Title of my master thesis

Franziska Hellmuth

Thesis submitted for the degree of
Master in Meteorology
60 credits

Department of Geoscience
Faculty of Mathematics and Natural Sciences

UNIVERSITY OF OSLO

Spring 2018

Title of my master thesis

Franziska Hellmuth

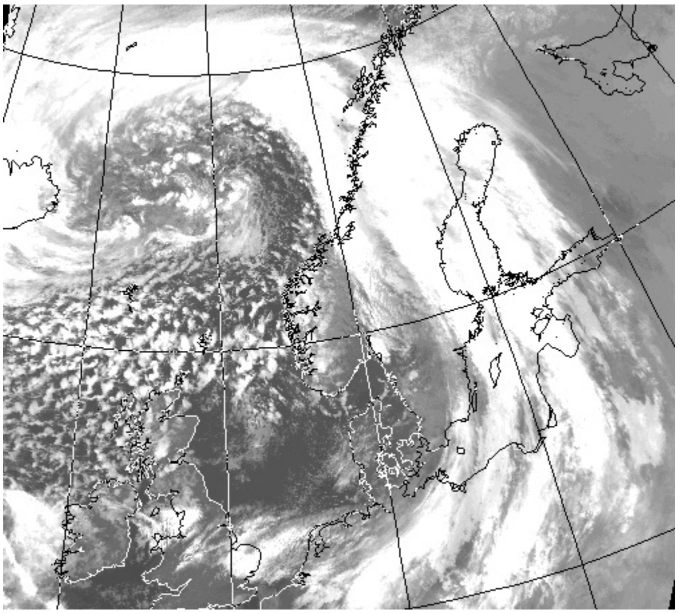

Satellite image of the extreme extratropical cyclone on 24 December 2016 at the coast of Norway. Image obtained from the Dundee Satellite Receiving Station http://www.sat.dundee.ac.uk.

Title of my master thesis

http://www.duo.uio.no/

Printed: Reprosentralen, University of Oslo

ABSTRACT

This abstract needs to be updated.

ACKNOWLEDGEMENT

First and foremost, I would like to thank my supervisor, Richard Moore, for helpful discussions, good guidance, feedback, and giving me the opportunity to work with an interesting thesis. I would also like to thank my co-supervisor, Steve Copper, for all the help with the optimal estimation retrieval, the possibility to travel to Kiruna to learn more about the instrumentation and the good scientific discussions. A big thank you goes to Bjørg Jenny Kokkvoll Engdahl for all the help to understand the ensemble prediction model and for helping me with random questions I had throughout the year. I would also like to thank Kirstin Krüger for her large effort in giving me constructive and detailed feedback on my scientific writing in the last minute.

I want to thank my fellow students at MetOs for a nice environment and good social and professional conversations. I also want to thank all the other friends I met during my studies in Germany and during my exchange at UNIS, which would not have been so exciting without you.

A very special thank you goes to my all my good old friends and my family in Germany, who were always there for me and have supported and encouraged my choices all times. Last but not least, thanks to my boyfriend for proofreading, scientific discussions and listening to my complaints during time of frustration.

Table of Contents

List of Figures

List of Tables

List of Abbreviations

ACC	Accretion
AGG	Aggregation
AR	Atmospheric River
AROME	Applications of Research to Operations at Mesoscale
AUT	Autoconversion
BER	Bergeron-Findeisen process
C3VP	Canadian CloudSat-CALIPSO Validation Project
CFR	Contact Freezing of Raindrops
CPR	Cloud Profiling Radar
CV	Coefficient of Variation
CVM	Conversion-melting
DEP	Deposition
DRY	Dry processes
DT	Dynamic Tropopause
ECMWF	European Centre for Medium-Range Weather Forecasts
EPS	Ensemble Prediction System

FMI	Finnish Meteorological Institute
HEN	Heterogeneous Nucleation
HON	Homogeneous Nucleation
IVT	Integrated Vapour Transport
LWC	Liquid Water Content
MASC	Multi-Angular Snowfall Camera
MEPS	MetCoOp Ensemble Prediction System
Meso-NH	Mesoscale Non-Hydrostatic model
Met-Norway	Norwegian Meteorological Institute
MetCoOp	Meteorological Co-operation on Operational NWP
MLT	Melting
MRR	Micro Rain Radar
MSLP	Mean Sea Level Pressure
NWP	Numerical Weather Prediction
PIP	Precipitation Imaging Package
PSD	Particle Size distribution
RIM	Riming
SMHI	Swedish Meteorological and Hydrological Institute
SWC	Snow Water Content
SWP	Snow Water Path
WCB	Warm Conveyor Belt

WET	Wet processes
WMO	World Meteorological Organization

Chapter 1: Introduction

An increased frequency of extreme weather events and heat waves, droughts, heavy rains or extremely high winds is one predicted consequence of global warming [Hansen et al., 2014]. Weather and climate extremes can have serious effects on human society and infrastructure, as well as on ecosystems and wildlife. Therefore, they are mostly in the media reports on the topic of climate in the focus [Meehl et al., 2000]. Understanding and predicting the impact of extreme weather events is one of the major challenges of current climate research [Field et al., 2014, Stocker et al., 2013].

It has long been known that measuring precipitation, especially in the form of snow, is difficult. Winter precipitation measurement errors between different observation networks and different regions show biases of more than 100 % [Kochendorfer et al., 2017]. Uncertainties in precipitation measurements under windy conditions can affect water balance calculation and the calibration of remote sensing algorithms [Wolff et al., 2015]. Measurement uncertainties can be caused by the instrument itself, which varies with wind speed, wind shielding, shape and size, as well as phase and fall velocity of hydrometeors [Kochendorfer et al., 2017, Wolff et al., 2015].
Precipitation observations are important for hydrological, climate and weather research, as more than one-sixth of the world's population receives water from glaciers and seasonal snow packs [Barnett et al., 2005].
Since winds have an influence on solid precipitation, a WMO (World Meteorological Organization) precipitation analysis between 1987 and 1993 recommended that the double-fence inter-comparison reference should be used as a reference for snow measurements [Goodison et al., 1998]. In 2010, it followed an adjustment for unshielded and single-shielded precipitation gauges. The adjustment transfer function represents a capture efficiency as a function of air temperature and wind speed to delimit the error for snowfall [Kochendorfer

et al., 2017, Wolff et al., 2015].

Estimates from radar reflections derived snowfall rates are not unique. Nearly identical snowfall rates for given radar reflectivity signatures can be generated from various combinations of snowflake microphysical properties and particle fall velocity. This can lead for individual events to an error in retrieval uncertainties of 100–200 % [Wood, 2011]. Kulie and Bennartz [2009] used CloudSat Cloud Profiling Radar (CPR) reflectivity to estimate the global dry snowfall rate for one year. They found that snowfall estimates critically depend on assumed snowfall particle size distribution, shape and radar reflection. These studies suggest that snowfall estimates resulting only from radar reflections are ambiguous. Numerous different combinations of snowflake microphysical properties and snow particle falling rates can yield to nearly identical surface snowfall rates for a given reflectivity profile. Therefore, the use of traditional Ze-Se relationships can lead to a large difference when comparing different snowfall events [Cooper et al., 2017].
Based on observations of particle size distribution, fall velocity, snowflake habit, and a modified version of the optimal estimation CloudSat snowfall algorithm followed an average difference reduction to 18 % of snowfall estimates, when compared to a National Weather Service measurement in Barrow, Alaska [Cooper et al., 2017].

With the increasing expansion of computational power, developments of high-resolution numerical weather forecasting models with ≤4 km scales can enable small-scale phenomena such as convective dynamics to be represented [Gowan et al., 2018]. This enhancement provides weather services the ability to improve short-term weather forecasts for convective events, which can seriously impact infrastructure and society [Müller et al., 2017]. The ability to use high-resolution models is also followed by various challenges, such as physical parametrisation schemes, accurate representation of topography, and data assimilation of high-resolution data [Sun, 2005].
The weather forecast in Scandinavia covers a wide range of phenomena and includes continental, maritime and polar conditions. Norway has a complicate coastline, gradients in land use, as well as complex topography, which can complicate local weather forecasting of temperature, wind and precipitation [Müller et al., 2017]. Several studies such as Colle et al. [2005], Garvert et al. [2005], Schwartz [2014] have shown, that simulations of orographic precipitation can be improved in mountainous terrain for horizontal grid spacing below 4 km. Uncertainties on a convective scale can lead to a rapid error growth

[Lorenz, 1969], hence high-resolution ensemble prediction make it possible to estimate the forecast uncertainty by performing several model runs, each with different initial conditions.

This work focuses on the measurement site Haukeliseter in Southern Norway and the extreme storm during Christmas 2016. The extreme storm was named 'Urd' by the Norwegian meteorological Institute. Storms of this kind are expected to occur on average every five years. The financial costs associated with 'Urd' are estimated to about 180 million Norwegian kroner. 'Urd' led to major traffic problems for cars, trains, ferries and air planes. Most mountain crossings were kept closed during Christmas 2016 [Olsen and Granerød, 2017]. A change in temperature and therefore change of precipitation from solid to liquid followed an increase in avalanche danger. In addition, was there a power breakout of around 70.000 households and 40 emergency power stations failed during the extreme weather (Figure 1.0.1).
The Christmas storm in 2016, might not have led to the same damages as some of the extreme weather events of recent years. But as people and infrastructure are affected by extreme weather, it is necessary to further improve the accuracy of snow-ground observations to better verify numerical weather forecasts, hydrological and climate models [Joos and Wernli, 2012]. This may lead to improvements in short- and long-term predictions as well as predicting the variability of the global water balance [Seneviratne et al., 2012]. Changes in snow pack characteristics after severe rain on snow events can lead to severe avalanches [Stimberis and Rubin, 2011] and to the formation of thick layers of ice in the snow pack or on ground [Hansen et al., 2011, Putkonen and Roe, 2003].

Since winter 2010, the site has been a WMO measuring station with single and double fence precipitation instruments. In the winter of 2016/2017, three additional state of the art radar and snowflake microphysical instrumentation were deployed which could be uset to estimate the vertical profile of snow water content in the atmosphere. The snowflake characteristics are estimated using a multi-angle snowflake camera [MASC; Garrett et al., 2012] and a Particle Imaging Package [Newman et al., 2009, PiP;]. With the aid of the modified CloudSat snow particle model algorithm and the snowflake properties, as well as reflectivity profiles, the amount of snowfall in the atmosphere can then be determined. The usage of a snowfall retrieval with ground-based measurements will give an insight into the microphysical structure of the extreme event. The double fence measurements

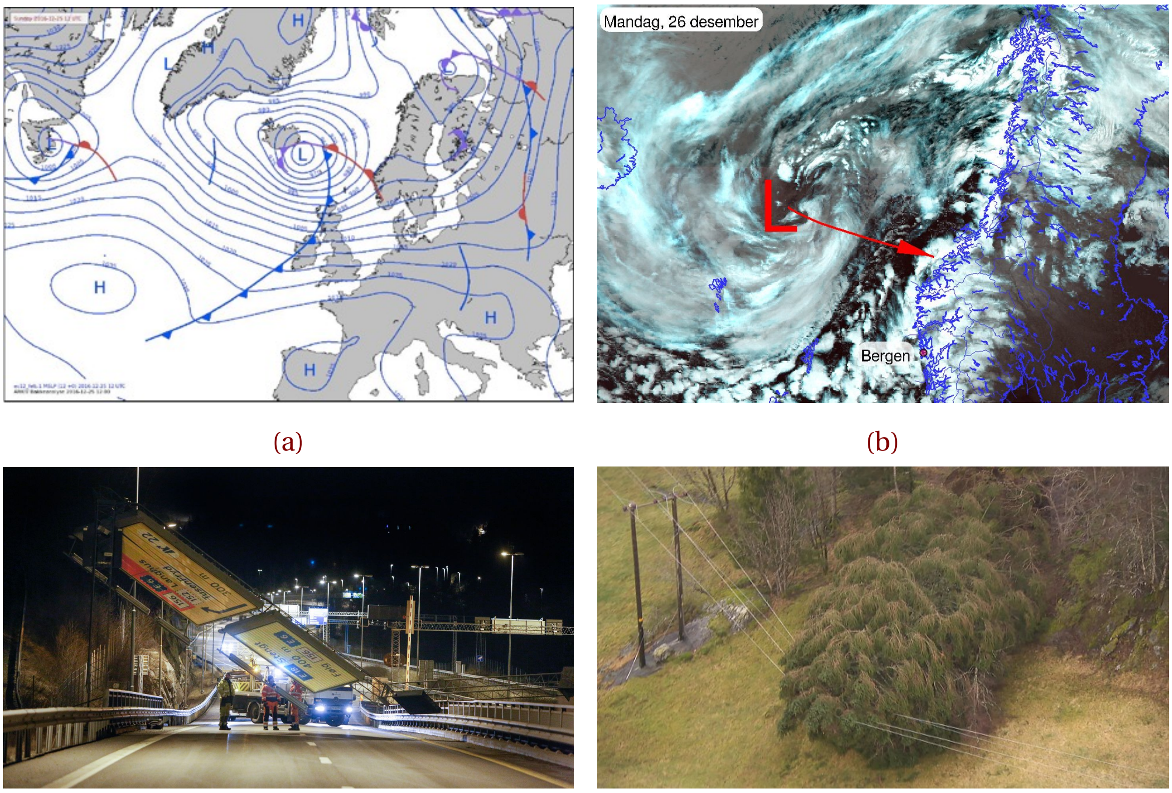

(a) (b)

(c) (d)

Figure 1.0.1: Weather situation during the extreme Christmas storm and impact on the infrastructure. In a: Weather situation Sunday 25 December 2016 at 12 UTC from the extreme weather report on Urd [Olsen and Granerød, 2017]. b: Tweet from Meteorologene [2016] on 26 December 2016 at 9:34 am: Here comes #Urd! The low pressure centre will hit Møre og Romsdal, but the strongest wind comes south of Stad. #SørNorge. c and d show the consequences related to the high wind speeds during Christmas 2016. c: This traffic sign, ten meter long and four meter high was blown down during the storm, [Ruud et al., 2016]. d: Trouble maker: The extreme weather during Christmas created problems for the local infrastructure. 80.000 households were without electricity during the storm, [Farestveit, 2016].

should help to estimate vertically derived snowfall on the ground.

Additionally, since November 2016 the Meteorological Cooperation on Operational Numerical Weather Prediction (MetCoOp) Ensemble Prediction forecast (MEPS) is operational at the Meteorological Institute of Norway (Met-Norway). The ensemble prediction system uses the previous deterministic AROME-MetCoOp, a version of the Mèteo-France Applications of Research to Operations at Mesoscale and initialises in addition ten perturbed ensemble members. The newly developed ensemble prediction systems (EPS) from Met-Norway is used to analyse the extreme winter storm during Christmas 2016. It will be shown if the ensemble prediction system is able to forecast the variation of an extreme winter storms such as 'Urd' and if it is able to predict large scale effects as well as local effects. Furthermore, the use of an ensemble prediction system will give the possibility to analyse the variation of snowfall precipitation in the vertical and at the surface. Using observations to evaluate MEPS will help to examine the following research questions. How well will the model predict the surface snowfall at the measurement site? Will precipitation transitions from snow to rain to snow forecasted by the regional model? Does the regional model cover local affects associated with the topography around the site?

The thesis is structured as following: Chapter 2 will give an overview of the measurement site Haukeliseter and its instrumentation. Followed by the methodology on the optimal estimation retrieval as well a description of the regional model MEPS. Afterwards the application to the data to compare the forecast system and the observations will be presented. The synoptic analysis of the extreme Christmas storm in 2016 is presented in Chapter 3. After this, will Chapter 4 present the results and the discussion on large scale effects, surface snowfall accumulation and local wind influence at Haukeliseter. The final chapter summarises the results and findings and suggests future research which has to be done.

Chapter 2: Site, Instrumentation, Data, and Methodology

This chapter describes the site, instruments, the optimal estimation retrieval and the regional forecast model used to determine the vertical profile of snow water content for observed snow events. The determination of required parameters from the measuring instruments in relation to the optimal estimation retrieval will be explained. The purpose of this study is to compare the vertical observations from the Haukeliseter measurement site and the output from the operational forecast model at the Norwegian Meteorological Institute for the extreme weather event during Christmas 2016. The last section will give an insight on how the data was analysed to compare the different systems.

2.1 Haukeliseter site

Haukeliseter, shown in Figure 2.1.1 is a mountain plateau 991 m above sea level, located in the Norwegian county 'Telemark' (59.8° N, 7.2° E, Figure 2.1.1). The station measures precipitation, temperature, snow depth and wind. It has served as a measurement site for snow accumulation since the winter of 2010/2011 [Wolff et al., 2010, 2013, 2015] and serves as WMO (World Meteorological Organization) station.
The study site is surrounded by mountain tops being 100 m to 500 m higher than the flat area. As seen in Figure 2.1.1c is Haukeliseter more open to the south and the south-west and the closest mountain top (situated to the NE) has an altitude of 1162 m a s l, [Wolff et al., 2015]. The mountains west to north exceed elevations of 1600 m.
A detailed setting of the measurement site is shown in Figure 2.3.1. The precipitation sensors are perpendicular to the predominant wind. Additional measurements of other

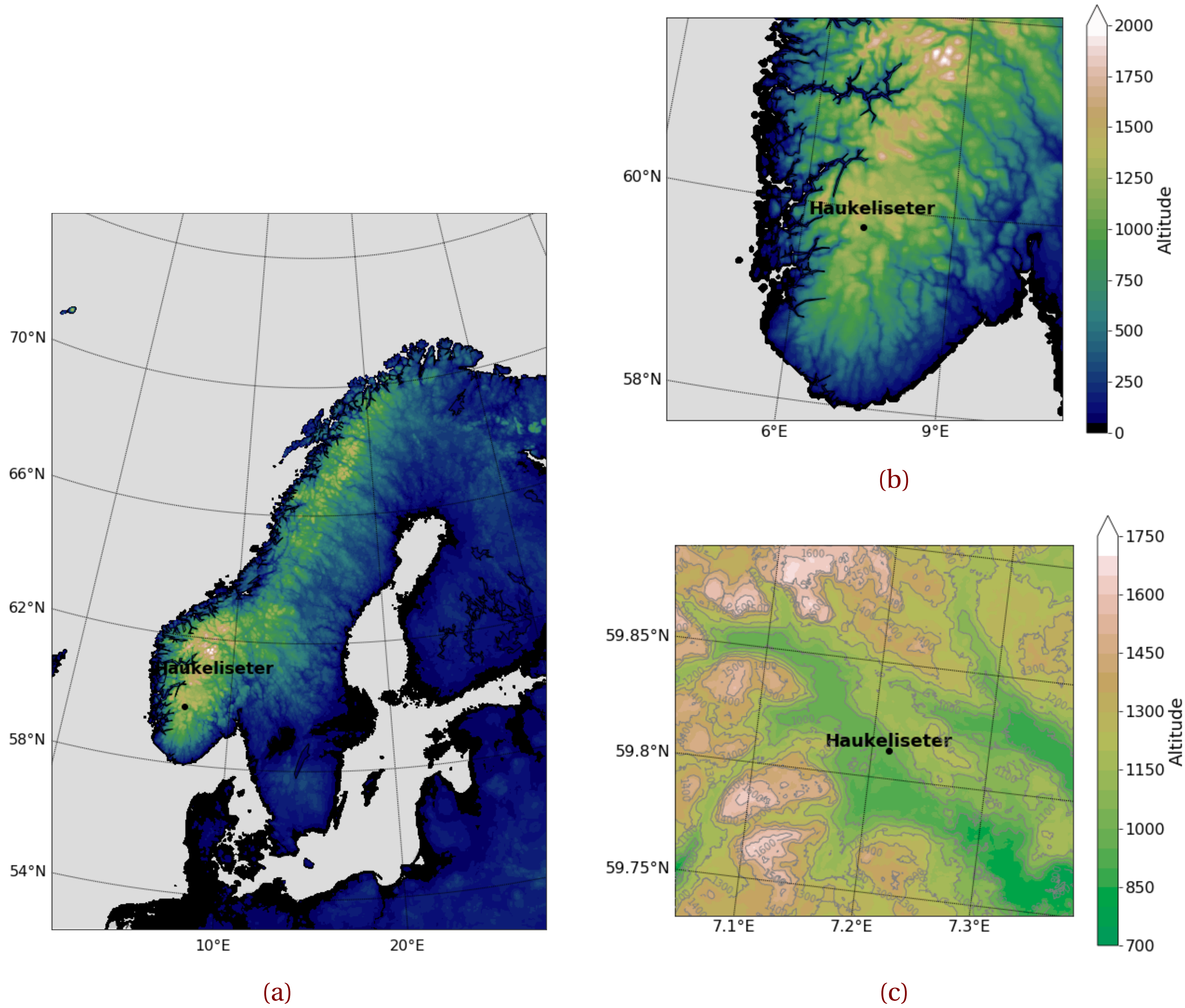

Figure 2.1.1: Model elevation map of Northern Europe (a) and Southern Norway (b), where the model domain of MEPS are presented in Lambert projection. The elevation corresponds to the legend of b. A topographic map of the measurement site is shown in c with DTM 10 Terrain Model (UTM33) from Geonorge [2018].

meteorological parameters such as temperature, wind, and pressure are used to connect the large-scale weather situation with the local measurements. The data is provided by eklima [2016], where the temperature is measured at double fence height. The hourly value of temperature is represented by the last minute value of the previous hour measurement. The 10 m wind is measured by an ultrasonic wind sensor from Gill, mounted at the tower close to the double fence. Wind data is obtained from eklima [2016] and represents 10 min averages from the last 10 min of an hour.

2.2 Climate at Haukeliseter

The general climate at Haukeliseter can be defined with the updated Köppen-Geiger climate types presented in Peel et al. [2007]. Figure 8 in Peel et al. [2007] show, that Haukeliseter may lay in a transition zone and can be categorized as ET, a polar tundra climate type (hottest month temperature $T_{hot} \geq 0\,°C$) or as Dfc, a cold climate without dry season and cold summers. Haukeliseter presents a typical Norwegian climate condition. At the measurement site, frequent snow events combined with high wind speeds are observed during a six to seven month winter period. In addition, a snow amount of about two to three meter can be expected, where 50 % of the yearly precipitation is solid in the form of snow, graupel or mixed-phase precipitation [Wolff et al., 2010, 2013, 2015].
The mean wind direction (Figure 2.3.1) for solid precipitation is from the west/east with maximum wind speed above $15\,m\,s^{-1}$, observed during a 10-year winter period at a nearby station [Wolff et al., 2010, 2015]. In Figure 2.2.1, the green dashed line represents the average December temperature of $-6\,°C$ (30-yr period 1961 to 1990,[eklima, 2016]). December 2016 was warmer with an anomaly of +4.9 K above the climate mean. In 2016, the precipitation was 200 % more than the climate mean during December. This difference could be associated with the new installation of the double fence - Geonor gauge at Haukeliseter. In Wolff et al. [2015], Figure 5 shows that single fence precipitation gauges underestimate the amount of precipitation about 80 % during high wind speed events. Since the Double Fence construction was not in use before 2010/2011, which might have led to an observation of too little precipitation at Haukeliseter during winter and a followed incorrect climate statistic. The precipitation observed in the period of 21 to 27 December 2016 where 56.9 % of the total accumulated precipitation in December 2016. Furthermore, a maximum wind of $22.3\,m\,s^{-1}$ was observed in this period, which can be associated with a slight storm (Section 3.5 and Table 3.5.1).

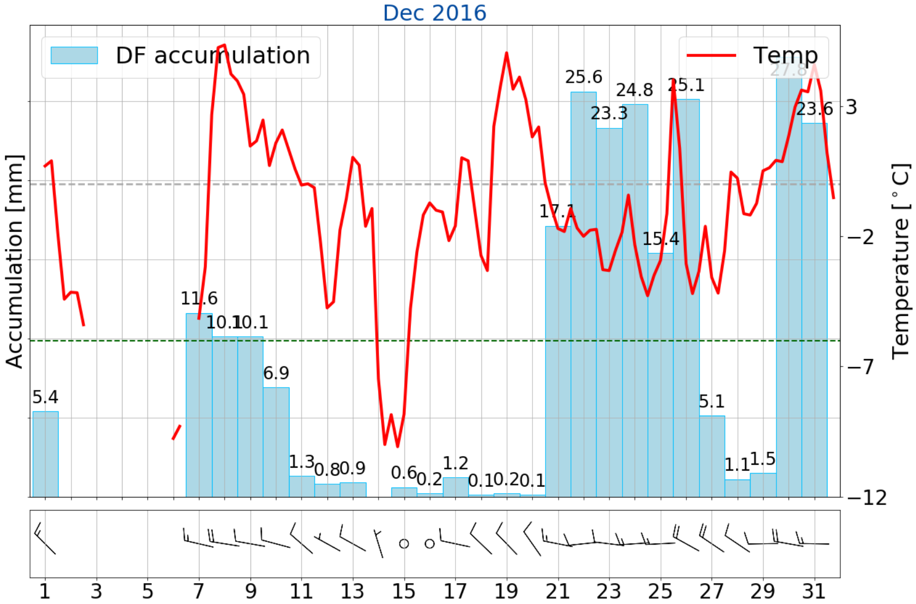

Figure 2.2.1: Observations at Haukeliseter weather mast during December 2016. The daily accumulation is presented in light blue [mm]; the six hour mean temperature in red, [°C], and daily maximum 10 m wind as barbs [m s^{-1}]. Gray dashed line indicates the freezing temperature. The freezing temperature is indicated by the green dashed line and the monthly normal value (−6.0 °C) by the green eklima [2016]. Note, no data was available from 2 to 6 December 2016.

2.3 Instruments

The WMO site Haukeliseter, operated by Met-Norway serve numerous meteorological measurements of temperature, wind speed and direction. 10 m wind and 4.5 m air temperature are measured at the tower close to the double fence (Section 2.3.1). The wind measurements are performed with an ultrasonic wind sensor from Gill (Wind observer II with extended heating). Air temperature is obtained with a pt100 element at gauge height and protected by standard Norwegian radiation screen [Wolff et al., 2015]. Pressure?

Further information about the WMO site and the instrument setting, can be found in Wolff et al. [2013, 2015].

A collaboration between the University of Utah, University of Wisconsin and Met-Norway made it possible to install three additional instruments at the measurement site during winter 2016/2017. A Multi-Angle Snowflake Camera (MASC) and a Precipitation Imaging Package (PiP) will be used to determine the snow habit, the snowfall particle size distribu-

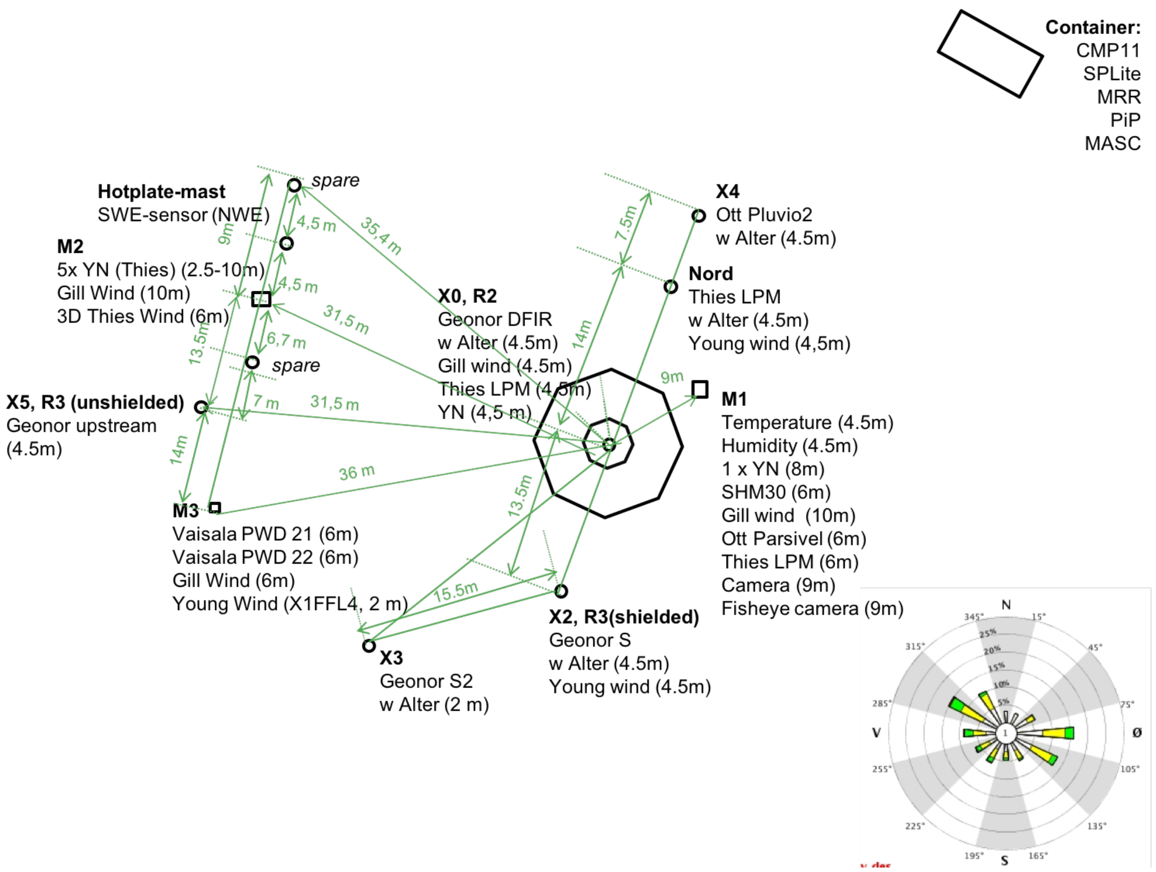

Figure 2.3.1: Instruments at the Haukeliseter measurement site during winter 2016/2017 [adapdet from Wolff et al., 2015]. The windrose indicates the mean wind direction from either from west-north-west or east-south-east.

tion, and the near-surface fall speed. Additionally, a Micro Rain Radar (MRR) is established to obtain fall speed and particle reflectivity aloft. Since many factors such as humidity and temperature contribute to snowflake geometry is the knowledge of snowflake habits, particle size distributions, and fall speed crucial to reduce error in snowfall retrievals.
This work is based on several datasets collected at the Haukeliseter measurement site, 59.8° N, 7.2° E. A composition of advanced ground-based observations and a modified 24 GHz-MRR scheme presented by Cooper et al. [2017] will help to get a better understanding of the vertical structure of the atmosphere and to reduce the uncertainties in the estimation of surface snowfall rate found using the optimal estimation retrieval scheme (Section 2.4).

A sketch of the instrumentation setting is presented in Figure 2.3.1. The octagonal indicates the double fence. The container is north-east from the double fence having the MRR, MASC and PiP mounted at the top. **M1** in Figure 2.3.1 is the 10 m weather mast, providing the hourly eklima [2016] temperature, pressure, and wind measurements. The mean wind direction from west-north west and east-south east are shown in the wind rose in Figure 2.3.1.

2.3.1 Double Fence Snow gauge

Since the winter 2010/2011 Haukeliseter is equipped with several precipitation gauges. The wind shielded gauges are placed perpendicular to the main wind direction (E/W wind).

The wind-induced under-catch of solid precipitation is determined by Wolff et al. [2015]. The wind plays different roles in the amount of accumulation depending on the kind of precipitation. For temperatures below −2 °C the wind speed influences the falling snow. Where less precipitation can be observed at higher wind speeds or more precipitation can be measured if too much is blown into the gauge. The catch ratio between the standard Geonor precipitation gauge and the Double Fence - Geonor (Figure 2.3.2a) shows that only 80 % of solid precipitation is observed at wind speeds of 2 $\mathrm{m\,s^{-1}}$ whereas only 40 % at 5 $\mathrm{m\,s^{-1}}$, Figure 5 in Wolff et al. [2015].

The precipitation gauge protected by an octagonal double fence (Figure 2.3.2a) is more accurate than the single fence and will be used as the reference to all surface accumulation measurements. The double fence creates an artificial calm wind and maximize the catch of precipit-

(a)

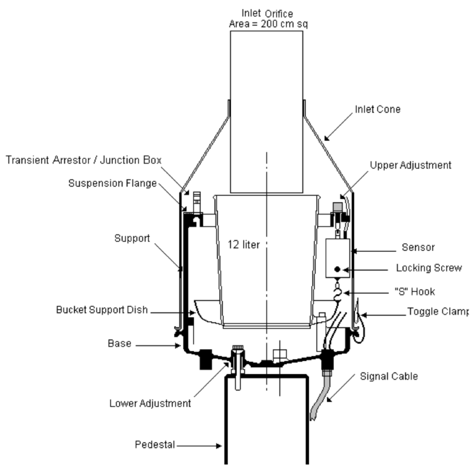

(b)

Figure 2.3.2: a: Double fence and unprotected precipitation gauges at Haukeliseter, from Wolff et al. [2015]. The prevailing wind direction from east comes from the lower, left corner in the image and the west wind from the opposite site. b: Vertical cross section of T-200B precipitation gauge [Geonor Inc., 2015].

ation, [Wolff et al., 2010, 2013, 2015]. The wind inside the double fence is measured to be not much higher than $5\,\mathrm{m\,s^{-1}}$ even if the winds outside exceed $20\,\mathrm{m\,s^{-1}}$ (occurred 26 December 2016).
This shows the need of a combination of ground-based observations together with an optimal estimation retrieval to verify the accuracy of MEPS. Wolff et al. [2015] introduced an adjustment function for the Geonor double fence, so that different precipitation under certain wind speeds are presented correctly and can be used as confidential data. For now, it is presumed that the average under catch inside a double fence is 20 % for wind speeds between $10\,\mathrm{m\,s^{-1}}$ and $20\,\mathrm{m\,s^{-1}}$ and 10 % for wind speeds below $9\,\mathrm{m\,s^{-1}}$ [Wolff, 2018].

Inside the double fence is a precipitation-weighing gauge Geonor T-200B3 [3-wire transducers, 1000 mm, Geonor Inc., 2015] with an Alter wind screen to reduce wind turbulence around the gauge. At Haukeliseter the orifice height of the Geonor is 4.5 m above the ground because of an expected snow depth of two to three meter during a winter season and the likelihood of measuring drifting snow [Wolff et al., 2013, 2015].
A vertical cross section of the T-200B gauge is shown in Figure 2.3.2b. The precipitation particles fall through the $200\,\mathrm{cm}^2$ orifice protected with a heated collar, into a cylindric bucket filled with frost protection. The bucket is placed on top of a Bucket Support Dish [Figure 2.3.2b, Geonor Inc., 2015]. This dish is connected with three wire sensors having an eigenfrequency changing with the weight inside the bucket. A formula provided by Geonor Inc. [2015] calculates the amount of precipitation with the frequency of each sensor. The three sensors provide a reduction of an error in connection with an unlevel installation. Met-Norway average the values of all three sensors and provide hourly data at eklima.

2.3.2 MRR - Micro Rain Radar

Radars are very useful to observe the vertical profile of the atmosphere. The instrument detects mesoscale features and makes it possible to visualise the vertical structure of storms [Markowski and Richardson, 2011].
The principle of radar measurements is based

Figure 2.3.3: Micro Rain Radar at the measurement site in Kiruna.

on an electromagnetic wave, which is emitted from the radar transmitter and interacts with the hydrometeors along the beam. A fraction of the pulse energy is reflected back to the receiver of the radar. The quantity of scattering depends on the shape and structure of the reflected particle. Vertical profiles of reflectivity give information about the diameter of the target object.

The Micro Rain Radar (Figure 2.3.3) measures profiles of Doppler spectra [METEK, 2010]. The Doppler spectrum describes the movement of the particle. The vertical pointing Doppler radar measures the returning energy from each interval and enables the detection of the Doppler spectrum [L'Ecuyer, 2017]. The MRR has a frequency of 24 GHz and a temporal and spatial resolution of 60 s and 100 m, respectively. The radar height range from 100 m (because of ground clutter) to 3.000 m [METEK, 2010].

MRR radar reflectivity (Z) is transformed from 1 mm^6/m^3 to dBZ, by the following relationship;

$$Ze = 10\log_{10}\left(\frac{Z}{1\,\mathrm{mm}^6/\mathrm{m}^3}\right) \qquad [\mathrm{dBZ}] \tag{2.3.1}$$

A transformation to rainfall rates can be performed by the Z-R (reflectivity - rainfall) relationship. The rainfall rate in each layer can be estimated by the use of typical fall speeds and the Marshall-Palmer particle size distribution for liquid particles [Rinehart, 2010], Equation (2.3.2)

$$\begin{aligned} Z &= 200R^{\frac{8}{5}} \qquad [\mathrm{mm}^6\mathrm{m}^{-3}] \\ R &= \left(\frac{10^{\frac{Ze}{10}}}{200}\right)^{\frac{8}{5}} \qquad [\mathrm{mm\,h}^{-1}] \end{aligned} \tag{2.3.2}$$

The Z-R relationship with the Marshall-Palmer assumption (Equation (2.3.2)) applied is represented in Table 2.3.1. Z-snowfall relationships are developed but are difficult to apply due to the variation of size and density of the particles [L'Ecuyer, 2017].

After the transformation to dBZ the reflectivity is averaged for every 200 m thick layers, where only values above 300 m taken into account, e.g. a reflectivity at 400 m represents the mean value of reflectivity between 300 m and 500 m.

Table 2.3.1: Typical reflectivity values, according to Doviak and Zrnic [1993], obtained from measurements, models, and observations. The rainfall rate R is calculated with Equation (2.3.2).

	Ze [dBZ]	**R** [$\mathrm{mm\,h^{-1}}$]
Drizzle	<25	1.3
Rain	25 to 60	1.3 to 205.0
Snow		
dry, low density	<35	5.6
Crystal; dry, high density	<25	1.3
wet, melting	<45	23.7
Graupel		
dry	40 to 50	11.5 to 48.6
wet	40 to 55	11.5 to 99.9
Hail		
small; <2 cm, wet	50 to 60	48.6 to 205.0
large; >2 cm, wet	55 to 70	99.9 to 864.7
Rain & Hail	50 to 70	48.6 to 864.7

2.3.3 PIP - PRECIPITATION IMAGING PACKAGE

The precipitation imaging package (PiP) is a modification of the Snowflake Video Imager presented by Newman et al. [2009]. The video distrometer is a construct of a halogen flood lamp and a video system (Figure 2.3.4). The instrument determines the habit of snowflakes from images at a frequency of 60 Hz. Both lamp and lens have a distance of approximately 3 m that follows a field of view: 32 mm by 24 mm.

Figure 2.3.4: Precipitation Imaging Package.

In front of the halogen lamp there is a frosted window, so that the background light is uniform over all time. A falling particle appears as a 2-D shadow in the video image. Particle size distribution (PSD) and fall speed of precipitation can be determined from the black and white images provided by the system. Newman et al. [2009] describes the details of the algorithm applied to the system to get information about the snowparticle habit.

The Winds have almost no effect on the result of the video distrometer [Newman et al., 2009]. To reduce eventual wind effects, the distrometer was oriented perpendicular to the mean wind.

2.3.4 MASC - Multi-Angular Snowfall Camera

Instruments like the afore mentioned PiP has according to Garrett et al. [2012] coarser resolution and the determination of particle size can have larger errors. Hence, a new instrument was developed. The Multi-Angular Snowfall Camera (MASC) takes high-resolution images of hydrometeors in free fall and measures the fall-speed simultaneously.

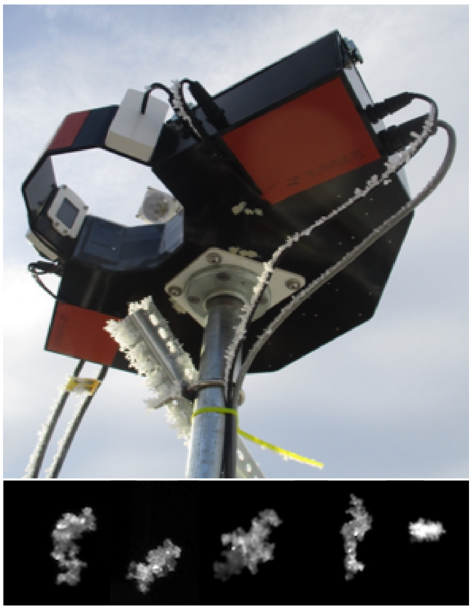

Figure 2.3.5: MASC and images taken by instrument during the Christmas storm 2016.

The MASC consists of three cameras, three flashes, and two near-infrared sensors, pointing at a ring centre (Figure 2.3.5). A hydrometeor has to pass through the ring in a certain way to trigger the near-infrared sensors. At the same time the three cameras take a picture of the falling particle. Since the cameras take pictures from three different angles, the particles size, shape, and orientation can be specified from an algorithm applied to the image, described in Garrett et al. [2012]. Furthermore, the form and heritage of the hydrometeor, such as collision-coalescence, riming, capture nucleation, or aggregation, can be estimated.
The near-infrared sensor, that is used to trigger the cameras and the lights quantifies the fall-speed of the hydrometeors, by measuring the time the particle needs to pass the distance between the upper and lower trigger.

2.4 Optimal Estimation Retrieval Algorithm

Since 2006, with the launch of the CloudSat Cloud Profiling Radar (CPR) a global estimation of snowfall can be done. Several studies, such as Kulie and Bennartz [2009] have shown that estimated snowfall values depend heavily upon assumed snowflake microphysical properties. Wood et al. [2015] showed that a refinement of the CloudSat snowfall retrieval algorithm can be performed by using snowflake models. This study was based on data from the Canadian CloudSat-CALIPSO Validation Project [C3VP, Hudak et al., 2006],

where they concentrated on cold season clouds and precipitation.
In an attempt to reduce the non-uniqueness of the problem, Wood et al. [2015] used the a priori knowledge of snowfall microphysics and temperature (from ground-based observations) to refine the forward-model assumptions for the CloudSat snowfall retrieval scheme. Results from this scheme showed a good agreement with reported values observed at meteorological measurement sites.
Model estimates have proven, how useful the estimation retrieval can be to verify ground-based radar snowfall measurements [Norin et al., 2015]. Although the retrieval has obviously been improved the estimation algorithm, a priori guess can still lead to uncertainties in the retrievals of up to 140 % to 200 % [Wood, 2011].
Cooper et al. [2017] developed a technique to combine MRR, MASC, and PiP information into a common retrieval framework. Specifically, estimates of snowflake microphysical properties from the MRR are used as the a priori term in the optimal-estimation retrieval scheme. The usage of either MASC/PiP or MRR fall-speed can show which a priori guess in the retrieval gives the more accurate retrieved snowfall rate at the ground.
The difference between the retrieval and the snow gauge observations was −18 % when applied to data from Barrow, Alaska.
Cooper et al. [2017] also showed that the retrieval is sensitive to habit and fall speed. The installation of a MRR, MASC, and PIP should help to adjust the particle models for graupels and rimed particles which are often observed at Haukeliseter.

2.4.1 Forward model

Forward model defines a relationship between the radar observations and the retrieved state vector **x**. It is difficult to find the properties of the atmosphere by using observations due to unknown parameters influencing the measurement.

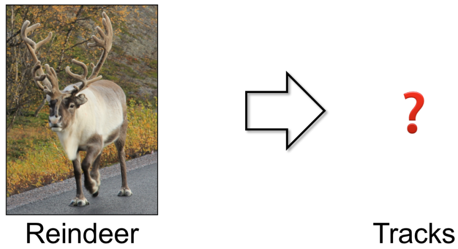

(a)Forward problem.

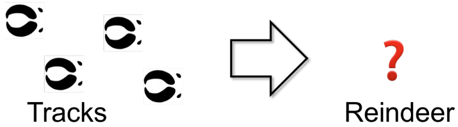

(b)Inverse problem.

Figure 2.4.1: a: Relationship between parameter of interest (reindeer) and the unknown parameter of measurements (tracks). b: Inverse problem when the parameter of measurements is known but the parameter of interest is not [Stephens, 1994].

Stephens [1994] described the forward problem in the manner that e.g. a reindeer represents the known source, observations Figure 2.4.1. The amount of received radiation lost during the transmittance to the sensor is unknown, the Tracks in Figure 2.4.1a. The forward model will help to find simulated observations before the attenuation took place and give information about the tracks of the reindeer. In the scope of this work the inverse problem is solved. The tracks in Figure 2.4.1b present the vertical reflectivity observations from the MRR. Using the forward model will solve the inverse problem by finding the question mark in Figure 2.4.1b, which are simulated profiles of SWC.

The knowledge about the a priori parameters and related covariances, as well as **x**, are used to minimize the cost function in Equation (2.4.3). The values of **x** are found by Newtonian iteration Wood et al. [2014, Eq. 5].

The snow water content in each layer is estimated from the knowledge of the snow particle mass-dimension relationship in Appendix B.1, and a PSD related to slope parameter and number concentration (Equations (2.4.8–10)).

$$\mathrm{SWC} = \int_{r_{min}}^{r_{max}} m(r)n(r)dr \qquad [\mathrm{g\,m^{-3}}] \tag{2.4.1}$$

To achieve a relationship between the reflectivity and the snowfall amount one needs to account for attenuation in the atmosphere. Using the previously calculated PSD (Equation (2.4.8)) the backscattering cross-section σ_{bk}, one can estimate the reflectivity for

Rayleigh approximated, singly-scattered non-attenuated ice particles [Kulie and Bennartz, 2009, L'Ecuyer and Stephens, 2002, Wood et al., 2015]. The Rayleigh approximation assumes, that $2\pi r/\lambda \ll 1$, where λ the wavelength of incident radiation.

$$\eta_{bk} = \int_{r_{min}}^{r_{max}} n(r)\sigma_{bk} dr \qquad [\mathrm{m}^{-1}]$$
$$Ze^{ss,na} = \frac{\Lambda^4}{\|K_w\|^2 \pi^5}\eta_{bk} \qquad [\mathrm{mm}^6\mathrm{m}^{-3}] \tag{2.4.2}$$

where, Λ is the wavelength of the radar; $\|K_w\|^2$ is the complex refractive index of water and varies between 0.91 and 0.93 for wavelength between 0.01 m and 0.10 m and is independent of temperature. It also exists a complex refractive index for ice $\|K_i\|^2$, which is 0.18. This is valid for a density of 0.917 $\mathrm{g\,cm^{-3}}$ and is independent of temperature and of wavelength in the microwave region [Doviak and Zrnic, 1993]. In this work $\|K_w\|^2 = 0.93$ is chosen. Why did we choose K_w and not the one for ice?

2.4.2 Snowfall retrieval scheme

The optimal estimation method is based on Gaussian statistics. Minimizing the scalar cost function, Φ for the snowfall properties, $\mathbf{x}$. The cost function weights the difference between the observed reflectivity and the simulated measurements as well as the difference between the estimated and a priori guess.
Scalar cost function:

$$\begin{aligned}\Phi(\mathbf{x}, y, a) =& (y - F(\mathbf{x}))^T \mathbf{S}_y^{-1} (y - F(\mathbf{x})) \\ &+ (\mathbf{x} - a)^T \mathbf{S}_a^{-1} (\mathbf{x} - a)\end{aligned} \tag{2.4.3}$$

where, $\mathbf{x}$, vector of retrieved snowfall properties (Equation (2.4.11)); y, vector of observation (MRR reflectivity) ; a, vector of the a priori guess (temperature dependent); $\mathbf{S}_a$, a priori error covariance matrix; $\mathbf{S}_y$, measurement error covariance matrix. The forward model $F(\mathbf{x})$, presented in Section 2.4.1 relates unknown snowfall parameters $\mathbf{x}$ to radar observations y and approximates the true physical state between them [Cooper et al., 2017, Wood et al., 2014].
$\mathbf{S}_a$ links the uncertainties of the PSD information and the surface temperature differences. The diagonal matrix elements in $\mathbf{S}_a$ are equal to 0.133 and 0.95 for the particle slope parameter and the number concentration, respectively as from Eq. 7.35 and 7.36 in Wood

[2011].

$\mathbf{S}_y$ characterises the uncertainties associated with the measurements and the error in the forward model. This study uses for the diagonal matrix elements 2.5^2 UNIT!? based on the study from CITATION. BECAUSE.

I don't understand the next steps and if it is still the same **x**?!

At convergence is the error covariance of the retrieved state vector $\mathbf{S}_x$

$$\mathbf{S}_x = \left(\mathbf{S}_a^{-1} + \mathbf{K}^T \mathbf{S}_y^{-1} \mathbf{K}\right)^{-1} \tag{2.4.4}$$

which follows for **x**

$$\mathbf{x} = \underbrace{\left(\mathbf{S}_a^{-1} + \mathbf{K}^T \mathbf{S}_y^{-1} \mathbf{K}\right)^{-1}}_{\mathbf{S}_x} \left(\mathbf{S}_a^{-1} a + \mathbf{K}^T \mathbf{S}_y^{-1} \left(y - F(\mathbf{x}) + \mathbf{K}\mathbf{x}\right)\right) \tag{2.4.5}$$

The Jacobian matrix, **K**, represents the sensitivity matrix of the perturbed result of the forward model. The true state **x** is perturbed by ±0.2 % and thus **K** represents the relation between simulated values to the true state and how sensitive the simulated values are to small changes when starting a new retrieval cycle. The closer **K** is diagonal, the more is **x** determined by the real observed and a priori values. If the limit of the partial derivative is close to unity, the retrieved value **x** is its true state [Wood, 2011].

mmmh? What exactly are we doing here? Test the if convergent:

$$\hat{x} = \left(\mathbf{x} - F(\mathbf{x})\right)^T \mathbf{S}_x^{-1} \left(\mathbf{x} - F(\mathbf{x})\right) \tag{2.4.6}$$

only if $\hat{x}$ is smaller than 2 it is a 'good' retrieval.

To test the result of **x** a χ^2 test is performed at the convergence of $\mathbf{S}_x$.

$$\begin{aligned} \chi^2 &= \left(F(\mathbf{x}) - y\right) \mathbf{S}_y^{-1} \left(F(\mathbf{x}) - y\right)^T \\ &\quad + (\mathbf{x} - a)^T \mathbf{S}_a^{-1} (\mathbf{x} - a)\,. \end{aligned} \tag{2.4.7}$$

The first term in Equation (2.4.7) measures the part of χ^2 related to the noise of the forward model, and the second part the relation to the state vector. Thus, the second term describes the accuracy of the quantities within the reflectivity and temperature measurements [Rodgers, 2000]. Furthermore, are the error contribution from the reflectivity measurement uncertainty, $\mathbf{S}_{y_\epsilon}$, and the uncertainty of the a priori values, $\mathbf{S}_{a_\epsilon}$ estimated.

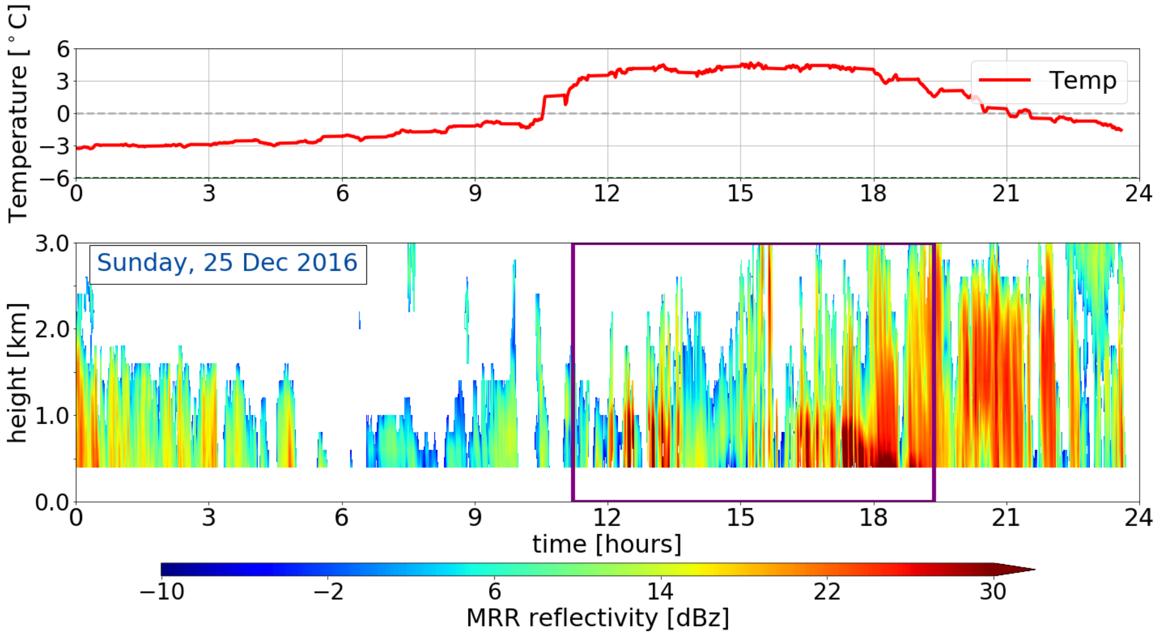

Figure 2.4.2: Shows the a priori temperature dependence within the optimal estimation retrieval for an all day precipitation event on 25 December 2016. The upper panel shows T_{ap} measured at the Haukeliseter site. The lower panel presents the reflectivity from the MRR in addition indicates the purple frame the time, where the MRR reflectivity was larger than −10 dBZ and surface temperatures less than 2 °C

2.4.3 Presence of snow

To achieve vertical profiles of snowfall from MRR different steps and assumptions are done in the here presented snowfall retrieval. From one of the lower levels, the snowfall rate at the surface can be estimated. The retrieval is only performed for profiles, which are likely to have observed snow, where most retrievals use rain. In previous studies relationships between reflectivity and snowfall have been developed. Even if the PSD of ice particles is known, different crystal shapes led to different results. Snow densities vary significantly from storm to storm, where small particles are still Rayleigh scattered, and larger particles non-Rayleigh scattered [Gunn and East, 1954].

To obtain the likelihood of present snow a reflectivity threshold of −15 dBZ is used. This threshold is similar to the one used in Wood et al. [2013], where it states that light liquid precipitation is related to −10 dBZ [Stephens and Wood, 2007]. Wood [2011] compared

the reflectivity in the lowest bin and adjacent bin and found, that the reflectivity above −15 dBZ are not influenced by ground clutter.
The Haukeliseter measurement site is equipped with a weather mast, measuring the air temperature every minute at two meter height (compare Figure 2.4.2, upper panel). Since the MRR measures above 300 m and only temperature measurements at the surface exists, a priori temperature (T_a) is assumed to be similar to the observed near-surface air temperature. Using a moist adiabatic lapse rate of $dT/dz = 5\,\mathrm{K\,km^{-1}}$ gives T_a in each layer. Assuming snow exists at temperature measurements up to a threshold of 2 °C, validated by Liu G. [2008] who analysed present weather reports to find the distinction between liquid and solid precipitation.
The purple line in the lower panel of Figure 2.4.2 represents the time frame during 25 December 2016, where the MRR reflectivity is less than −15 dBZ, and a priori temperature passes the 2 °C limit at the surface.

2.4.4 SIZE DISTRIBUTION

To determine the snowfall rate at the surface an exponential particle size distribution (PSD) is needed.

$$n(r) = N_0 \exp\left(-\lambda r\right) \qquad [\mathrm{m^{-3}\,mm^{-1}}] \tag{2.4.8}$$

where λ represents the PSD slope parameter and N_0 the number concentration. r is the particle maximum dimension evaluated from the 2D-scattering model for branched 6-arm spatial particles with porosities for reflectivity measurements at 24 GHz (see Appendix B.1). Since T_a varies with a moist adiabatic lapse rate in each layer bin the slope parameter and the number concentration in Equation (2.4.8) are changing too. Wood [2011] showed a linear fit between $\log(\lambda)$ and the a priori temperature, respectively $\log(N_0)$ and the a priori temperature. Using T_a in °C for each layer bin the following logarithmic assumption is used, to define the slope parameter and the number concentration.

$$\log(\lambda) = -0.03053 \cdot T_{ap} - 0.08258 \qquad [\log(\mathrm{mm^{-1}})] \tag{2.4.9}$$

$$\log(N_0) = -0.07193 \cdot T_{ap} + 2.665 \qquad [\log(\mathrm{m^{-3}\,mm^{-1}})] \tag{2.4.10}$$

To achieve the state vector **x** of unknown microphysical properties, the log-transformed values are taken.

$$\mathbf{x} = \begin{bmatrix} log(\lambda)_0 \\ \vdots \\ log(\lambda)_{\text{nlayer}} \\ log(N_0)_0 \\ \vdots \\ log(N_0)_{\text{nlayer}} \end{bmatrix} \qquad \text{nlayer} = 14 \tag{2.4.11}$$

The log-transformed equation is useful, since the results from C3VP were similar to other observations. The study showed, that N_0 ranges over several order of magnitude as well as λ was non-Gaussian for the snow events Wood [2011].

2.4.5 Snowfall rate at the surface

To achieve snowfall rates at the surface, the snow water content (Equation (2.4.1)) has to be transformed. The use of an assumed particle fall speed of $V = 0.85\,\mathrm{m\,s^{-1}}$ and the retrieved SWC (Equation (2.4.1)) gives the snow mass flux $J_{snow} = \mathrm{SWC} \cdot V$ in $[\mathrm{kg\,m^{-2}\,s^{-1}}]$. Why did we use this fall speed? Where does this assumption come from? Similar as Cooper et al. [2017] Eq. 4? To compare retrieved snow, fall rates to double fence measurements and the forecast model output, the precipitation amount at the surface is calculated.

$$P = J_{snow} \times 10^{-3} \cdot (3600\,\mathrm{s} \cdot 24) \qquad [\mathrm{mm\,d^{-1}}] \tag{2.4.12}$$

The precipitation amount at the surface, presented in Chapter 4, are taken to be equal to the values at the snow layer in 400 m, the lowest level of the obtained averaged MRR reflectivity.

2.5 MetCoOp Ensemble Prediction System

MEPS (MetCoOp Ensemble Prediction System) was newly operational at Met-Norway when the extreme weather occurred in Norway. Comparing model data with actual observations helps to verify the agreement between model prediction and ground-based

measurements.
AROME-MetCoOp was operational from March 2014 until November 2016, when it was replaced with an ensemble prediction system (EPS) based on AROME-MetCoOp. MEPS is used as weather forecast at the Norwegian Meteorological Institute, the Swedish Meteorological and Hydrological Institute (SMHI) and the Finnish Meteorological Institute (FMI), [Køltzow, 2017, Müller et al., 2017].

2.5.1 AROME - METCOOP

In principle, MEPS is a short-term weather forecast consisting of a ten ensemble member forecast system with 66 h prediction time and a horizontal resolution of 2.5 km and 65 vertical levels. One of the members is the deterministic forecast where the other nine present the perturbed state of the deterministic forecast. The initialisation of each member is performed at 0 UTC, 6 UTC, 12 UTC and 18 UTC [MetCoOp Wiki, 2017].
Forecast data saved for the deterministic and first ensemble member have a time resolution of one hour for 66 h. The other eight members have values every three hours for up to 48 h forecast time.
Figure 2.1.1a shows the MEPS model domain and its elevation as it was operational for December 2016. It covers the Nordic Countries including open water such as the Atlantic Ocean, the North and the Baltic Sea. A representation of the horizontal resolution zoomed on the Haukeliseter site is shown in Figure 2.5.1. Haukeliseter is surrounded by a complex terrain with mountains up to 1500 m no the west and the north and the more open terrain to the south-east.

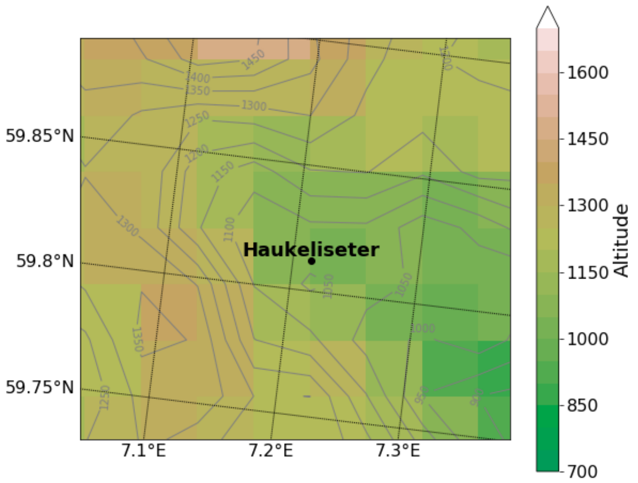

Figure 2.5.1: Representation of the topography around measurement site Haukeliseter in MEPS. Contours and shading present the elevation of the grid cells.

The centre of the model is approximately at 63.5° N, 15° E. The horizontal grid points are projected on a Lambert projection to receive the same area size of each grid cell. The outer, parent grid is the ECMWF-IFS model (European Centre for Medium-Range Weather

Forecasts Integrated Forecasting System) with a horizontal resolution of 9 km [Homleid and Tveter, 2016]. The ECMWF-IFS forecasts are used 6 h prior to the actual cycle in MEPS. Vertical hybrid coordinates are terrain-following and are mass-based, [Müller et al., 2017]. How the vertical hybrid coordinates are transformed into layer thickness or height is described in Section 2.6.1. Furthermore, MEPS underlies non-hydrostatic dynamics, Met-CoOp Wiki [2017].
The representation of snow is covered by a modification of the three-class ice parametrization (ICE3) scheme. Where liquid-phase processes are separated from slow ice-phase processes and described in Section 2.5.2. To model the snow cover an one-layer atmosphere model scheme is implemented. This includes three variables such as: snow water equivalent (SWE), snow density, and snow albedo [Müller et al., 2017].
As synoptic observations are included in the model the snow-depth predictions underlay a special performance. Observations of snow-depth are only available at 6 UTC and 18 UTC, therefore is the snow analysis only performed twice daily [Homleid and Tveter, 2016, Müller et al., 2017].

2.5.2 Meso-NH and the ICE3 scheme

The physical parametrization within AROME is based on the French research communities' mesoscale non-hydrostatic atmosphere model (Meso-NH). The microphysical scheme in the Meso-NH atmospheric simulation system is based on the ICE3 scheme. The purpose of the scheme is to model as correctly as possible the ice phase in the atmosphere [Pinty and Jabouille, 1998]. McCumber et al. [1991] concluded from their case study, that at least three different ice categories are necessary to cover most precipitation but that applications might be case specific. According to the Meteo France [2009] documentation, the ice phase microphysical scheme must include:

r_i: pristine ice phase

r_s: snowflake type from lightly rimed large ice crystals or dry clusters, and

r_g: heavily rimed crystals, such as graupel, frozen drops or hail

Within the ICE3 scheme no distinction between hail and graupel exists and therefore is the physical discrimination in the growth mode of graupel and hail is neglected.

To achieve snow water content within MEPS the total number concentration, slope parameter, mass diameter and the particle size distribution have to be determined. According to Caniaux et al. [1994] follows the particle size distribution the Marshall-Palmer distribution similar to Equation (2.4.8). The goal is to use a varying number concentration N_0 dependent on the ice category. The study has shown that N_0 can be assumed with

$$N_0 = C\lambda^x \tag{2.5.1}$$
$$\log_{10} C = -3.55x + 3.89$$

where C and x depend on the ice category and represent the relation between each other in Equation (2.5.1).
The ice water content for primary ice, snowflakes and rimed crystals is then be assumed to be similar to Equation (2.4.1), but the integration limits range from zero to infinity and mass, and particle size distribution are dependent on the diameter of the particle. The mass diameter and particle size distribution (Equations (2.5.2) and (2.5.3)) are represented depending on the ice category shown in Table 2.5.1

$$m(D) = aD^b \tag{2.5.2}$$
$$n(D) = N_0 g(D) \tag{2.5.3}$$

and $g(D)$ to be the generalised Gamma function

$$g(D) = \frac{\alpha}{\Gamma(v)} \lambda^{\alpha v} D^{\alpha v - 1} \exp\left(-(\lambda D)^{\alpha}\right) \tag{2.5.4}$$

with α, v the shape and tail dispersion parameters and $\Gamma(v)$ the gamma function.
After following the above equations including Equation (2.4.1) the slope parameter λ can be generated with $G(B)$ the gamma function.

$$\lambda = \left(\frac{\text{SWC}}{aCG(b)}\right)^{\frac{1}{x-b}} \tag{2.5.5}$$

Meteo France [2009] documentation suggests starting the microphysics in the ICE3 scheme with 'slow' processes such as homogeneous and heterogeneous nucleation (HON, HEN), vapour deposition of snow and graupel particles (DEP), aggregation (AGG) and auto conversion (AUT), for ice processes right side in Figure 2.5.2. The second step is to initiate the

Table 2.5.1: Characterization parameters from primary ice (r_i), snowflakes (r_s) and rimed crystals (r_g). Values are based on the references in Meteo France [2009] and in Pinty and Jabouille [1998].

	$\mathbf{r}_i$	$\mathbf{r}_s$	$\mathbf{r}_g$
α, ν	3.3	1.1	1.1
a	0.82	0.02	196
b	2.5	1.9	2.8
c	800	5.1	124
d	1.0	0.27	0.66
C		5	5×10^5
x		1	-0.5

warm processes left side in Figure 2.5.2. Then include the aggregation and conversion-melting (CVM) for snowflakes and contact freezing of raindrops (CFR). Add AGG and melting for graupel (MLT), and then the melting from pristine ice and the Wegener-Bergeron-Findeisen (BER) effect and lastly the sedimentation terms.
Figure 2.5.2 shows the summary of the microphysical processes for mixed phase clouds. The study focuses mostly on solid precipitation particles and therefore only the initiation and growth of pristine ice crystals r_i, snowflakes r_s, and rimed crystals r_g is presented.
Following Pinty and Jabouille [1998] and Figure 2.5.2 it can be seen how AROME performs the ice production. Orange lines in Figure 2.5.2 show the initiation of pristine ice crystals and snowflakes. In purple the growth mechanisms of r_i (BER,DEP). Green lines demonstrate the expansion of the snowflakes (RIM, AGG, ACC). Graupel (r_g) forms as an effect of heavy riming (RIM), by collision of larger raindrops with snowflakes (ACC), by WET/DRY growth or by contact freezing of raindrops (CFR). All graupel growth processes are indicated by blue lines in Figure 2.5.2, were hail formation is included.

2.5.3 Adjustment of ICE3 inside MEPS

Since the ICE3 scheme showed some weaknesses for the winter month, Müller et al. [2017] introduced some modifications. During cold conditions the ICE3-scheme showed too low temperature at two meter, too much ice fog and all year long was the occurrence

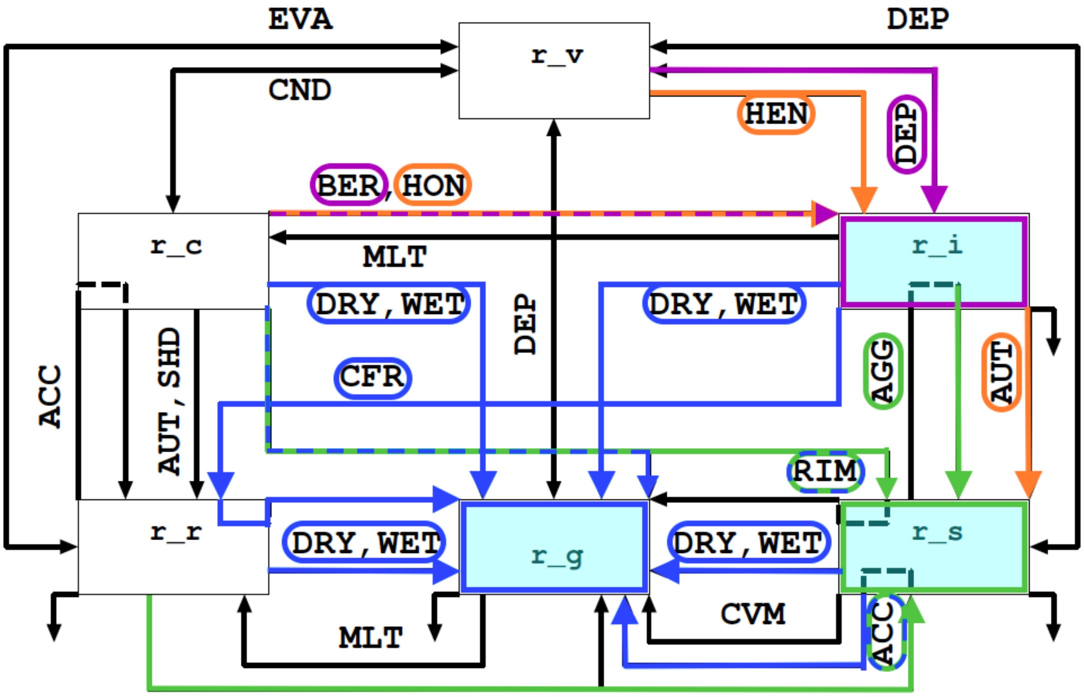

Figure 2.5.2: Microphysical processes for mixed phase clouds in the ICE3 scheme adapted from Meteo France [2009]. In orange the initiation processes for primary ice r_i and snowflakes r_s. The growing processes of r_i is shown in purple and for r_s in green. Graupel particles, r_g, grow from existent particles and the processes are shown in blue.

of cirrus overestimated. After implementing the modifications described in Müller et al. [2017] the two meter temperature bias was reduced as well as an improvement of low-level clouds was shown. A negative aspect of these adjustments was that the occurrence of fog increased.

2.6 Numerical data transformation

The following section will describe how the different variables where processed to achieve a comparison between the retrieved values and the forecast model output.

2.6.1 Layer thickness in MEPS

To compare the measurements from the surface with the MEPS data, the closest grid point to Haukeliseter, is used.
MEPS has a vertical resolution in hybrid sigma pressure coordinates, were one is at the surface and decreases with height. To calculate the actual vertical pressure in Pa, a formula is provided in the OPeNDAP Dataset of `meps_full_2_5km_*.nc` by the Norwegian Meteorological Institute [2016].

$$p(n,k,j,i) = a_p(k) + b(k) \cdot p_s(n,j,i) \qquad [\mathrm{Pa}]. \tag{2.6.1}$$

p_s is the surface air pressure in Pa, and information about the variables a_p, b are not given from the access form. Find reference for sigma-hybrid coordinate transformation equation.
The next step was to convert pressure-levels into actual heights by the use of the hypsometric equation. Here, the air temperature in model levels is used to calculate the mean temperature of each layer.

$$\overline{T} = \frac{\int_{p2}^{p1} T \partial lnp}{\int_{p2}^{p1} \partial lnp} \qquad [\mathrm{K}] \tag{2.6.2}$$

For the numerical integration, the Simpson rule was used, which is a build-in function in Python.
Martin [2006] presents steps of differentiating the hypsometric equation by using the virtual air temperature. But when the atmospheric mixing ratio is large, will the virtual temperature only be 1 % larger than the actual air temperature. Since the error is little calculations are done with the provided air temperature in model levels.
The thickness, Δz, of each layer is then be found by using the hypsometric equation from Martin [2006] and the previously calculated mean temperature (Equation (2.6.2)):

$$\Delta z = z_2 - z_1 = \frac{R_d \overline{T}}{g} ln\left(\frac{p_1}{p_2}\right) \qquad [\mathrm{m}] \tag{2.6.3}$$

where R_d is gas constant for dry air with a value of $287\,\mathrm{J\,kg^{-1}\,K^{-1}}$, standard gravity $g = 9.81\,\mathrm{m\,s^{-2}}$. p_1 and p_2 are the pressure levels at lower and higher levels, respectively ($p_2 < p_1$). To gain the respective height of each pressure layer, Δz is summed.

2.6.2 Snow water content

To get a valid comparison between the SWC from the optimal estimation retrieval and the results from MEPS, the SWC is averaged over each hour. Taking the model initialisation of MEPS at 0 UTC the model produces forecast values at 0, 1, 2, ..., 22, 23, ..., 66 UTC. To approach hourly mean values from the retrieval SWC an average over 30 min prior and 29 min after each full hour is performed. This leads to a match of the average value at the same time as from MEPS.
Since MEPS has a higher vertical resolution than the optimal estimation snowfall retrieval each vertical profile of SWC is averaged every 200 m. To accomplish the same vertical resolution only values above 100 m are used to start at the same range height as given from the MRR (Section 2.3.2).
Within the output from MEPS snow water content does not exist for each model layer. Hence the calculation of the SWC is performed by using the three solid precipitation categories given in MEPS. Namely the instantaneous mixing ratio of snowfall (r_s), graupel fall (r_g) and the atmosphere cloud ice content (r_i). The mixing ratios are represented in kg kg^{-1} and a transformation to g m^{-3} is performed. Densities in each model level (ρ_{ml}) are calculated and then multiplied with the sum of the solid precipitation mixing ratio.

$$\rho_{ml} = \frac{p_{ml}}{R_d T} \qquad [\mathrm{kg\,m^{-3}}] \tag{2.6.4}$$

$$SWC_{ml} = \rho_{ml} \cdot (r_s + r_g + r_i)_{ml} \cdot 10^6 \qquad [\mathrm{g\,m^{-3}}]. \tag{2.6.5}$$

2.6.3 Snow water path

The snow water path (SWP) is the vertically integrated value of the averaged SWC (Equations (2.4.1) and (2.6.5)), where the numerical Simpson's integration is applied.

$$\int_{h_0}^{h_1=3000\,\mathrm{m}} \mathrm{SWC}(h)\,dh \approx \frac{h_1 - h_0}{6}\left[\mathrm{SWC}(h_0) + \mathrm{SWC}(h_1) + 4\mathrm{SWC}\left(\frac{h_0 + h1}{2}\right)\right] \qquad [\mathrm{g\,m^{-2}}] \tag{2.6.6}$$

The snow water path is a measure of the weight of ice particles per unit area. It indicates the total amount of ice in the atmosphere.

2.6.4 Ensemble mean and Coefficient of Variation

Check literature of meaning

The ensemble mean is the average of all ten ensemble members of MEPS.

$$\bar{x} = \frac{\sum_{i=1}^{n} x_i}{N} \tag{2.6.7}$$

The ensemble spread is known as the standard deviation with respect to their mean of the model output. That means it shows the variation around the center or control run.

$$\sigma = \sqrt{\frac{\sum_{i=1}^{n} (x_i - \bar{x})^2}{N-1}} \tag{2.6.8}$$

for either variable is the dimension of the standard deviation the same.
To verify how well MEPS performed during the Christmas storm a variation of the SWC is calculated. For this, the standard deviation (Equation (2.6.8)) is divided by the ensemble mean (Equation (2.6.7)).

2.6.5 Dew point temperature for Skew-T log-P Diagram

The Python module `pyMeteo` is used to calculate the dew point temperature of each ensemble member to study the stability of the atmosphere (https://pythonhosted.org/pymeteo/, last visited: 25.01.2018). The additional package `thermo.py` is able to calculate the dew point temperature if the pressure and the specific humidity in each level are known.

$$e_l = ln\left(\frac{\frac{q_v}{\epsilon} \cdot \frac{p}{100}}{1 + \frac{q_v}{\epsilon}}\right) \tag{2.6.9}$$

$$T_d = 273.15 + \frac{243.5 \cdot e_l - 440.8}{19.48 - e_l} \qquad [\mathrm{K}] \tag{2.6.10}$$

where, q_v is the specific humidity, p pressure in [Pa], $\epsilon = R_d/R_v = 0.622$ with R_v gas constant for water vapour.

Chapter 3: Analysis of the Christmas Storm 2016

Extreme storm Urd was chosen for an in depth examination for a number of intriguing reasons: i) the MEPS forecasting system had recently become the operational model platform for Met-Norway, ii) the Haukerlister site is a WMO sanctioned weather station with single and double fence rain gauge measurements, iii) additional instruments were placed at the site for the winter 2016/2017 season allowing for the vertical profiling of snow properties and snowfall accumulation, and iv) the unique temporal evolution of the precipitation properties during the event.

A preliminary analysis identified periods of both good agreement of snow accumulation measurements by MEPS in comparison to the ground observations, as well as periods of overestimation by MEPS. The above factors make for an interesting study to assess and better understand the usefulness of the measurements in question.

The next sections will provide a definition of an extreme weather event, a description of the weather maps that were utilized, and a presentation of the synoptic scale evolution of the storm.

Prior to the analysis, each weather maps' purpose will be presented to understand the connections between them. All the weather maps are generated using data from ECMWF operational model Cycle 43r1. The analysis consists of 137 model levels and to reduce computational costs is it reduced to the *octahedral reduced Gaussian grid* and then interpolated to a N640 Gaussian grid.

Between the pole and the equator are 640 lines of latitude equally symmetric spaced. This follows 1280 latitude lines for each hemisphere. The resolution along the longitude is 90°/640 lines with points getting closer with increasing latitude. This follows a total number of grid points of $8 \cdot 640^2$ [Dando, 2016].

3.1 Extreme weather

'Extreme weather' is a meteorological term, associated with the extent of a weather type. The Norwegian Meteorological Institute declares an extreme event, if strong winds, large amounts of precipitation and large temperature changes are expected before the event occurs. As well as a large avalanche risk is present and coastal areas are influenced by extremely high-water levels. Generally, an event is divided into four phases that it can be called extreme [Pedersen and Rommetveit, 2013].

Phase A: *Increased monitoring before the possible extreme weather.* The meteorologists give special attention to the weather situation. At this point it is not certain, that there will be an extreme weather event.

Phase B: *Short-term forecasts.* It is decided, that there will be an extreme event. The forecasts are more detailed, and updates will be published at least every six hours. The event will get a name.

Phase C: *The extreme weather is in progress.* The meteorologists send out weather announcements at least every six hours.

Phase D: *The extreme weather event is over. Clean-up and repairs are in progress.* When the extreme weather is over the public is notified and information about the upcoming weather and clearing work is given.

The Christmas storm was deemed an extrme event by the Met-Norway, named Urd [Olsen and Granerød, 2017]. The average wind along the coast of Western Norway reached hurricane strength (observed: $40\,\mathrm{m\,s^{-1}}$ to $55\,\mathrm{m\,s^{-1}}$). In South and Eastern Norway, west to north-west winds between $25\,\mathrm{m\,s^{-1}}$ to $40\,\mathrm{m\,s^{-1}}$ were measured. At Haukeliseter, 136.4 mm of precipitation were measured from 21 to 27 December 2016. The event was just above the limit of been called an extreme weather event.

3.2 Dynamic Tropopause map

The dynamic tropopause maps (DT), presented herein are comprised of the potential temperature (shading) and wind barbs $[\mathrm{m\,s^{-1}}]$ on the two PVU surface (one PV unit =

$10^{-6}\,\mathrm{m^2\,s^{-1}\,K\,kg^{-1}}$), and the 925–850 hPa averaged relative vorticity (black contours - every $0.5\times10^{-4}\,\mathrm{s^{-1}}$ only positive values are plotted). An example is presented in **??**. High (low) values of potential temperature represent and elevated (suppressed) tropopause. Regions with a large horizontal gradient of potential temperate indicate a steeply-sloping tropopause that is associated with an enhanced pressure gradient force and winds. The low-level averaged relative vorticity is plotted to provide a 3-dimensional (in the vertical) picture of the atmosphere. It is useful for identifying cyclone centres and attendant frontal boundaries.

The 925 –850 hPa layer-averaged surface relative vorticity is shown in black contours, every $0.5\times10^{-4}\,\mathrm{s^{-1}}$. It represents the rotation of a fluid. Does the relative vorticity need more explanation?
Along the Rossby-Wave-Guide Define what I mean by Rossby-Wave-Guide, troughs and ridges are seen which can be combined with the surface relative vorticity to understand the vertical dynamic interaction in the atmosphere. In case of a westward tilt between the surface cyclone and an upper level through an intensification of the surface cyclone is more likely to occur.

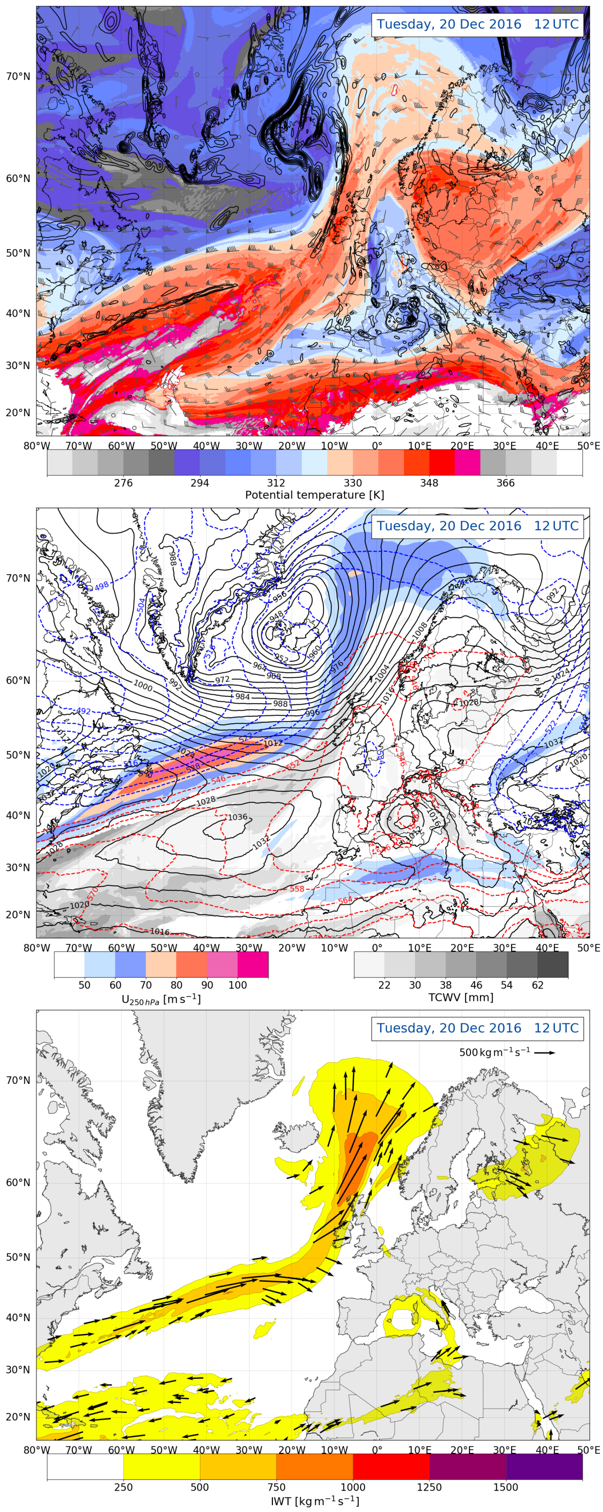

a: Dynamic tropopause analysis map at 2 PVU. Potential temperature [K] at the 2 PVU surface, shaded according to the colour bar. Total wind, barbs [m s^{-1}], and 925 −-850 hPa layer-averaged surface relative vorticity (black contours, every 0.5×10^{-4} s^{-1}).

b: Jet, thickness, mean sea level pressure, and moisture synoptic analysis. 250 hPa wind speed, shaded according to the colour bar, [m s^{-1}]. 1000 −500 hPa thickness, dashed contours every 6 dam, MSLP, black contours every 4 hPa, total column water vapour [mm], shaded according the grey scale.

c: Atmospheric river analysis map. IVT, shaded according to the colour bar [kg m^{-1} s^{-1}]. Vectors, indicating the direction and magnitude of the IVT.

Figure 3.2.1: ECMWF analysis on 20 December 2016 at 12 UTC.

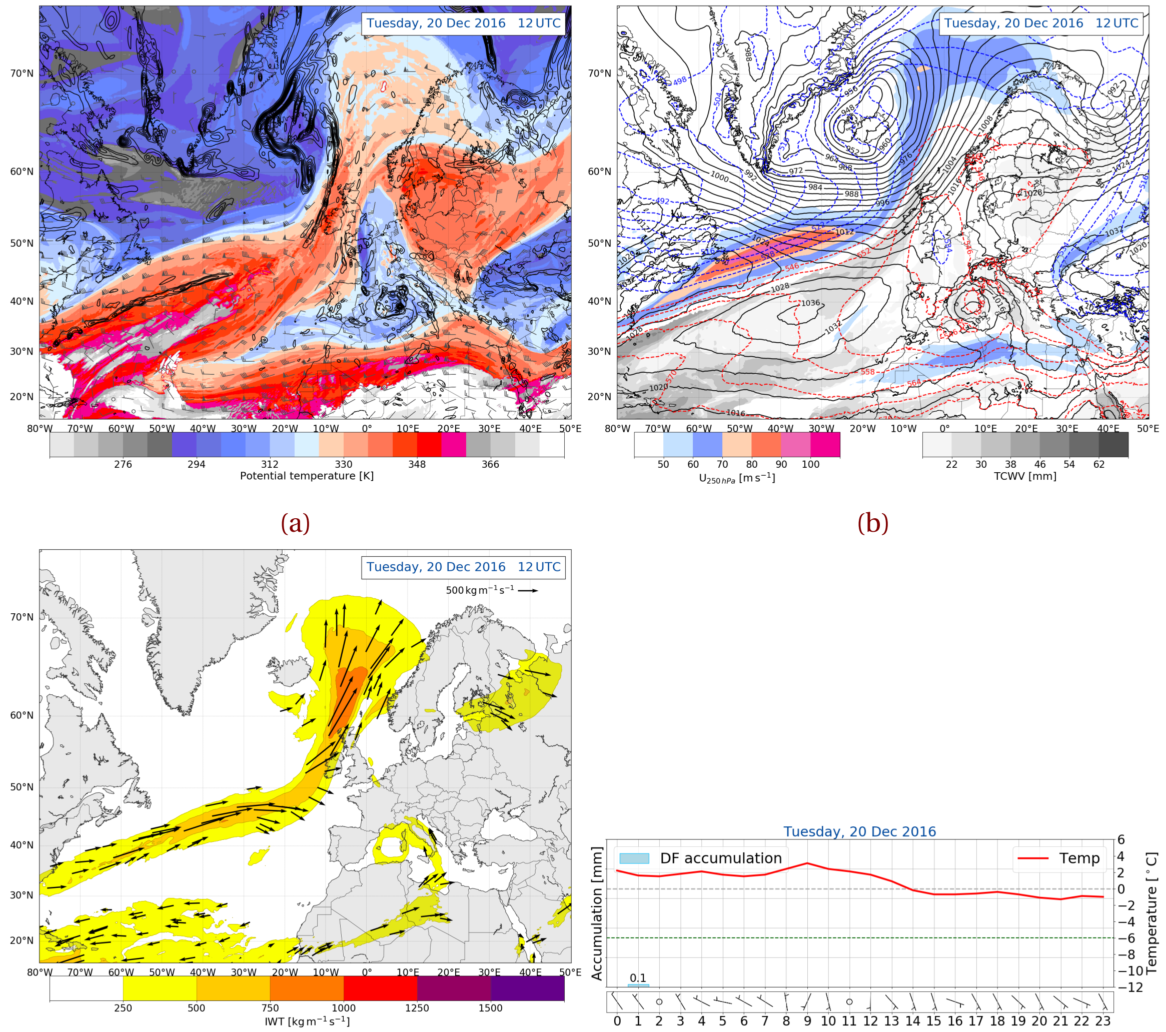

(a) (b)

(c) (d)

3.3 Thickness, Sea Level Pressure, Total Precipitable Water, and wind at 250 hPa

A complementary view of the 3-dimensional structure of the atmosphere is also presented: 250 hPa wind speed (color shading, m s^{-1}), mean sea level pressure (black contours, hPa), 1000–500 hPa thickness (dashed contours) and the total precipitable water (black-white shading, mm). See Figure 3.2.1 for an example.

The dashed, coloured contours show the vertical thickness between the 1000 hPa and

500 hPa surface, every 6 dam. The thickness between two pressure levels can be interpreted via the hypsometric equation (Equation (2.6.3)), which equates the thickness to the mean temperature of the layer in question. In a relative sense, a larger thickness indicates a warmer air mass. In addition, strong horizontal gradients in the thickness field can be related to frontal boundaries. Specific to the discussion herein, the thickness field is also provides useful information regarding the form of precipitation (rain, snow)..
Analysis of the mean sea level pressure can be used to identify cyclones and anticyclones at the surface as well as provide supplementary information regarding frontal boundaries. The total precipitable water is a measure of the column integrated moisture. The 250 hPa wind speeds are used to identify strong upper-level flow (i.e. the jet stream) and can be directly compared to the DT map. It represents an instantaneous measure of moisture in time and space, which can be useful when assessing the amount of moisture that may fall as precipitation in future time steps.

3.4 INTEGRATED VAPOUR TRANSPORT

Figure 3.2.0c shows coloured contours of the integrated vapour transport (IVT) in $\mathrm{kg\,m^{-1}\,s^{-1}}$, where warmer colours indicate higher IVT. Stream vectors indicate the direction and intensity of the IVT flow. An atmospheric river is characterised if the integrated vapour transport shows values higher than 250 $\mathrm{kg\,m^{-1}\,s^{-1}}$ and a continuous region larger than 2000 km [Rutz et al., 2014].
An atmospheric river (AR) is a filament structure of intense moisture transport from the tropics to higher latitudes. Heavy precipitation can be associated with it, because the air is warm and moist. This can often be observed at mountain ranges at west coasts such as in Norway include reference here. Due to orographic lifting will the moisture be released and follow high amounts of precipitation.
The integrated vapour transport (IVT) was calculated from the ECMWF data as followed:

$$IVT = \frac{1}{g} \int_{p_{sfc}}^{100\,\mathrm{hPa}} q\mathbf{V}dp \qquad [\mathrm{kg\,m^{-1}\,s^{-1}}] \tag{3.4.1}$$

where g is the standard gravity, q the specific humidity, and $\mathbf{V}$ the total wind vector at each pressure level p. The numerical, trapezoidal integration is performed by using data

Table 3.5.1: Damage related to wind speed, from Færaas et al. [2016].

slight storm	$20.8\,\mathrm{m\,s^{-1}}$ – $24.4\,\mathrm{m\,s^{-1}}$	Large trees sway and hiver. Roofs can blow down.
full storm	$24.5\,\mathrm{m\,s^{-1}}$ – $28.4\,\mathrm{m\,s^{-1}}$	Trees are pulled up with clutter. Big damages to houses.
strong storm	$28.5\,\mathrm{m\,s^{-1}}$ – $32.6\,\mathrm{m\,s^{-1}}$	Extensive damage.
hurricane	$>32.6\,\mathrm{m\,s^{-1}}$	Unusually large destruction.

from the surface pressure p_{sfc} to 850 hPa in 50 hPa intervals and from 700 hPa to 100 hPa in 100 hPa intervals.

3.5 Observations at the weather mast

It is a primary goal of this work to relate the local weather observations from the WMO site at Haukeliseter to the synoptic scale structure and the additional measurements taken at Haukeliseter during the winter of 2016/2017.
Examples of the 60 min precipitation accumulation from the double fence rain gauge are presented in **??** to document the continuous precipitation at Haukeliseter during the extreme event. The temperature evolution will be used to investigate possible changes in the type of precipitation.
Snowfall is likely for temperatures up to 2 °C. The intensity of the storm can be classified by the hourly averaged wind speed and direction as wind barbs in $\mathrm{m\,s^{-1}}$. To understand which damage a storm can have, Færaas et al. [2016] released a table to associate wind strength with damage (see Table 3.5.1).

Chapter 4: Results and Discussion

In this chapter the results of the surface observation, the optimal estimation retrieval and the regional mesoscale forecast model are presented. On the basis of the methodology described in Chapter 2 it should be evaluated if a regional mesoscale forecast model predicts the same synoptic patterns as observed at the measurement site. Also, vertical SWC forecasted by MEPS is being verified with the retrieved vertical SWC at Haukeliseter. Attention should be paid to the fact, that this study study is very unique of its kind. As far as the author has knowledge was no approach done to verify a vertical regional forecast model with the help of vertical observation measurements.

4.1 Comparison of surface observations

To be able to compare the vertical predicted snow water content with the retrieved snow water content a verification of the surface accumulation is made. If the retrieved surface accumulation is confident in comparison to the double fence measurement, then the vertical measurements can be trusted.

The correlation in Figure 4.1.1a demonstrates a good agreement between the 48 h accumulation measured by the double fence and the retrieved surface accumulation. The black line in Figure 4.1.1a presents a linear correlation with a regression coefficient of R = 0.97. In general, the retrieved surface snowfall accumulation is underestimated when compared to the double fence measurements, but not to a large degree.

Figure 4.1.1b shows the difference between retrieved accumulation and observed accumulation by the double fence. For the time period 20 to 24 December 2016, Figure 4.1.1b indicates an underestimation of retrieved snow accumulation of less than -5 mm for the first 24 h. Snow accumulation calculated on 23 December 2016 at 0 UTC show after

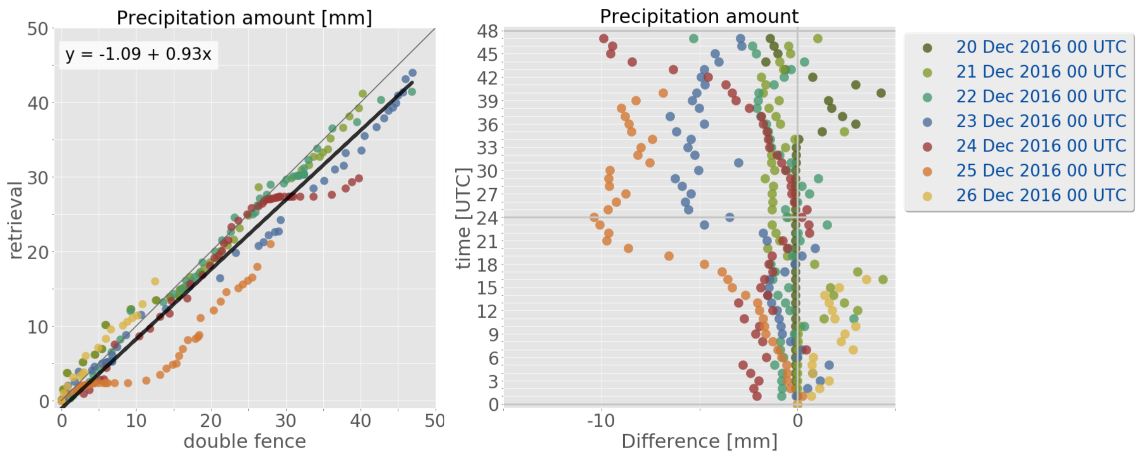

(a) (b)

Figure 4.1.1: a: Surface precipitation amount comparison between the double fence observations and the retrieved surface accumulation of precipitation for 48 h. In black the linear correlation between the double fence observations and retrieved surface snow. b: Difference between the retrieved and the observed accumulation by the double fence. The colours represent the different starting days at 0 UTC for the 48 h accumulation.

24 h an underestimation by the retrieval of up to −6.5 mm. Larger underestimation after 43 h is related to the observation of liquid precipitation on 25 December 2016 between 12 UTC to 21 UTC for accumulations on 24 December 2016. On 25 December 2016 no fair comparison to the double fence measurement can be performed after 12 UTC because of the neglection of liquid precipitation when temperatures exceed 2 °C.

For a 12 h accumulation follows for the Christmas storm (20 to 26 December 2016) an average error of 85.5 % (Table 4.1.1). For longer, 24 h accumulation decreases the average error to be −4.7 % (excluding values on 25 December 2016 after 12 UTC and on 26 December 2016 after 17 UTC because of attenuation at the MRR). The daily surface snowfall accumulation difference between retrieval and observation in Table 4.1.1 show almost always a well agreement to the boundary condition of the double fence. The only well pronounced mismatch is seen non 21 December 2016, where it measures much more than the double fence gauge (+435.8 %).

Similar to this study, Cooper et al. [2017] used a CloudSat snow particle model, PSD and fall speed from MASC observations for five snow events at Barrow, Alaska. The comparison to the weather station revealed an difference between National Weather

Table 4.1.1: Comparison of observed (obs.) and retrieved (ret.) snowfall amounts for the Christmas storm 2016. Difference refers to the difference of the retrieved and observed snow accumulation after 12 h and 24 h. The average difference is the value over all six/four days. Excluding values after 12 UTC on 25 December 2016 and after 17 UTC on 26 December 2016.

Day in 2016	12 h **accumulation**				24 h **accumulation**			
	Snowfall		**Difference**	**Average difference**	**Snowfall**		**Difference**	**Average difference**
	obs.	**ret.**			**obs.**	**ret.**		
	[mm]		[%]	[%]	[mm]		[%]	[%]
20 Dec	0.1	0.0	−97.8		0.1	0.0	−97.8	
21 Dec	0.7	3.8	+435.8	+85.5	17.1	16.6	−2.7	−4.7
22 Dec	13.6	13.2	−3.0		25.6	25.1	−2.1	
23 Dec	6.3	5.2	−16.8		23.3	19.8	−14.9	
24 Dec	14.7	13.4	−8.6		24.8	25.0	+0.8	
25 Dec	4.3	–	–		+15.4	–	–	
26 Dec	8.8	10.6	+20.1		25.1	–	–	

Service observations and retrieved accumulations of −18 % for all five snow events.

Table 4.1.1 shows the difference for each individual day and the average difference for six and 4 days, depending on the accumulation of 12 h or 24 h. The choice of the correct PSD model, slope parameters and fall speed in the optimal estimation snowfall retrieval, shows a good agreement with the observations at Haukeliseter for the 2016 Christmas storm in contrast to the 200 % difference when only using the CloudSat snowfall algorithm Section 2.4. It indicates also that the non-uniqueness of snow accumulation is reduced, when using a combination of ground-based observations instead of only Ze-S relationships. During the 2016 Christmas storm the average error for 24 h accumulation is almost similar to Barrow, Alaska. It turns out that there is no relation between high and low precipitation events since the differences vary. Cooper et al. [2017] also showed different combinations of PSD assumptions and snow fall speed. For Barrow, best agreements between observations and retrieved snowfall were found by using the CloudSat particle model, slope parameters and snowfall speeds from the MASC. The here presented work (Section 2.4) uses a particle model based on observed particle sizes during the entire winter 2016/2017, like in Figure 2.3.5. Add Discussion on different combination/parameters as discussed with Steve.

On 20 and 21 December 2016, the difference error is large (−97.8 % and 435.8 %, respectively). This is probably related to an observation of precipitation at the double fence, even though no precipitation was observed. The double fence observation might be related to some particles stirred up by wind into the orifice of the gauge. Since no manual observations are done at the Haukeliseter site, is it difficult to say if blowing snow occurred and might introduce additional errors. But from the vertical MRR reflectivity it can be seen, that precipitation was not observed on before 21 December 2016 9 UTC.
Even though it is assumed that the double fence is the absolute correct measurement it still underlies some uncertainties. A better way to asses the accuracy of the retrieved surface snowfall accumulation could be to compare the results to measurements inside a bush gage. A bush gauge is a precipitation gauge surrounded by a large bush to create artificial calm winds to increase the catch ratio of frozen precipitation and is considered as the best available measurement for solid precipitation [Wolff, 2018]. Unfortunately there are only two bush gauges in the world, and because of local limitations a double fence construction is developed as reference for the Solid Precipitation Measurement intercomparison study during 1986 to 1993 [Goodison et al., 1998]. Comparisons between bush gauge and double fence precipitation measurements have shown, that for wind speeds up to 9 $\mathrm{m\,s^{-1}}$ outside the fence, the double fence will measure up to 10 % less precipitation. While wind speeds outside the double fence might reach 20 $\mathrm{m\,s^{-1}}$ show measurements inside a decrease to 5 $\mathrm{m\,s^{-1}}$. Wolff [2018] believes the underestimation of the double fence will not be more than 20 % during frozen precipitation events with high wind speeds.
The low average difference value for 24 h accumulation, in Table 4.1.1 during the Christmas 2016 event (−4.7 %) follows a much lower average difference between retrieved and observed surface accumulation than at Barrow (36 %) and therefore a very good agreement between observed and retrieved snow accumulation during 21 to 24 December 2016. In **??**, the vertical SWC will be compared to the forecasted MEPS values for the 2016 Christmas storm. Despite the condition that the double fence measurement is influenced by wind will the small average difference for 21 to 24 December 2016 give confidence in

the retrieved profiles of snow water content when comparing to the forecast, but it should be kept in mind that retrieved snow accumulation is underestimated and therefore may the vertical SWC be too low.

4.2 Observation and predictions of large scale weather phenomena at the surface

One of the main factors, that made the Christmas 2016 storm so interesting is the fact, that fronts passed over Norway during the six-day period. One aim of this work is to determine if large scale features were observed at the measurement site during the extreme event.
A comparison between the surface observations at Haukeliseter and the ECMWF analysis of the dynamic tropopause and geopotential thickness maps show that frontal passages occurred on three days during the Christmas storm (**??** and **??**). A typical cyclone has a prevailing warm front and a faster moving cold front. As the storm gets more intense and the cold front rotates around the low-pressure centre and catches the warm front the cyclone will begin to occlude. Changes in pressures, temperature, wind direction and wind speed can occur. In some cases, an intensification of the precipitation can be observed as well.
Figure 4.2.1 shows the different parameters forecasts initialised at 0 UTC for 23 December 2016, 25 December 2016 and 26 December 2016, as well as the observations at the Haukeliseter measurement site in dash-red. Typical pressure decreases and increases, as well as temperature increases, and wind changes are present on 23 December 2016 and 26 December 2016, since these changes show in the surface observations in Figure 4.2.1, it is assumed that frontal boundaries passed. The 25 December 2016 shows only an increase of temperature leading to the assumption of a warm air passage in Figure 4.2.1d.

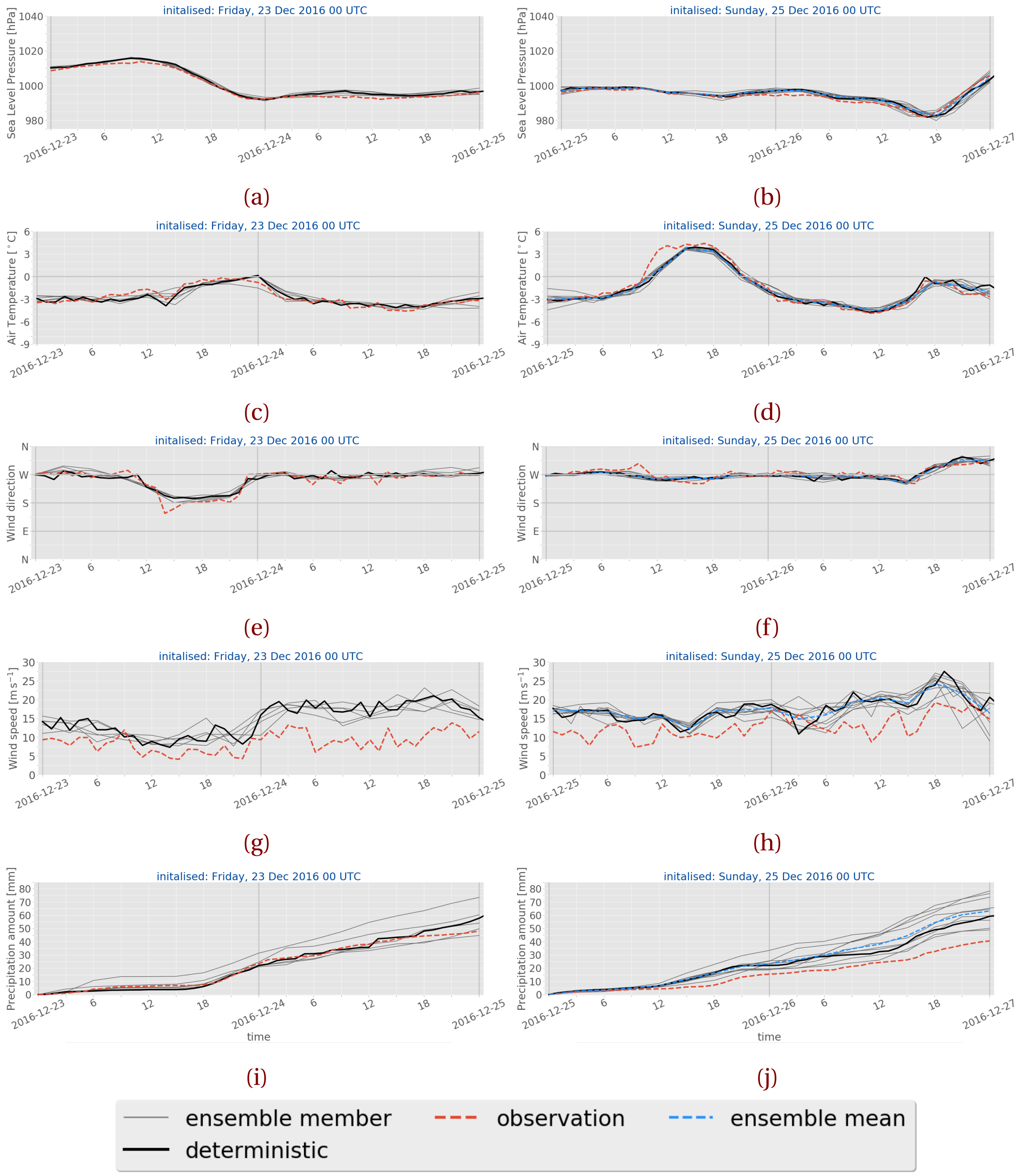

Figure 4.2.1: 48 h surface observations and ensemble forecasts initialised on the 23 December 2016 at 0 UTC (left column, a, c, e, g, i), and on 25 December 2016 at 0 UTC (right column, b, d, f, h, j) as well as 26 December 2016 (k, l, m, n, o). Line representation according to the label. Upper panel sea level pressure, second 2 m air temperature, third and fourth 10 m wind direction and speed, respectively, and lowest panel precipitation amount.

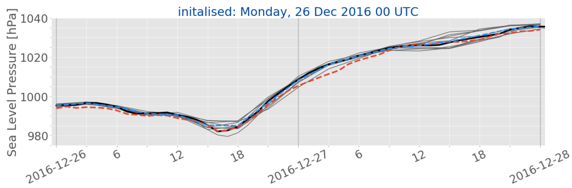

(k)

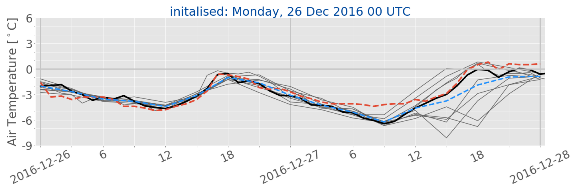

(l)

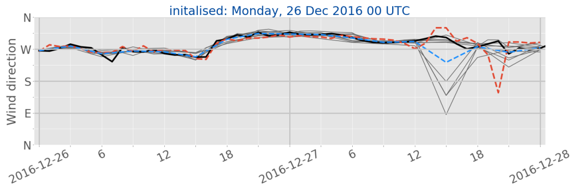

(m)

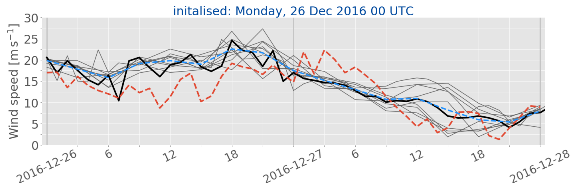

(n)

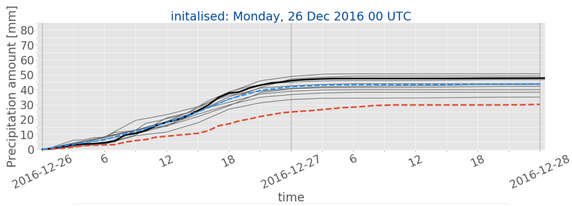

(o)

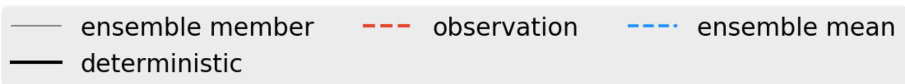

Figure 4.2.1: *(Continued from previous page.)* Initialisation 26 December 2016 at 0 UTC.

As described in **??** shows the ECMWF dynamic tropopause analysis map (**??**) more ridging and therefore warmer air over Southern Norway on 23 December 2016. The low-pressure system approaches in the course of the day south-east of Iceland and hence stronger west to south west wind are associated with the cyclone (**??**). The MEPS forecast, initialised on 23 December 2016 at 0 UTC in Figure 4.2.1a follows the observations and shows the decrease in pressure after 12 UTC due to the passage of the occluded front with a constant pressure after the transition. Since warmer air is more advected to the north and the DT in **??** shows a warm low-pressure core, an increase in temperature was observed and predicted at the measurement site (Figure 4.2.1c).
As the cyclone is advected to the north-east, closer into the Norwegian Sea, a wind change can be seen in the analysis map from ECMWF (**??**). First west wind and later south-west wind was associated with the low-pressure system. The MEPS forecast and observations in Figure 4.2.1e and g indicate a wind change from west to south with a slight decrease in wind speed.
On 23 December 2016 was the passage of the occlusion also observed by an increase in precipitation. Before 18 UTC shows the surface accumulation light precipitation. During the passage of the occluded front increases the observed surface accumulation and is associated to continuous, heavy precipitation.

Similar patterns were seen for the passage of the occluded front on 26 December 2016 in the ECMWF analysis **??** and **??**. In this case the low-pressure system was located north of Morø og Romsdal in the Norwegian Sea. In the morning was the cyclone located east of Iceland and in the course of the day it got closer to the coast of Norway. Before landfall at 16 UTC indicates Figure 4.2.1k a pressure decrease. During the passage the sea level pressure reaches its lowest point of 985 hPa and increased afterwards during the dissipation of the Christmas storm. Pressure, temperature, and wind changes were already forecasted for initialisations on 25 December 2016 (Figure 4.2.1b, d, f, h), only wind speed and precipitation seem not to agree with the observations at Haukeliseter.
Since the cyclone was surrounded by colder air (south of the low-pressure system) first a drop and then an increase of temperature were observed and forecasted by MEPS. An indication of the passage is also seen in the 10 m wind observations and forecasts. As the cyclone is east of Iceland with a westward large-scale surface wind (**??** and **??**), shows Figure 4.2.1m and n west wind with observed strength up to 17.5 m s^{-1}. During the

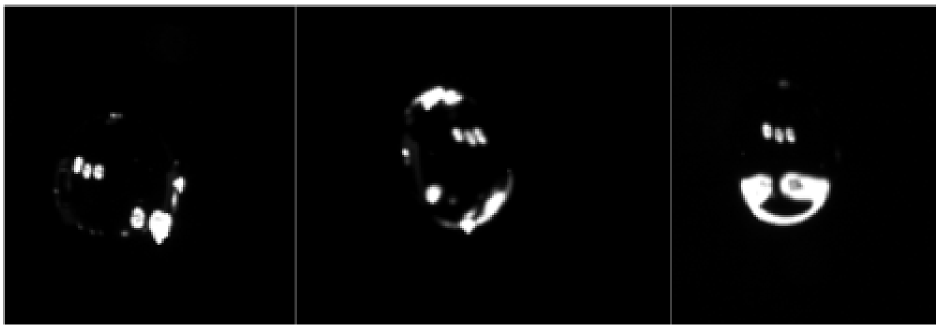

Figure 4.2.2: MASC images of falling water drops observed on 25 December 2016 at 17 UTC from three different angles. Not all parts of the liquid sphere are equally illuminated.

passage changes the wind direction to north-west with higher wind speed which can be associated to the location of the low-pressure system and the closer surface isobars (**??**). The precipitation was continuing throughout the day, with light to moderate precipitation before the passage and heavy precipitation around 16 UTC followed by moderate to light precipitation.

While on 23 December 2016 and 25 December 2016 the precipitation was associated with a passage/landfall of an occluded front, was the 25 December 2016 marked by the transition of a warm sector. The ECMWF analysis showed a ridging at the DT surface. The surface cyclone core is south east of Iceland in **??** with two associated frontal boundaries. While the warm front is approaching the west coast, is the cold front north-west of Great Britain. The cold fronts tail moved into lower latitudes, following the slowdown of the cold front, leading to a stationary frontal boundary. Furthermore, the mid-latitude jet is aligned along the surface frontal boundaries (**??**), while the Haukeliseter site is located below the left jet exit region. This leads to rising motion at the surface.
Neither pressure nor wind observations and forecasts indicate the passage of any frontal boundary. The only indication of the transition is seen in the increase of temperature at 11 UTC until 21 UTC (Figure 4.2.1d). In Figure 4.2.1f a small wind change was observed by the wind mast at 10 UTC. This development from west to north-west was not forecasted by MEPS, it rather estimated strong west winds.
In Figure 4.2.2 are the surface observations from the MASC during the passage of the warm sector. Without the images taken around 17 UTC it would not be possible to verify

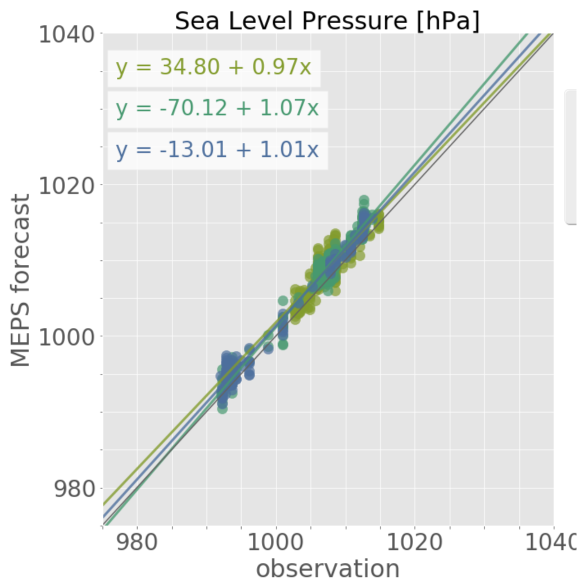

(a)

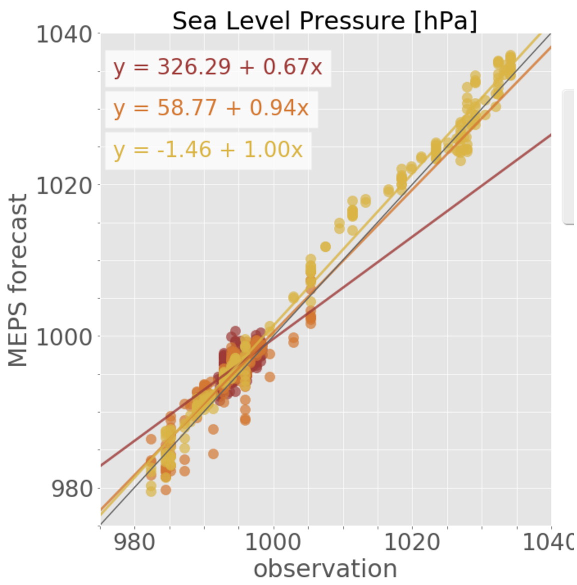

(b)

Figure 4.2.3: 48 h scatter plots for surface observations and ensemble forecasts initialised for 21 December 2016 to 23 December 2016 (left column, a, c, e, g, i) and for 24 December 2016 to 26 December 2016 (right column, b, d, f, h, j). Sea level pressure.

that liquid precipitation occurred at the Haukeliseter site. Together with the increase in surface temperature in Figure 4.2.1d it is qualified that at least the warm sector of the low-pressure system appeared at the measurement site. Should I include the DIANA analysis maps? But I dont know what the meteorologists are using to produce them? ECMWF?

The comparison between the ECMWF analysis displays, that the ensemble member forecast system MEPS covers the prediction of large scale phenomena like frontal boundaries and liquid precipitation at the surface. Figure 4.2.3 presents the correlation between the observations and the 48 h ensemble forecast. The relation between Haukeliseter observations and the forecast members is indicated by the regression line for each day.
Sea level pressure has the best correlation under all variables. The best agreement shows on 26 December 2016 when the Christmas storm made landfall and dissipates after the passage of the occluded front at 16 UTC. Dahlgren [2013] showed that by mixing in large scale information from the boundary condition (ECMWF) into the regional model, the

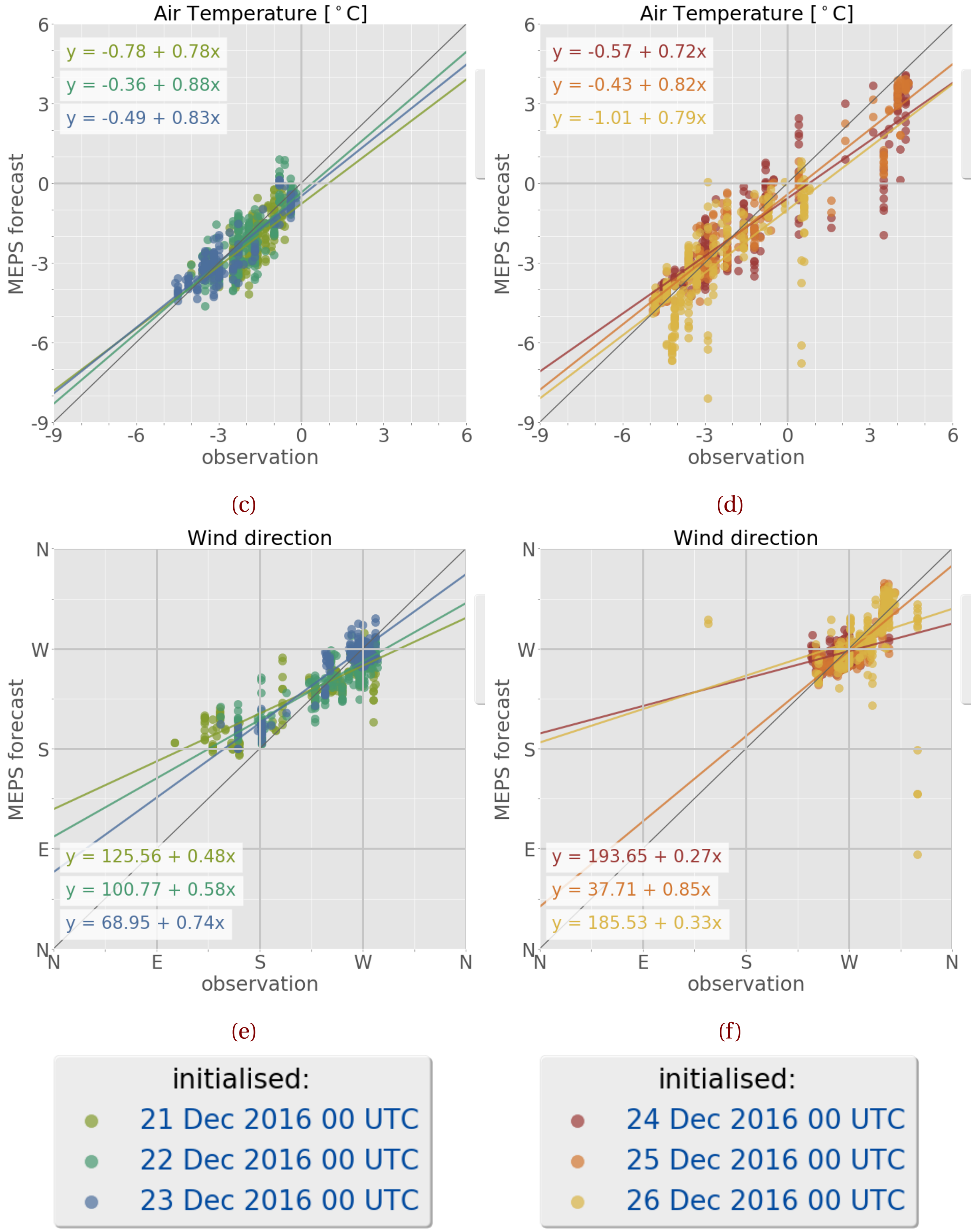

Figure 4.2.3: *(Continued from previous page.)* Upper panel 2 m air temperature, second panel 10 m wind direction.

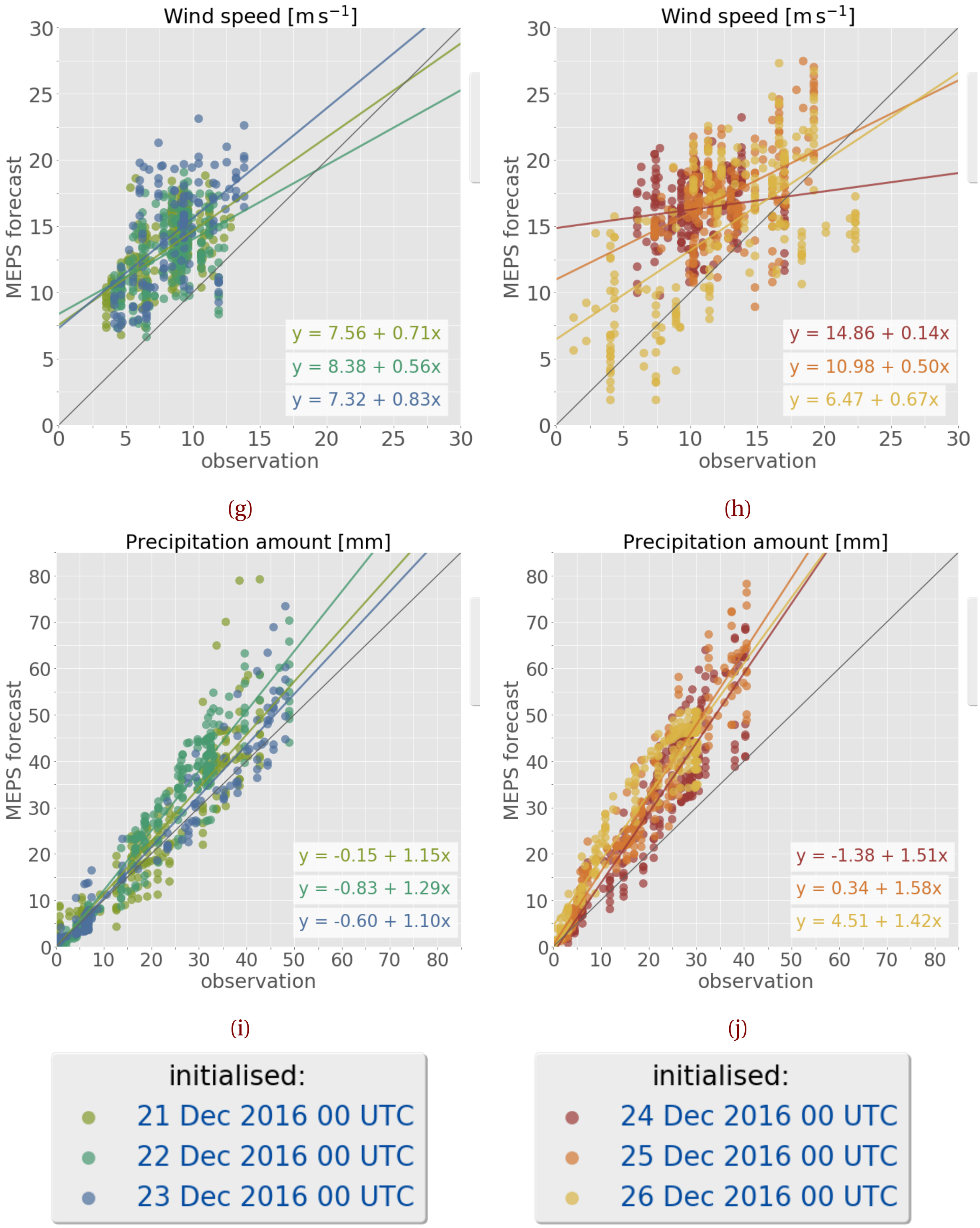

Figure 4.2.3: *(Continued from previous page.)* Upper panel 10 m wind speed, lower panel surface precipitation amount.

forecast for sea level pressure will be improved. The model-observation comparison by Dahlgren [2013] showed a declination of forecasts with pressure mixing after 24 h Since the pressure values are in good agreement with the observations is assumed that the warm front did not pass through at Haukeliseter on 25 December 2016 and only the warm sector is observed. This shows a quite detailed forecast ability of MEPS, as from the ECMWF analysis it is not quite clear where the warm front could have passed through.
Figure 4.2.3d indicates a moderate correlation between observation and the 48 h ensemble member forecast system. In general, underestimated MEPS the observed temperature, but it estimated it at the correct timing on 25 December 2016. The previous operational model AROME-MetCoOp showed a negative winter bias after winter 2012 [Müller et al., 2017]. Figure C.2.1c shows for 23 December 2016 and 26 December 2016 positive as well as negative mean error for the individual members. On 25 December 2016, during the warm sector a negative bias was observed, underestimating the temperature when compared to the observation. The mean error for the Norwegian model domain of AROME-MetCoOP estimated by Müller et al. [2017] is smaller than 1.8 K for the surface temperature in December 2014. The forecasts for 23 December 2016, 25 December 2016 and 26 December 2016 show mean absolute error values of up to 0.61 K, 0.77 K and 1.44 K, respectively. It shows by using an ensemble forecast system a reduction of mean errors and an increase in forecast accuracy can be done.
During the Christmas storm 2016 high wind speeds were observed at the Haukeliseter site (Figure 4.2.3g and h). According to Müller et al. [2017] are large wind speeds significantly better simulated for AROME-MetCoOp compared to ECMWF's forecast. The wind speeds are still overestimated, which is an already known difficulty in the deterministic version of MEPS. In AROME-MetCoOp wind speed prediction agreed better with observations for wind speeds between 3 $\mathrm{m\,s^{-1}}$ to 13 $\mathrm{m\,s^{-1}}$ than ECMWF forecasts did, showing the advantage of a high-resolution weather model. With increasing wind speed the forecast accuracy decreases with a mean absolute error below 2 $\mathrm{m\,s^{-1}}$ for December 2014 in AROME-MetCoOp. The mean absolute error for wind speed during the Christmas storm is higher at all days ranging from 3 $\mathrm{m\,s^{-1}}$ to 7 $\mathrm{m\,s^{-1}}$. During the three days with frontal passages shows the 23 December 2016 the highest mean absolute error of 6.5 $\mathrm{m\,s^{-1}}$, more than three times as high as the monthly averaged value from Müller et al. [2017]. Their study case in February 2015 showed a slight overestimation of ECMWF 10 m wind compared to the Norwegian AROME-MetCoOp domain, but still overestimates MEPS the

wind. What could be still a weakness that the model overestimates the wind speed? In Müller et al. [2017]: change from ECOCLIMAP1 because the surface roughness was too low and followed high wind speeds? Is this still the case for MEPS? High wind speeds followed also from wrongly adressed 'permanent snow'. Do not use 'orographi drag' in AROME-MetCoOp, could that lead to the too high estimated wind? When 'canopy drag' was changed saw increase in SBL drag which followed a decrease in wind speed. But AROME-MetCoOp is able to forecast high wind speeds, while ECMWF is not.
Haukeliseter is a measurement site exposed to high wind speeds [Wolff et al., 2013, 2015] the ensemble prediction system MEPS seems to still have issues forecasting the wind speed correctly in mountainous terrain. Figure 4.2.1 indicates that MEPS is able to estimate larger scale features which is probably related to the outer boundary conditions of ECMWF described by Dahlgren [2013]. In general, were surface parameters well predicted, only wind speed and precipitation accumulation showed overestimation in MEPS. Wind speeds forecasted higher than observations, is probably related to the weakness of wind speed prediction already known from the previous operational model AROME-MetCoOp. On the 25 December 2016 and 26 December 2016 MEPS also overestimated the precipitation amount at the surface, this will be further discussed in Section 4.3.

4.3 SURFACE SNOWFALL ACCUMULATION

One approach of this study is to see if observed surface accumulation was correctly predicted by the regional weather model MEPS. Precipitation amount at the surface are shown in Figure 4.3.1. The figures are representing the observed and forecasted surface precipitation accumulation in mm over 48 h. Accumulation, measured by the double fence are presented as red hexagons. Minutely retrieved surface snowfall amount in dash-dotted green. The ten 48 h forecast ensemble members are lines in black and grey, the deterministic and its perturbed ensemble members, respectively. The blue dashed line shows the ensemble mean of all ten members. Since the deterministic and the first ensemble member are having values every hour and the other perturbed members only every three hours, shows the ensemble mean the precipitation amount at 0 h, 3 h, ..., 21 h, 24 h, ..., 48 h forecast time. When too few ensemble members were present, like

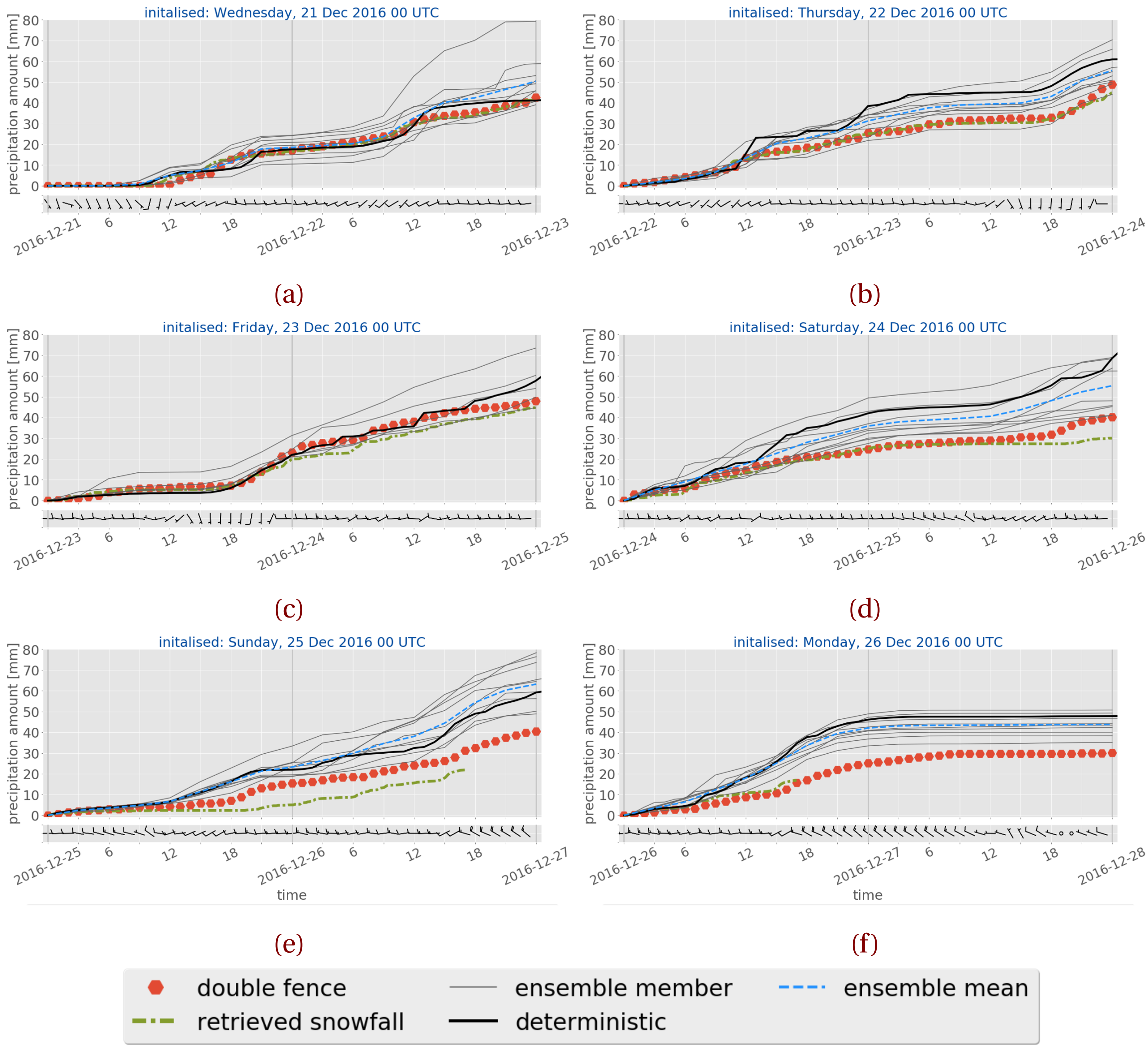

Figure 4.3.1: 48 h surface snowfall accumulation for 21 December 2016 to 26 December 2016 (a f). Representing the values from the double fence in red, hexagons; optimal estimation retrieval output at snow layer height 400 m in dash-dotted green; and ensemble member deterministic forecast, initialised at 0 UTC in black and its nine perturbed ensemble members in grey. The ensemble mean of all ten members is shown in dashed blue. Underneath are the associated last hour 10 min average wind from the weather mast at 10 m height.

on 23 December 2016, no ensemble mean is calculated (Figure 4.3.1c). Underneath is the associated 10 min average wind of the last hour from the 10 m weather mast at Haukeliseter, to see if surface accumulation observations may be influenced by wind.

Figures 4.3.1a to 4.3.1c show in general a better agreement between observations and forecast for 48 h forecasts initialised on 21 December 2016 to 23 December 2016 at 0 UTC. The spread of the ensemble members around the control run fit better to the observations as well than initialisations on 24 December 2016 to 26 December 2016. During these days intensifies the low-pressure system and gets closer advected to the Norwegian coast and influencing the local weather in Norway (Chapter 3). Figures 4.3.1d to 4.3.1f indicates a larger estimated surface precipitation amount for all ten ensemble members than observed at the measurement site between 24 December 2016 to 26 December 2016.

The correlation between double fence observation and ensemble forecast is presented in Figure 4.2.3a and b. Showing a better agreement between 21 December 2016 to 23 December 2016 than initialisation on 24 December 2016 to 26 December 2016. On 21 December 2016 to 23 December 2016 is the slope of the regression relatively close to unity, indicating a good agreement between the ensemble forecast and the observations by the double fence. The largest disagreement between surface observations and forecasts is seen on 25 December 2016 with a positive bias up to 17 mm (Figure C.2.1i). The mean absolute error is not larger than 13 mm for the first three days and increases with intensification of the storm up to 19 mm on 24 December 2016.
Initialisations on 24 December 2016 indicate an overestimation of the deterministic surface snowfall prediction already after 13 h forecast time. The deterministic forecast in solid black is much higher and increases faster than the observations. In Figure 4.3.1d at 16 UTC a higher value of approximately 15 mm can be seen when compared to the surface measurements. This difference remains almost constantly over the forecast time. Furthermore, all ensemble members seem to overestimate the surface accumulation after 24 h prediction time.
Since the MEPS performance was better on the previous days one might assume that the double fence measurement is influenced by surface winds. It shows in Figure 4.3.1d that the 10 min average wind at 13 UTC increases from 5 $\mathrm{m\,s^{-1}}$ to 10 $\mathrm{m\,s^{-1}}$ (see also Figure C.1.1n). Wolff [2018] states that the double fence gauge is influenced by wind, but accumulation measurement errors occur rather at higher wind speeds larger than 20 $\mathrm{m\,s^{-1}}$. It is therefore assumed that the measurements from the double fence are correct and MEPS had rather a forecasting issue.
While the cyclone gets more advected to Norway increases the forecast inaccuracy of

the surface precipitation. On 25 December 2016 the miscalculation of the precipitation amount is associated with the warm sector passage at Haukeliseter (Section 4.2). Afterwards follows the model the same path as the double fence observations, but higher. The 25 December 2016 indicates a good spread between the ensemble members and the deterministic forecast, while on 24 December 2016 the ensemble members were not spread symmetrically around the deterministic forecast.

An overestimation of the surface accumulation is also observed on 26 December 2016. While the large-scale analysis indicates the passage of an occlusion after 15 UTC (**??**, **??**) seems the overestimation to occur after 12 h forecast time in Figure 4.3.1f. Again, all ensemble members seem to follow the course of the double fence accumulation, but larger.

Whereas the spread between the ensemble members is large in the beginning of 24 December 2016 is the variability between the members narrow for 25 December 2016 and 26 December 2016. The variability between the ensemble member can be compared with a box-whisker plot. A box-whisker-plot shows the time evolution of the distribution of the precipitation amount made of ten ensemble members up to 48 h. Since some ensemble member do not have forecast values every hour provides the box-whisker-plot in Figure 4.3.2 information every 3 h. The red line shows the ensemble mean of all ten members and shows if the distribution is skewed. The short light green horizontal line is showing the median, wide vertical box represents the 25th and 75th percentiles, and minimum and maximum values are indicated by the vertical lines, whiskers.

The box-whisker-plot in Figure 4.3.2 shows the distribution of the ten ensemble members for the respective days. All three days with overestimation seem to be different in their variability. As expected increases the forecast uncertainty with longer forecast time for precipitation amount.

Figure 4.3.2b shows for 25 December 2016 the least variability between the ten ensemble members of up to almost 24 h. The 25 December 2016 is also the forecast with the smallest positive bias of these three days. As Figure 4.2.3j suggests is the overestimation not as high as for 24 December 2016 and 25 December 2016. On 24 December 2016 and 26 December 2016 is the mean error for the surface accumulation largest with values up to 19 mm.

Larger variability is already present after 3 h prediction time in Figure 4.3.2a on

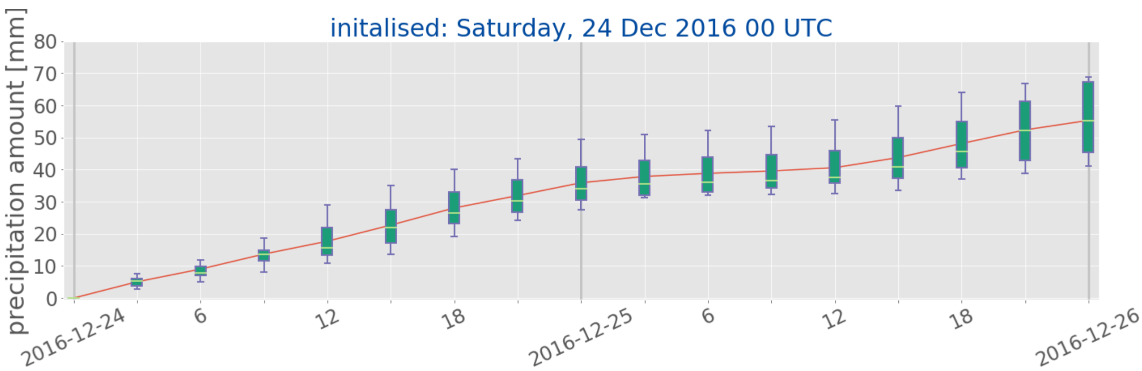

(a)

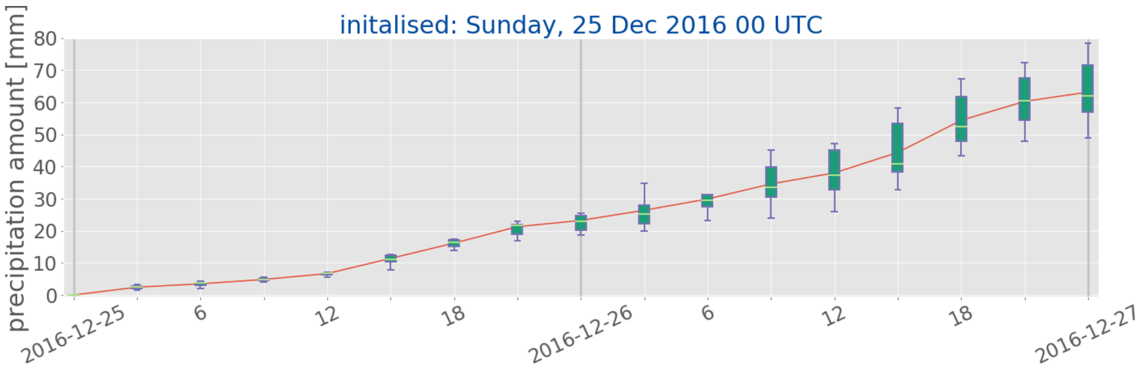

(b)

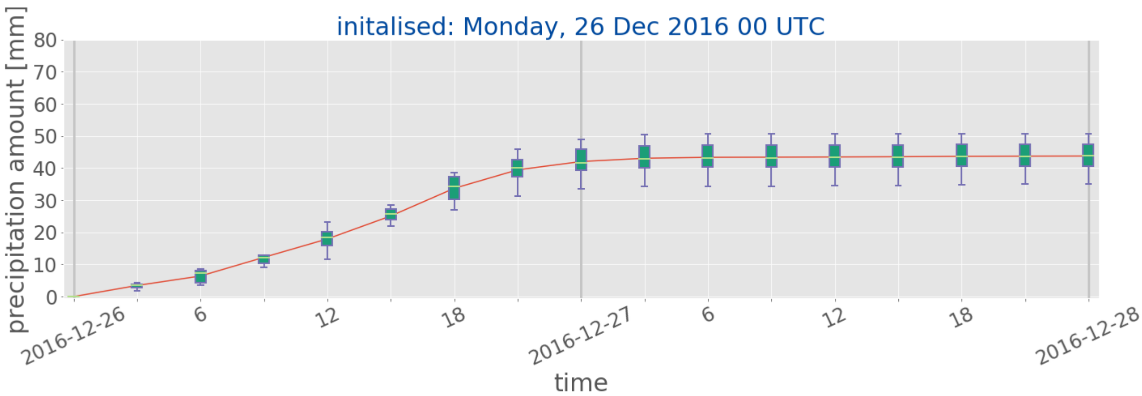

(c)

Figure 4.3.2: Box-whisker-plot of the ten ensemble members of MEPS. Red line indicating the ensemble mean, lower and upper whisker the 25th and 75th percentile, respectively. Light green shows the median of all members and the box represents the middle 50 % of scores of the precipitation.

24 December 2016. The spread between the ensemble members (shown by the minimum and maximum whiskers) seems to be wide indicating a larger uncertainty about the amount of surface accumulation. The ensemble mean (red line) is always higher than the median and already after 12 h forecast time is the median closer to the lower 25th percentile. Also, all upper whiskers in Figure 4.3.2a are taller than the lower ones, which would follow that the ensemble members vary amongst the most positive quartile and that it is very similar for the least positive quartile group. Since the deterministic forecast, black line in Figure 4.3.1d, is in the upper percentile compared to its perturbed members it follows that for this forecast the deterministic forecast was not the best guess for the surface accumulation and by using the 'wrong' initial state it can have led to larger miscalculations.

I believe that the uncertainty appearing already after 3 h could be associated with a too long spin-up time of MEPS. MEPS usually has a spin-up time of about three hours, on 24 December 2016 this might have been longer as a result of poorer initial conditions Need a reference here, not stated in Müller et al. [2017]. The regional model MEPS receives initial and boundary conditions from ECMWF before it can produce forecasts [Müller et al., 2017]. Since initial conditions such as observations have uncertainties as well as the model has mistrust, and the own climatology needs to be approached, a model has to stabilize before the simulations can be trusted. The spin-up time varies depending on the quality of the initial and boundary conditions. Apparently, it seems, that the initial and boundary conditions for MEPS were not perfect for initialisations on 24 December 2016 at 0 UTC. The deterministic and perturbed members seem not to have stabilised yet and show larger variability in **??** from early on.

The uncertainty might have also been related to the fact, that the large-scale situation got more complex. The precipitation amount associated with the passage of an occluded front on 23 December 2016 was higher than on the previous days (Figure 4.2.1i and **??**). On previous days was the hourly precipitation around 0 UTC less intense than on 23 December 2016. This led to a higher accumulation amount over shorter time and could have followed a larger variability in the forecast model. Another possibility is perhaps that MEPS might have accounted for additional precipitation around 12 UTC on 24 December 2016 and this showed a stronger increase in accretion in Figure 4.3.1d at 13 UTC. I believe it could be associated to a local resolution effect of MEPS. Figure 2.5.1 shows the MEPS resolution and its 2.5 km grid cells around the Haukeliseter site. The complex terrain represented in the model could have followed a local misplacement of a precipitation cell by a few kilometres and followed an estimation of more accumulation at the site after noon.

Figure 4.3.2b and c show a smaller ensemble member variability on 25 December 2016 and 26 December 2016 than on 24 December 2016. The box-whiskers are narrower for the first 30 h in Figure 4.3.2b, but slightly larger after 6 h forecast time for initialisations on 26 December 2016. Section 4.2 presented a good agreement between observations and forecast of large scale features in terms of pressure, temperature and wind direction. While the occlusion on 26 December 2016 was more intuitive (Figures 4.2.1k to 4.2.1n) than the warm front passage on 25 December 2016 (Figure 4.2.1b, d, f, h) shows the mean error for each variable to be best for 25 December 2016 (Figure C.2.1b,d,f, h, and j).
On 25 December 2016the overestimation started to occur around 13 UTC in Figure 4.3.1e, related to the delayed forecasted temperature increase in Figure 4.2.1d. As **??** shows, increases the variability in the forecast after 15 h prediction time. In general, agree median and mean well for the entire period of a 48 h forecast. After 39 h prediction time is the mean much higher than the median and closer to the lower 25th percentile in **??**. It seems, that all ten ensemble members agree well on the prediction and nevertheless overestimates MEPS the surface accumulation. I consider that MEPS misinterpreted the amount of precipitation related to the passage of the warm sector.
During 26 December 2016 the core of the low-pressure system goes through between 15 UTC and 18 UTC at Haukeliseter. The box-whiskers in Figure 4.3.2c indicates a larger variability after 6 h prediction while the precipitation amount forecast is miscalculated at 12 UTC and following the structure of the double fence observation. Variability of all ensemble members show to increase at 6 h forecast time, but then decreases again in Figure 4.3.2c.
Since the box-whisker-plot in Figure 4.3.2b and c show less variability in the beginning it is assumed that spin-up time issues are less likely. It could be related to an error in the initialisation state, even though it does not show in the variability in the beginning. An error associated with the spin-up time of MEPS is not totally excluded for these days. In Figure 4.3.1e and f agrees the ensemble mean well with the deterministic forecast, which is an indication of a symmetrical spread around the deterministic run.
The overestimation during 24 December 2016 and 26 December 2016 might be related

to the high forecasted wind speeds, as well as to the complex development of the low-pressure system north-west of Norway on 24 December 2016.

Table 4.3.1: Surface snowfall accumulation measured by the double fence gauge. Presenting 12 h accumulation before noon and after noon, as well as the total 24 h surface accretion.

Day	**Accumulation** [mm]		
	12 h (0 to 12 UTC)	12 h (12 to 23 UTC)	24 h
21 December 2016	0.7	16.4	17.1
22 December 2016	13.6	12.0	25.6
23 December 2016	6.3	17.0	23.3
24 December 2016	14.7	10.1	24.8
25 December 2016	4.3	11.1	15.4
26 December 2016	8.8	16.3	25.1

According to Müller et al. [2017] are strong precipitation events better predicted with AROME-MetCoOp than with ECMWF (European Centre for Medium-Range Weather Forecasts). In Section 2.2 it was described, that during 21 December 2016 to 27 December 2016 56.9 % of the total December 2016 accumulation were observed. Müller et al. [2017] states also, that an overestimation appears, where the precipitation event (12 h accumulation) is less than 10 mm this seems not to be true for all days but could be possible for 25 December 2016 and 26 December 2016 (observed accumulation in Table 4.3.1). In December 2014 was the 12 h precipitation mean absolute error in AROME-MetCoOp with 1.5 mm. For the Christmas storm is the mean absolute error not larger than 5 mm for the first 12 h accumulation on 24 December 2016 and 26 December 2016 (Figure C.2.1l). Therefore, the assumption follows that on 26 December 2016 the overestimation might be correlated to the <10 mm problem described by Müller et al. [2017]. The 12 h accumulation is presented in Table 4.3.1 for Haukeliseter and shows that 12 h accrection was less than 10 mm for 25 December 2016 and 26 December 2016. On 25 December 2016 the mean absolute error was 1.1 mm for the first 12 h accumulation and shows that this could be an influence but does not necessarily mean to be the case, since the overestimation started to occur after 11 h prediction time.

It will be interesting to re-run the ensemble prediction system again with all available observations to see, if this has an influence on the overestimation indicated in Figures 4.3.1d to 4.3.1f. ECMWF as boundary condition might not have reached its stabilised state itself when MEPS was initiated and could also have led to a misinterpretation of surface accumulation. A re-run with analysis data from ECMWF could possibly improve the original forecast find reference for this. Another approach could be to perturb the initial state (deterministic forecast) in other way, to see if different perturbations might lead to a better correlation between observation and forecast at the ground than presented in **??**. Also, the deterministic forecast (best guess) might have been chosen incorrectly and followed a miscalculation of surface accumulation, since the misinterpreted best guess was perturbed. It is very important to have correct measurements such as the double fence or MRR observations, to produce better initial condition for weather forecast models, so that initialisations can start at a realistic state.
Also, more study cases should be considered to get a better estimate about the performance of MEPS during extreme winter events. The mean absolute error for 12 h accumulation has shown a great variability, depending on the initialisation time and the intensification of the low-pressure system.

4.4 OBSERVATION OF LARGE SCALE WEATHER PHENOMENA IN THE VERTICAL

Frontal boundary passages were observed at the surface several times throughout the extreme storm in December 2016. MEPS is able to predict the large scale features and related surface changes for initialisation more than 24 h before (Section 4.2). In winter 2016 three additional instruments were installed to estimate the vertical snow water content at Haukeliseter. This unique approach gives the opportunity to compare the vertical forecasts of SWC to vertical solid precipitation observations. As far as the author knows is there no study on this particular topic about the verification of vertical ensemble member prediction models with observations.
Figure 4.4.1 shows the reflectivity from the MRR at Haukeliseter for 23 December 2016,

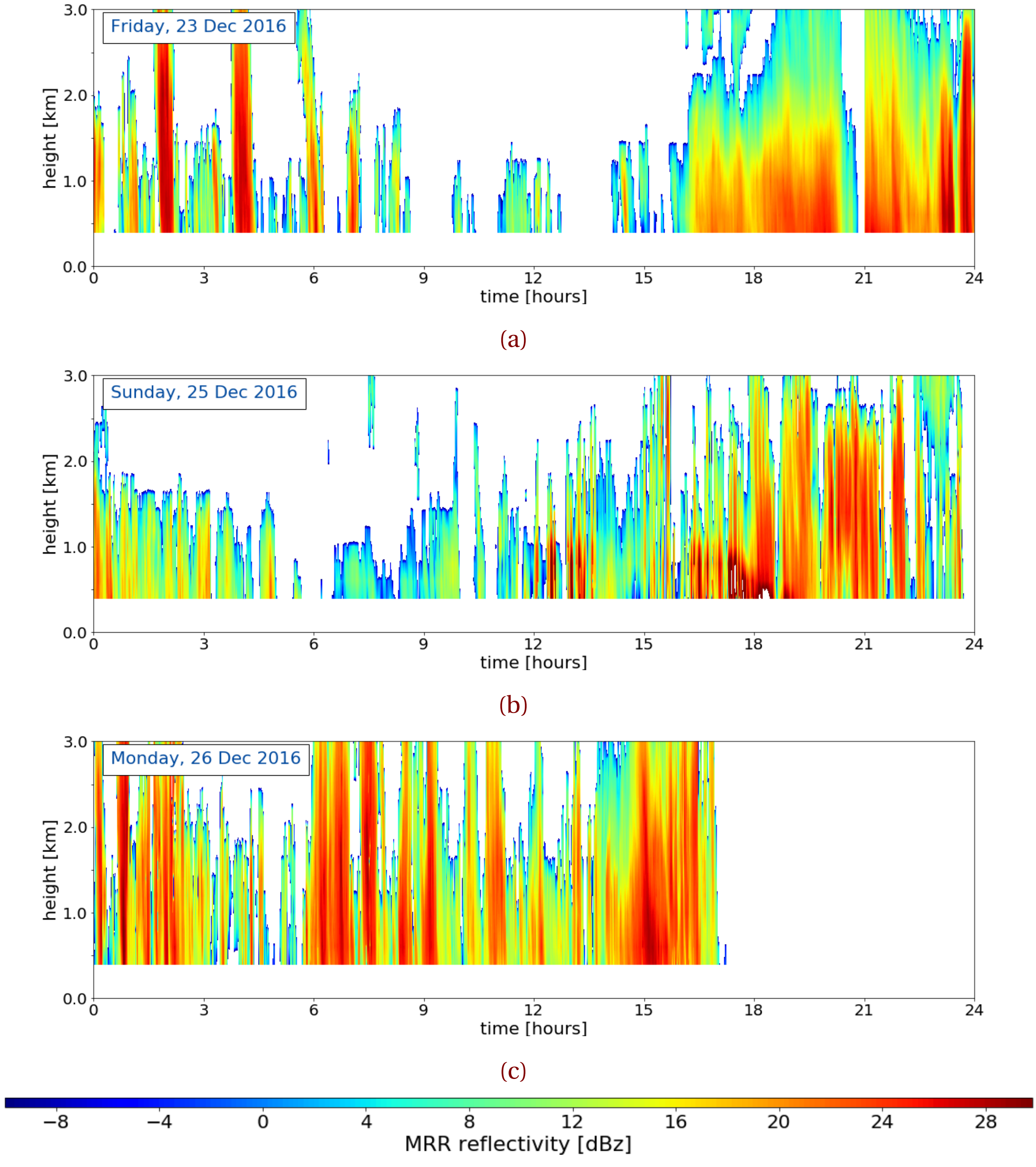

Figure 4.4.1: MRR reflectivity for the days when a front or an occlusion passed through at Haukeliseter. dBZ reflectivity according to the colour bar, with weaker precipitation in blue and more intense precipitation in red. a: Friday, 23 December 2016, b: Sunday, 25 December 2016, and c: Monday, 26 December 2016.

25 December 2016 and 26 December 2016. Passages of occluded fronts and a warm sector were observed on 23 December 2016, 26 December 2016 and 25 December 2016, respectively. Figure 4.4.1c presents only values until 17 UTC, because of the temperature change and hence a precipitation shift followed liquid drops freezing on the MRR dish and the signal got attenuated.
The transit of the boundary is shown in Figure 4.4.1 by the more consistent structure of a storm with higher reflectivity values. While on 23 December 2016 and 26 December 2016 the reflectivity did not pass values larger than 28 dBZ shows Figure 4.4.1b high reflectivity values larger than 30 dBZ (compare for approximation Table 2.3.1). These high values indicate the observation of possible liquid precipitation. Images from the MASC were able to verify observed liquid drops during 12 UTC to 21 UTC (Figure 4.2.2).
On 23 December 2016 allow the surface observations to assume that the occluded front passed through between 12 UTC to 21 UTC (Figure 4.2.1a, c, e). The vertical observations at Haukeliseter show intense reflectivity and therefore more intense precipitation after 16 UTC (Figure 4.4.1a). Another occlusion passed through on 26 December 2016 shortly before 15 UTC which lasted until 21 UTC indicated by a more consistent storm structure in Figure 4.4.1c around 15 UTC. The high reflectivity on both days shows the passage of the occlusion and the associated precipitation. The wind on 23 December 2016 was from the south, upslope (Figure 4.2.1e, Figure 2.1.1c) which led to a more consistent storm structure. On 25 December 2016 indicate Figure 4.2.1f and h strong wind observations from the west which led to a consistent, but shorter storm structure in Figure 4.4.1b at 15 UTC. The orographic influenced wind and therefore a possible relation to the precipitation will be further assessed in Section 4.5.

?? presents the reflectivity from the MRR and the snow water content retrieved from the reflectivity as well as the 48 h forecast values. Minutely MRR reflectivity and retrieved snow water content can be seen in Figure 4.4.2a, d, g, and j. Figure 4.4.2b, e, h, k show in the upper panel the hourly averaged values from the retrieved SWC and in the lower panel the ensemble mean of the instantaneous forecast values every hour over all ensemble member. Three hourly averaged retrieved values are then presented in the upper panel of Figure 4.4.2c, f, i, and l, the lower panel are the ensemble mean forecast values every three hours.
Figure 4.4.2e (lower panel) shows the one hourly averaged forecast values over all

ensemble members, neglecting not existing values. Initialisations less than 24 h before the event predict the consistent retrieved snowfall after 16 UTC (Figure 4.4.2d, lower panel and Figure 4.4.2e, upper panel). Even the three hourly averaged forecast values show a response on the occurrence of the storm (Figure 4.4.2f, lower panel). The duration of the passage is between 16 UTC to 23 UTC because of the longer time span is the prediction system able to estimate the snow water content. Forecasts initialised 48 h prior predict also the consistent storm structure and therefore the passage of the front (Figure 4.4.2b, c). In general, is the forecasted instantaneous snow water content amount weaker than the retrieved values for predications on 23 December 2016. Hourly averages, only using the deterministic forecast and the first ensemble member show no occurrence of the occlusion passage on either day (Figure C.3.1a, b, c, d). The variation of each ensemble member initialised on the respective day are given in Figure C.4.1. In Figure C.4.2a is the prediction for the occlusion passage quite weak.

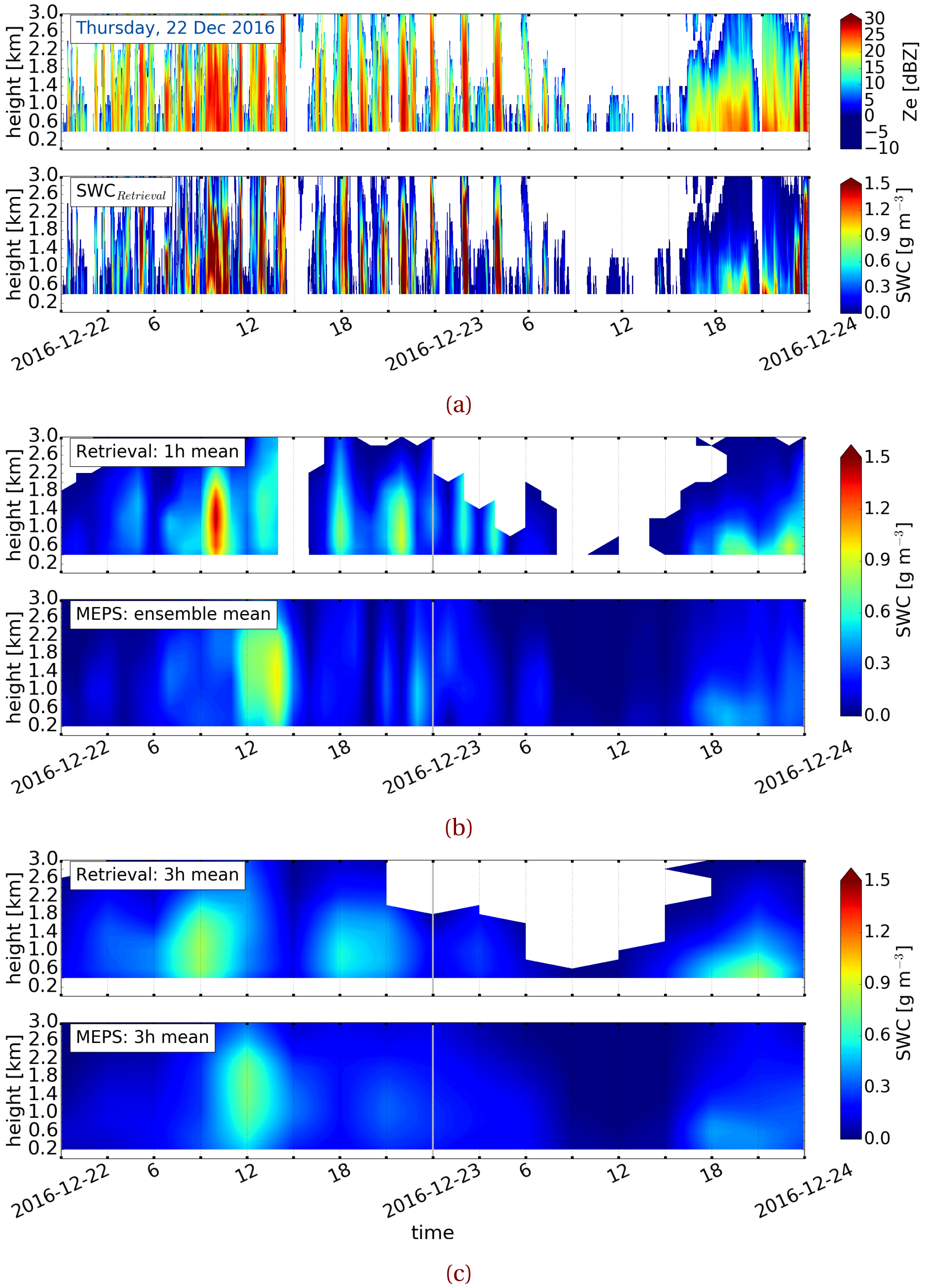

Figure 4.4.2: Initialisation 22 December 2016, 23 December 2016, 25 December 2016 and 26 December 2016 0 UTC. (a,d, g, j) Upper panel: MRR reflectivity for 48 h, lower panel minutely retrieved SWC. (b, e, h, k) Upper panel: hourly averaged retrieved SWC, lower panel instantaneous hourly averaged forecast of all ensemble member SWC, neglecting missing values. (c, f, i, l) Upper panel three hourly averaged retrieved SWC, lower panel instantaneous three hourly averaged forecast of all ensemble member SWC.

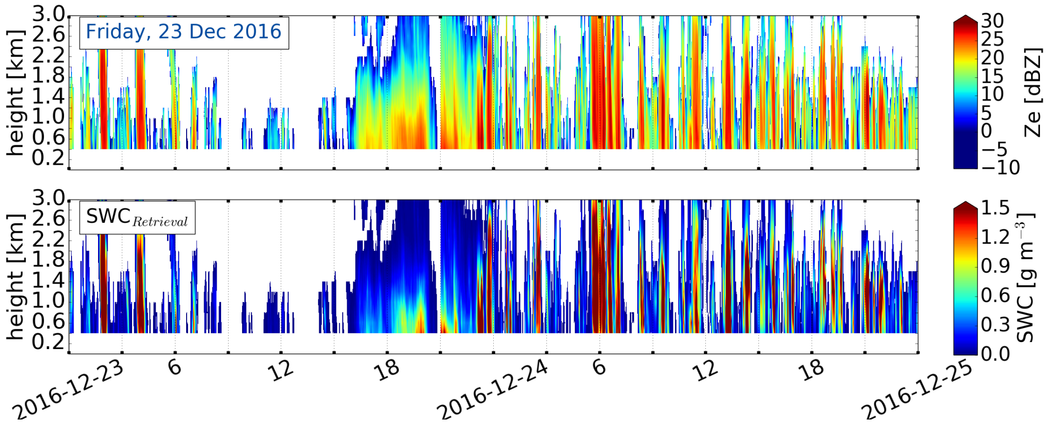

(d)

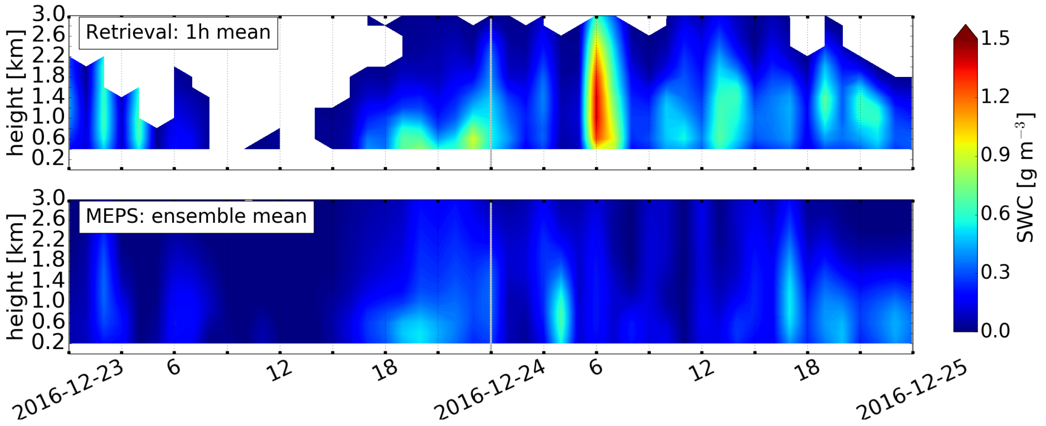

(e)

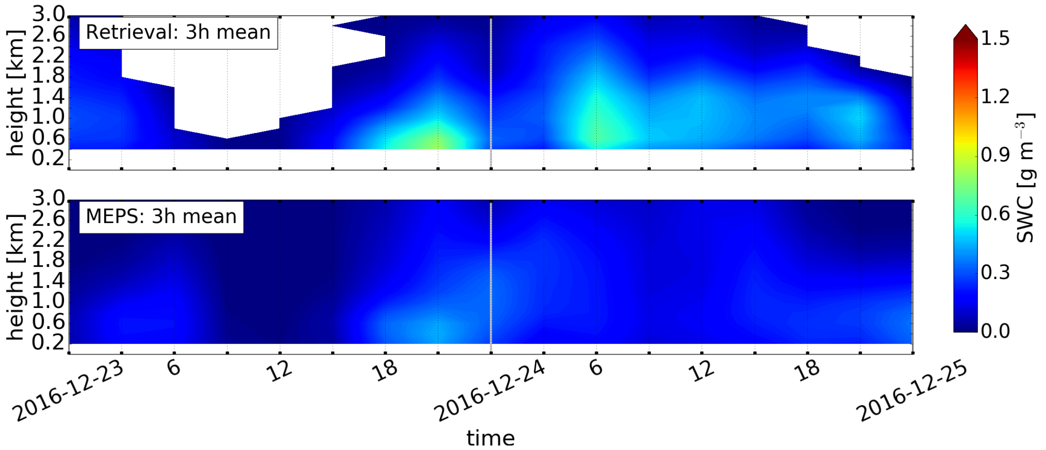

(f)

Figure 4.4.2: *(Continued from previous page.)* Initialisation 23 December 2016.

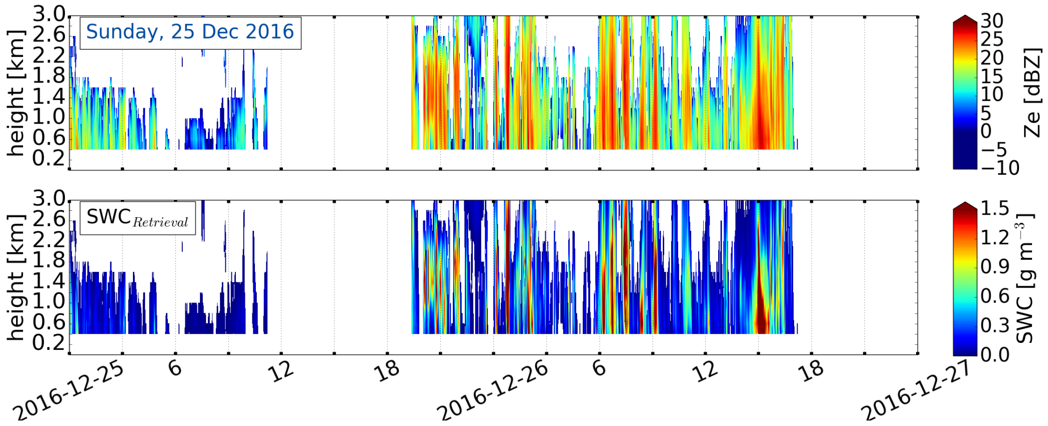

(g)

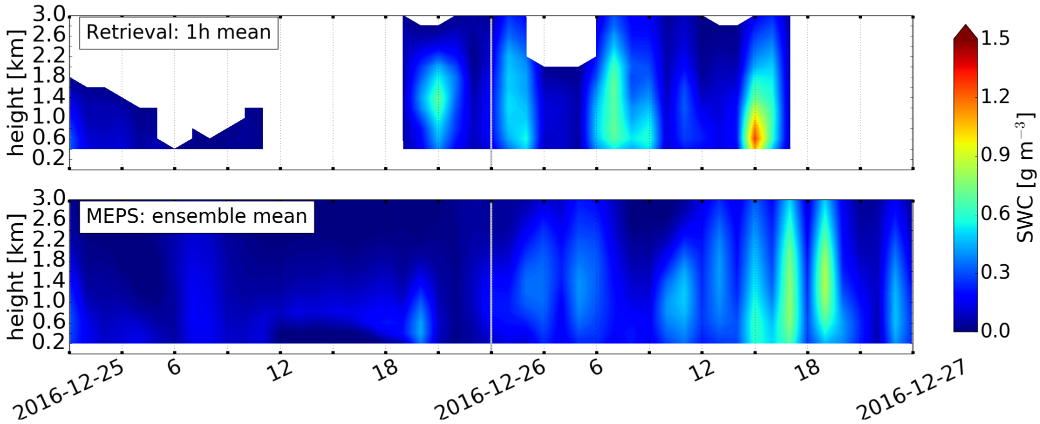

(h)

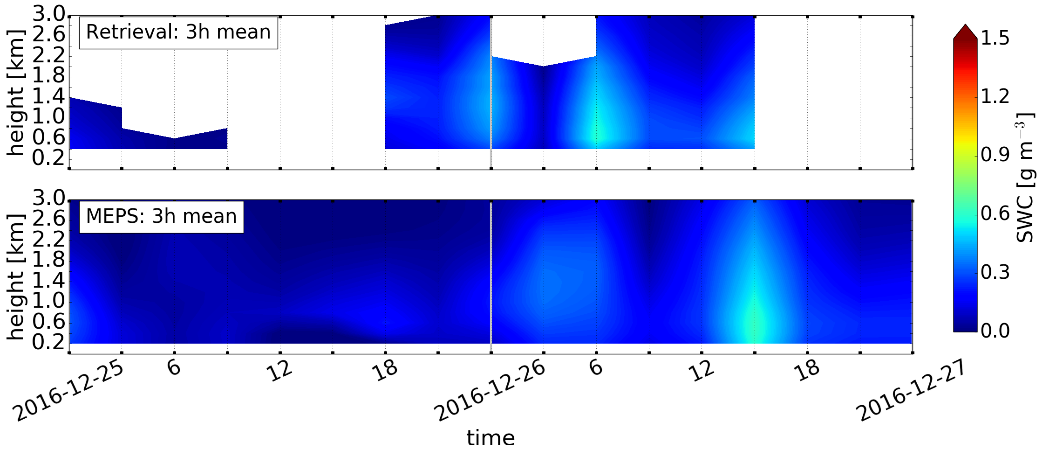

(i)

Figure 4.4.2: *(Continued from previous page.)* Initialisation 25 December 2016.

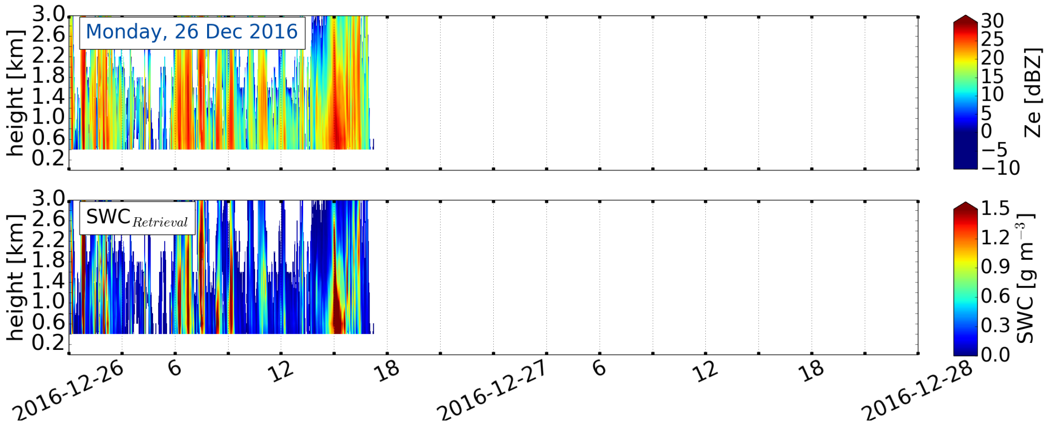

(j)

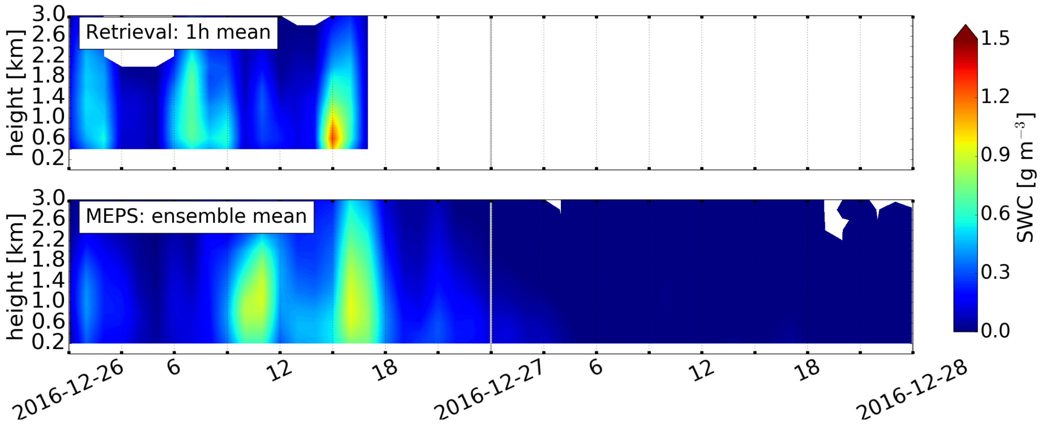

(k)

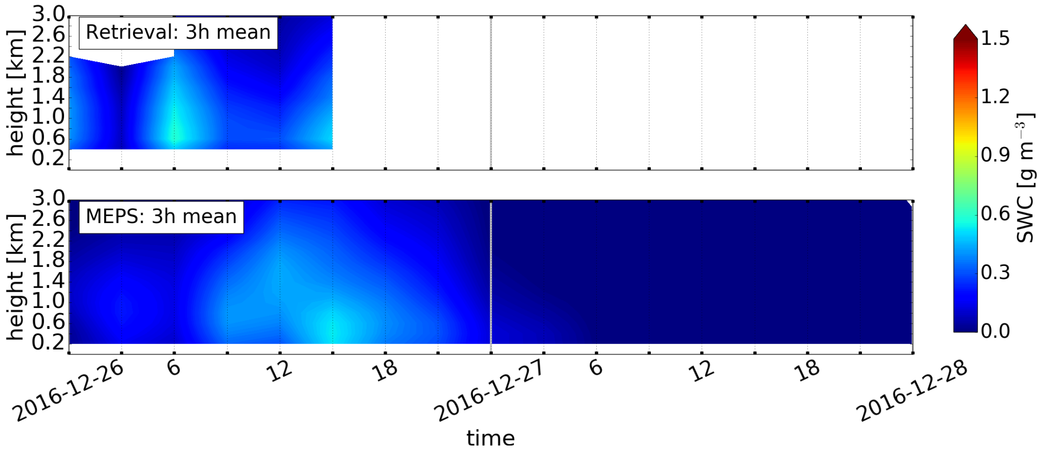

(l)

Figure 4.4.2: *(Continued from previous page.)* Initialisation 26 December 2016.

It shows also on 23 December 2016 the first perturbed ensemble member does not exist and hence little snow water content is predicted for the ensemble means. A comparison with 25 December 2016 and 26 December 2016 shows the same result. Not much more snow water content is predicted when using the instantaneous values from the deterministic and first perturbed forecast (Figure C.3.1c, d).

On 26 December 2016 when the passage of the occlusion is predicted, the three-hourly instantaneous SWC (Figure 4.4.2l) as well as the average of all ensemble members (Figure 4.4.2k) predict the frontal passage. Already initialisations 39 h prior let assume that intense precipitation over a short time will occur (Figure 4.4.2h, i). The variation of all members in Figure C.4.2c and d indicate that almost all perturbed members would have predicted the precipitation around 16 UTC, but the ensemble mean weakens the result. Higher predicted values appear for deterministic forecasts than for any other ensemble member for initialisations on 25 December 2016 and 26 December 2016. This bias might have led to an overestimation at the surface on 26 December 2016, where the deterministic forecast indicates higher values than the perturbed members (Figure 4.3.1f). But in Figure C.3.1c and d is the amount of snow water content very weak. It shows better estimations for predicted snowfall amount when using either hourly or three hourly time resolution and all ten ensemble members to create the mean than forecasts for hourly averages with only the deterministic and first perturbed member. Still the instantaneous average values of all ensemble members are much weaker than the retrieved SWC.

The 25 December 2016 showed patterns of liquid precipitation (Figure 4.2.2) with warm temperatures (Figure 4.2.1d) and high reflectivity (Figure 4.4.1b) between 12 UTC to 21 UTC. High reflectivity values in Figure 4.4.1b are present around 18 UTC with layer thickness up to 1.2 km. To see if liquid precipitation was predicted, the atmospheric cloud condensed water content and rainfall amount in model levels is summed. Figure 4.4.3a and b show liquid water content for initialisations at either 24 December 2016 or 25 December 2016. Positive surface temperatures were forecasted between 12 UTC to 21 UTC (Figure 4.2.1d). Initialisations more than 24 h prior show already the occurrence of the liquid layer. Figure 4.4.3a or b show also a narrow thickness up to 800 m. In Norwegian mountainous terrain is this an important feature since precipitation change can lead to a high risk for people. The avalanche danger increases with the precipitation change especially during high wind speeds. Since MEPS forecasts the liquid layer correctly in depth and length it seems to be a good interaction between the surface model and

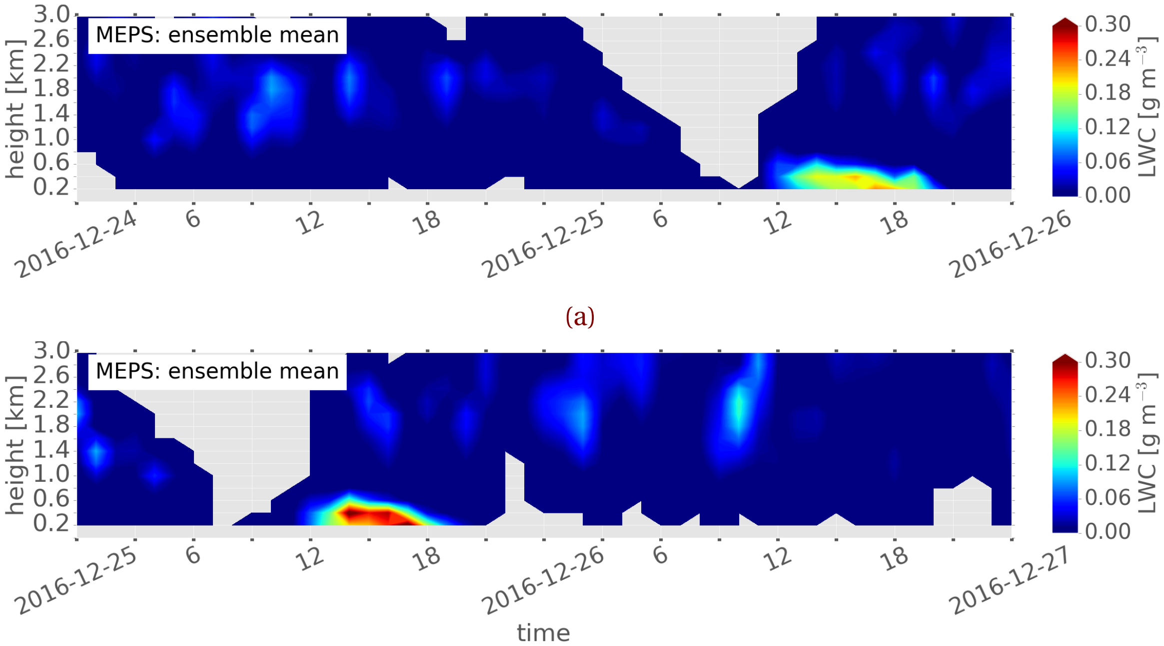

(a)

(b)

Figure 4.4.3: 200m hourly averaged LWC forecast from MEPS with all ensemble members, neglecting missing values. Initialised on 24 December 2016 and 25 December 2016 at 0 UTC. Liquid water content according to the colorbar.

the vertical prediction. This follows a high accuracy of the forecasting system and the advantage of using a high resolution convective scheme model.

For the first glance operates the forecast well when compared to vertical observations. One possibility is to assess the variability of all ensemble member with the coefficient of variation described in Section 2.6.4. Figures 4.4.4a to 4.4.4c show the coefficient of variation for SWC, which is the standard deviation of the ten ensemble members divided by the mean of all ensemble members. This coefficient gives the possibility to compare the SWC results for different days with different values. It follows for even a low ensemble spread of SWC (standard deviation of all ensemble members) then the different members do not need to be less variable.
The grey line in Figure 4.4.4 shows the ensemble mean of the hourly predicted SWC values. The darker the colour in Figure 4.4.4 the smaller is the variation of the SWC

Table 4.4.1: Interpretation of the coefficient of variation for SWC.

Size of CV [%]	**Interpretation** variability
0 to <25	negligible
25 to <50	low
50 to <75	moderate
75 to <100	high
100 to ∞	very high

relative to the mean. Initialisations on 23 December 2016 does not exist, because it had too few ensemble members (only six) to create a reasonable verification. Therefore, the initialsation on 22 December 2016 is used. The interpretation of the coefficient of variation for SWC is presented in Table 4.4.1. The CV agrees well with the prediction of the occlusion on 23 December 2016 after 15 UTC. The variability between the members is small and show a good agreement on the occurrence of snow precipitation. Figure C.4.2a and **??** show the same variability, where all ensemble member agree on the passage after 16 UTC. While comparing only six ensemble members in Figure C.4.2b, one could assume that the uncertainty of all ensemble members during the up-slope storm is low, but not as certain as for an initialisation on 22 December 2016 at 0 UTC.

A larger difference between the ensemble members is shown for the passage of the occlusion on 26 December 2016. Initialisations on 25 December 2016 present a lower variability for the passage after 15 UTC on 26 December 2016 than initialisations less than 24 h prior. Therefore, an increase of variability after shorter time and an increase in uncertainty. Again, this is not a fair comparison since hourly instantaneous values are used and there might be a time delay of half an hour about the passage which would follow it is not seen in the model forecast.

Another way to see how the MEPS forecast performed compared to the vertical observations can be done by correlating the observed SWP with the ensemble member snow water content.

One question to answer in this work is if the operational model MEPS gets large

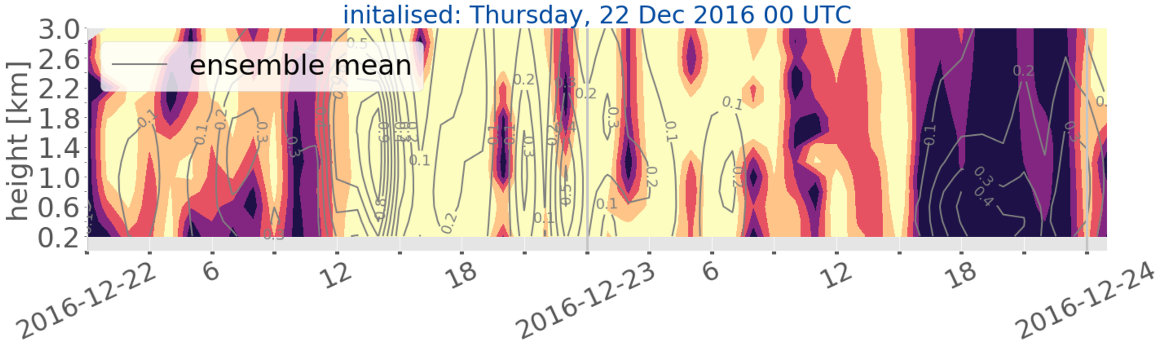

(a)

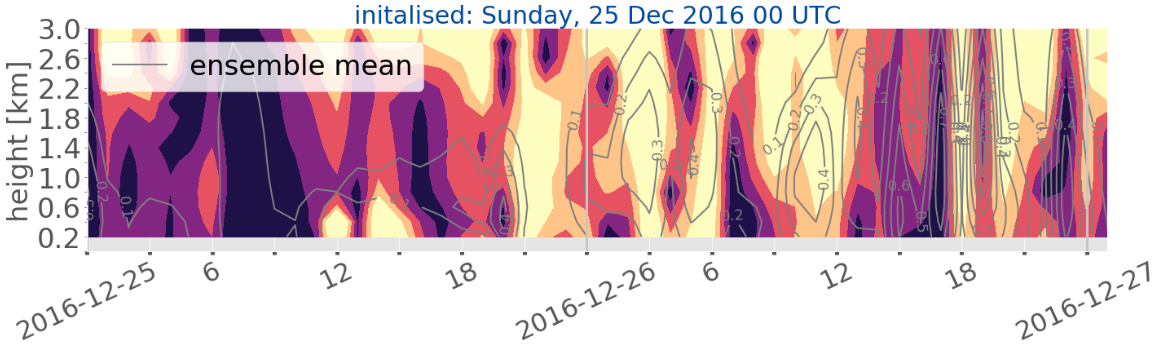

(b)

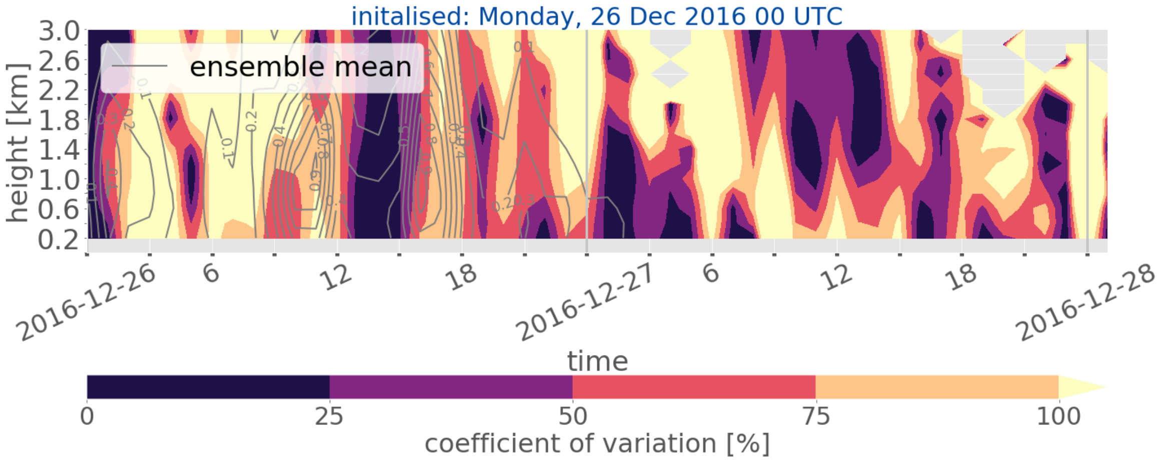

(c)

Figure 4.4.4: SWC variation of the ten ensemble members of MEPS. The lighter the colour according to the colourbar the higher the variation between the perturbed ensemble members. In grey the ensemble mean of all ten members.

scale features correctly. As discussed here and in Section 4.2 it seems that the model is able to cover the development of large scale features and its associated precipitation. Even with the intensification of the storm seems MEPS to be able to predict extreme events such as the Christmas event, but might have some issues predicting fast transitions of frontal boundaries.
MEPS is also able to distinguish between liquid and solid precipitation in layer thickness and duration for time resolution of one hour. This can be a major advantage since a change in temperature and associated precipitation transformation can lead to high safety issues in the Norwegian mountains, especially during winter. With the knowledge more than 24 h prior can risk notice be send out to the population and rescue teams can prepare in advance. Furthermore, roads and train tracks can be closed to increase the safety of people. I'm not sure if the above mentioned should be here?!

4.5 Orographic influence on precipitation

The Haukeliseter is suspended to high wind speeds during the winter. The previous results have shown, that wind plays an important role on the precipitation. The mountain plateau is surrounded by higher mountains to the west and more open to the south east [Wolff et al., 2013, 2015], this orography seems to influence the vertical precipitation pattern. The correlation between wind speed observations and forecast have shown an overestimation of predicted wind speed throughout the event (Figure 4.2.3g and h). Müller et al. [2017] already mentioned the weakness of too strong wind prediction in AROME-MetCoOp.
On 21 December 2016 and 23 December 2016 wind directions from the south-east and south were observed, respectively. As earlier discussed in Section 4.2 and **??** was the wind change associated with the occlusion passage on 23 December 2016. The wind direction on 21 December 2016 change was also related to the large scale synoptic flow but was not associated with a frontal passage. A comparison with the large scale weather analysis from ECMWF shows, that the large scale surface wind is from the south-west at 6 UTC on 21 December 2016 (**??**) and has changed to west at 12 UTC (**??**). The observations at the Haukeliseter site show between 6 UTC to 12 UTC wind from south-east, while the predicted wind direction is from south in Figure C.1.1e. The local wind direction

influenced the precipitation pattern in the vertical in the matter that a more consistent storm structure was observed and predicted between 9 UTC to 12 UTC (Figures 4.5.1a to 4.5.1c). Both days show a more consistent storm structure with not as intense snow water content than for storm patterns from the west. Figure 2.1.1c presents the local topography around Haukeliseter and Figure 2.5.1 shows the topography resolved by MEPS. It shows that MEPS is able to cover some of the complex structure around the site, with the higher mountain to the west and the valley to the south-east. The prediction model seems to forecast the wind direction overall well, only on 21 December 2016 before 10 UTC is a south instead of a south-east wind predicted. It displays that even if the large scale wind is from the south-west is the local wind rather from the south or south-east. The orography in Figure 2.1.1c lets assume that large scale south-west wind is forced along the valley laying in south-east direction. As Figure 4.5.1b indicates is the model obviously able to cover almost the exact timing of the up-slope storm pattern. The variability of each ensemble member is again presented in Figure C.4.1a. It shows that almost all ensemble member agree on the occurrence of the storm pattern during 9 UTC to 12 UTC.

Wind from the west and therefore over mountains followed always a pulsing with more intense precipitation in the vertical (Figure 4.4.2 and **??**). This effect might be related to wave breaking at the mountain and result into a pulsing precipitation pattern. More precipitation events need to be studied to understand this effect around the Haukeliseter site. MEPS seems not to cover all pulses during the course of a day, which is related to the time resolution of the forecast values. Since the prediction values exist only every hour the model might miss some of the high pulses 30 min before or after the occurrence.

One outcome of the presented study is that MEPS is able to resolve the local topography and predicts the wind direction in almost all the cases correctly. It did not cover the south-east wind direction on 21 December 2016, which must be related to the local topography. It seems more intuitive for the model to force large scale south-westerly flow into south direction. As seen in Figure 2.5.1 must the wind go along the 7.2° longitude, since a higher elevation is to the west and a 1350 m high mountain to the east. This true prediction of wind direction leads then to the correct estimation of vertical precipitation patterns. Section 4.3 describes the overestimation of surface snow accumulation during the intensification of the extreme storm. MEPS forecasted more ground accumulation than it was observed. One approach was to see, if the wind might have had an influence on the surface measurement of the double fence, which did not show to be true. A

comparison of the hourly values of MEPS, shows that neither on 24 December 2016 nor on 25 December 2016 or 26 December 2016 the vertical snow amount was higher than the observations (Figure 4.5.1e, 4.4.2h, and k). Figure C.4.1 shows very intense individual ensemble members, but no prominent sign of overestimation when the surface miscalculation was present.
During 24 December 2016 to 26 December 2016 was the wind constantly from the west with higher wind speeds observed than during 21 December 2016 to 23 December 2016 (Figure 4.2.1e, f, m; Figure C.1.1e, f, m; Figure 4.2.1g, h, n, and Figure C.1.1g, h, n). Figure 4.2.3e and f indicate a better agreement between the forecasted and observed wind directions when precipitation overestimation occurred. During 24 December 2016 to 26 December 2016 were the observed wind speeds higher than on the previous days, and as Figure 4.2.3g and h present is the correlation between observation and forecasts lower during high wind speeds. The high wind speeds from the west followed a pulsing storm pattern with intense and less intense precipitation. The pulsing pattern is forecasted by MEPS for initialisations longer than 24 h prior. Since the model gets the wind direction correctly and the affect of local mountains it follows that there seems to be some kind of interaction issue between the vertical snow amount and the surface accumulation. Vertical instantaneous values every hour can lead to a misinterpretation of the here presented results. The ensemble variability in Figure 4.5.2a, Figure 4.4.4b, and c show that the ensemble members are divided about the existence of the exact pulsing.

While the wind direction of MEPS has a good agreement shows the wind speed larger values over all days. Although MEPS includes ten perturbed ensemble members the insufficiency of AROME-MetCoOp too high wind prediction in extreme situations is not resolved. The regional model wind prediction is still dependent on the intensity of the storm. As Müller et al. [2017] also mentioned are higher wind speeds in general better forecasted in AROME-MetCoOp than in ECMWF.

4.6 DISCUSSION ALL

This section needs another title! Just collecting up-coming disscussion points Of course, more storms should be investigated to find the exact correlation between the surface observations and the estimated accumulation to see if the deviation keeps as small for different snow patterns at Haukeliseter.

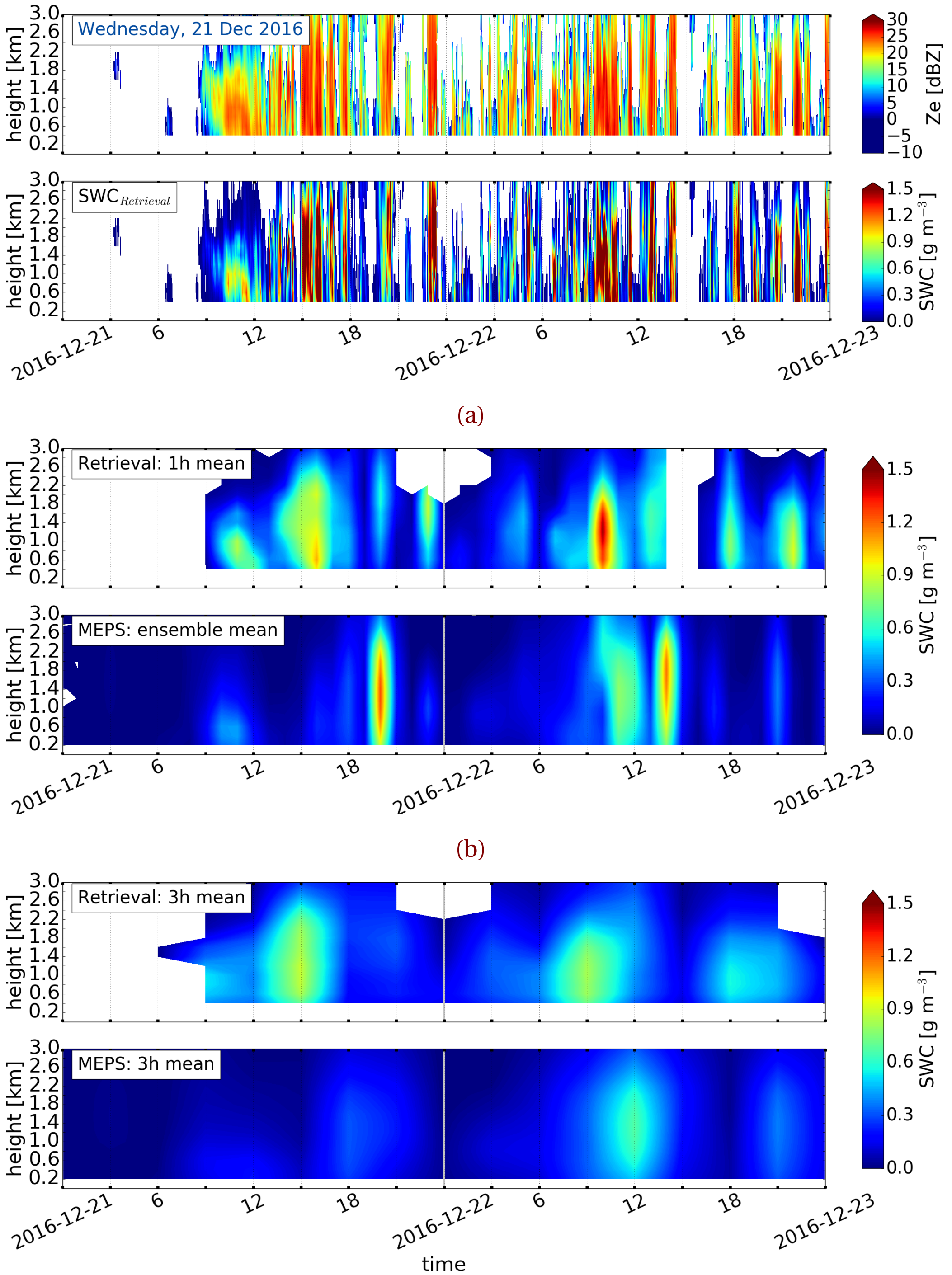

(a) (b) (c)

Figure 4.5.1: Initialisation 21 December 2016 0 UTC. (a,d) Upper panel: MRR reflectivity for 48 h, lower panel minutely retrieved SWC. (b, e) Upper panel: hourly averaged retrieved SWC, lower panel instantaneous hourly averaged forecast of all ensemble member SWC, neglecting missing values. (c, f) Upper panel three hourly averaged retrieved SWC, lower panel instantaneous three hourly averaged forecast of all ensemble member SWC.

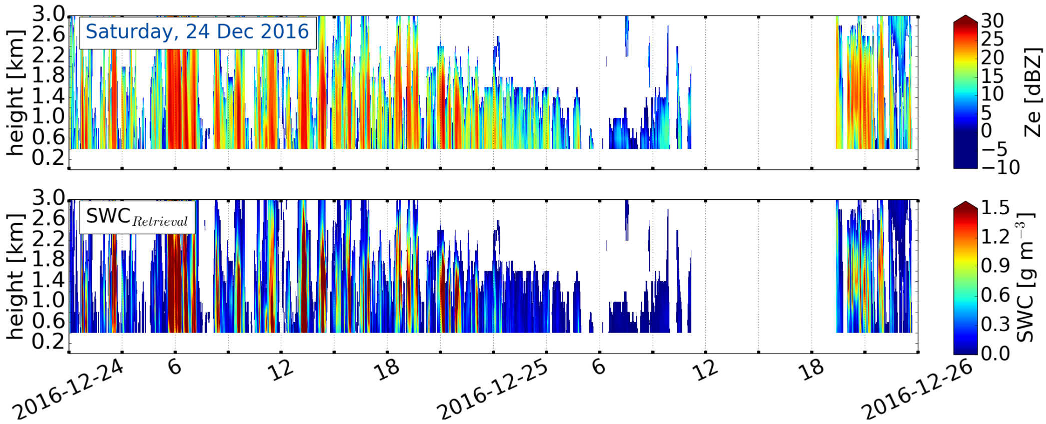

(d)

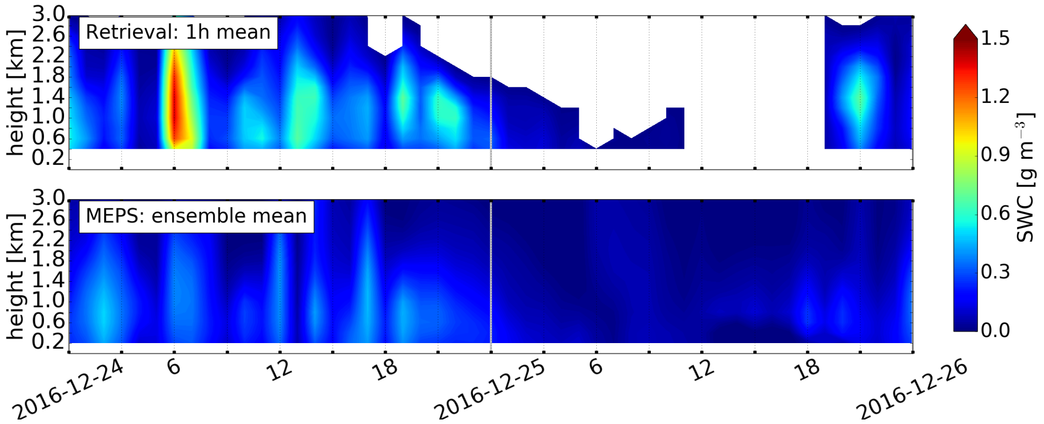

(e)

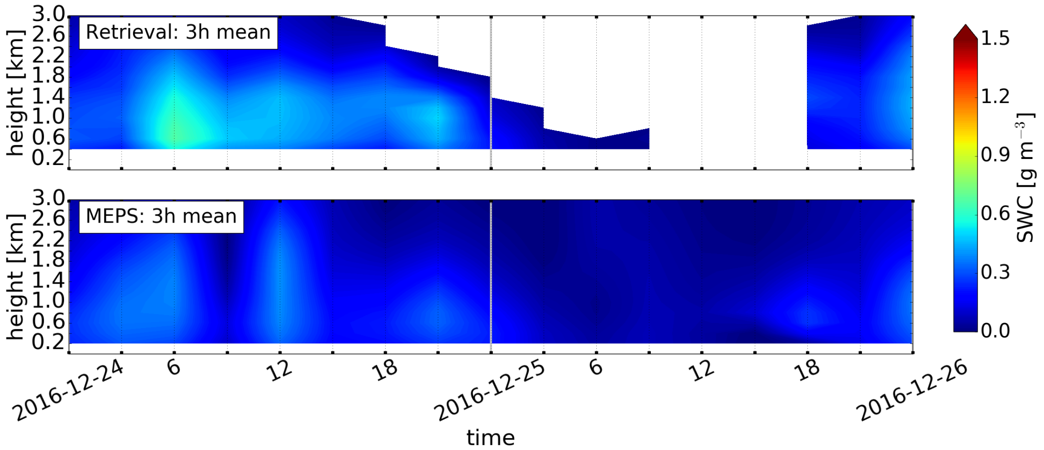

(f)

Figure 4.5.1: *(Continued from previous page.)* Initialisation 26 December 2016.

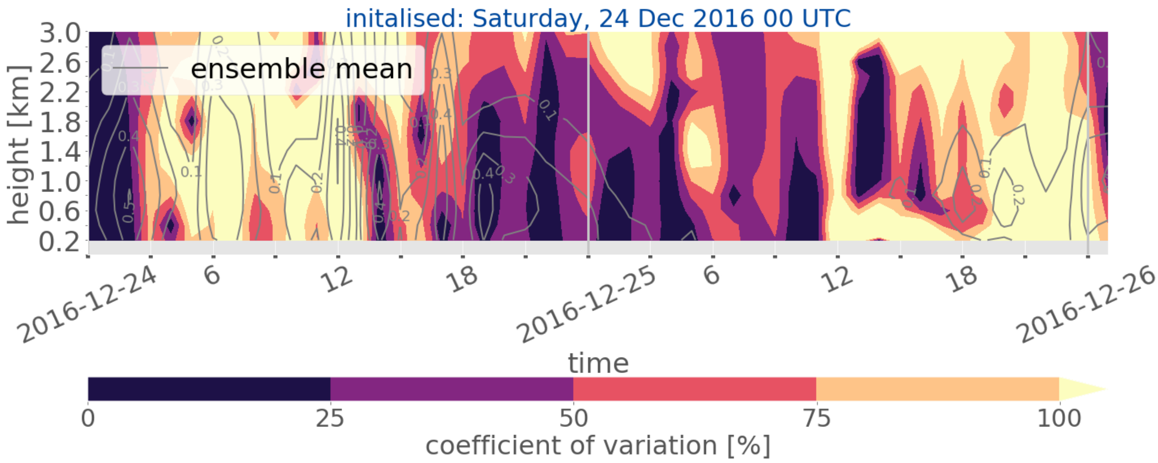

(a)

Figure 4.5.2: SWC variation of the ten ensemble members of MEPS. The lighter the colour according to the colourbar the higher the variation between the perturbed ensemble members. In grey the ensemble mean of all ten members.

Chapter 5: Summary and Conclusion

SUMMARIZE! What did you do? Why did you do it? What did you use? What were your findings? What could be done in the future?

References

Barnett, T. P., Adam, J. C., and Lettenmaier, D. P. Potential impacts of a warming climate on water availability in snow-dominated regions. *Nature*, 438(7066):303–309, November 2005. ISSN 1476-4687. doi: 10.1038/nature04141. URL https://www.nature.com/articles/nature04141.

Caniaux, G., Redelsperger, J.-L., and Lafore, J.-P. A Numerical Study of the Stratiform Region of a Fast-Moving Squall Line. Part I: General Description and Water and Heat Budgets. *J. Atmos. Sci.*, 51(14):2046–2074, July 1994. ISSN 0022-4928. doi: 10.1175/1520-0469(1994)051<2046:ANSOTS>2.0.CO;2. URL https://journals.ametsoc.org/doi/abs/10.1175/1520-0469(1994)051%3C2046:ANSOTS%3E2.0.CO;2.

Colle, B. A., Garvert, M. F., Wolfe, J. B., Mass, C. F., and Woods, C. P. The 13–14 December 2001 IMPROVE-2 Event. Part III: Simulated Microphysical Budgets and Sensitivity Studies. *J. Atmos. Sci.*, 62(10):3535–3558, October 2005. ISSN 0022-4928. doi: 10.1175/JAS3552.1. URL https://journals.ametsoc.org/doi/abs/10.1175/JAS3552.1.

Cooper, S. J., Wood, N. B., and L'Ecuyer, T. S. A variational technique to estimate snowfall rate from coincident radar, snowflake, and fall-speed observations. *Atmos. Meas. Tech.*, 10(7):2557–2571, July 2017. ISSN 1867-8548. doi: 10.5194/amt-10-2557-2017. URL https://www.atmos-meas-tech.net/10/2557/2017/.

Dahlgren, P. A Comparison Of Two Large Scale Blending Methods. page 16, 2013. URL http://metcoop.org/memo/2013/02-2013-METCOOP-MEMO.PDF.

Dando, P. Introducing the octahedral reduced Gaussian grid, June 2016. URL https://software.ecmwf.int/wiki/display/FCST/Gaussian+grids.

Doviak, R. J. and Zrnic, D. S. *Doppler Radar and Weather Observations*. Courier Corporation, 1993. ISBN 978-0-486-45060-5. Google-Books-ID: ispLkPX9n2UC.

eklima. Norwegian Meteorological Institute, 2016. URL http://sharki.oslo.dnmi.no/portal/page?_pageid=73,39035,73_39049&_dad=portal&_schema=PORTAL.

Farestveit, E. 80.000 mista radioen under ekstremvêret, December 2016. URL https://www.nrk.no/hordaland/80.000-mista-radioen-under-ekstremveret-1.13294980.

Field, C. B., Barros, V. R., Dokken, D. J., Mach, K. J., Mastrandrea, M. D., Bilir, T. E., Chatterjee, M., Ebi, K. L., Estrada, Y. O., Genova, R. C., Girma, B., Kissel, E. S., Levy, A. N., MacCracken, S., Mastrandrea, P. R., and White, L. L. Summary for policymakers. In: Climate Change 2014: Impacts, Adaptation, and Vulnerability. Part A: Global and Sectoral Aspects. Contribution of Working Group II to the Fifth Assessment Report of the Intergovernmental Panel on Climate Change. *Cambridge: Cambridge University Press*, page 34, 2014.

Færaas, A., Rommetveit, A., Duesund, J., and Senel, E. «Urd» har nådd orkan styrke – flytter seg mot Østlandet, December 2016. URL http://www.yr.no/artikkel/_urd_-har-nadd-orkan-styrke-_-flytter-seg-mot-ostlandet-1.13292245.

Garrett, T. J., Fallgatter, C., Shkurko, K., and Howlett, D. Fall speed measurement and high-resolution multi-angle photography of hydrometeors in free fall. *Atmos. Meas. Tech.*, 5(11):2625–2633, November 2012. ISSN 1867-8548. doi: 10.5194/amt-5-2625-2012. URL https://www.atmos-meas-tech.net/5/2625/2012/.

Garvert, M. F., Woods, C. P., Colle, B. A., Mass, C. F., Hobbs, P. V., Stoelinga, M. T., and Wolfe, J. B. The 13–14 December 2001 IMPROVE-2 Event. Part II: Comparisons of MM5 Model Simulations of Clouds and Precipitation with Observations. *J. Atmos. Sci.*, 62(10):3520–3534, October 2005. ISSN 0022-4928. doi: 10.1175/JAS3551.1. URL https://journals.ametsoc.org/doi/10.1175/JAS3551.1.

Geonor Inc. T-200b All Weather Precipitation – Rain Gauge, 2015. URL http://geonor.com/live/products/weather-instruments/t-200b-weather-precipitation-rain-gauge/.

Geonorge. DTM 10 Terrengmodell (UTM33) - Kartverket - Kartkatalogen, May 2018. URL https://kartkatalog.geonorge.no/metadata/uuid/dddbb667-1303-4ac5-8640-7ec04c0e3918.

Goodison, B. E., Louie, P. Y. T., and Yang, D. WMO Solid Precipitation Measurement Intercomparison: Final Report. Instruments and Observing Methods Rep. 67, WMO/TD-No. 872,. *World Meteorological Organization, Geneva, Switzerland*, page 318, 1998.

Gowan, T. M., Steenburgh, W. J., and Schwartz, C. S. Validation of Mountain Precipitation Forecasts from the Convection-Permitting NCAR Ensemble and Operational Forecast Systems over the Western United States. *Wea. Forecasting*, 33(3):739–765, June 2018. ISSN 0882-8156, 1520-0434. doi: 10.1175/WAF-D-17-0144.1. URL http://journals.ametsoc.org/doi/10.1175/WAF-D-17-0144.1.

Gunn, K. L. S. and East, T. W. R. The microwave properties of precipitation particles. *Q. J. Royal Meteorol. Soc.*, 80(346):522–545, 1954.

Hansen, B. B., Isaksen, K., Benestad, R. E., Kohler, J., Pedersen, Ø. Ø., Loe, L. E., Coulson, S. J., Larsen, J. O., and Varpe, Ø. Warmer and wetter winters: characteristics and implications of an extreme weather event in the High Arctic. *Environ. Res. Lett.*, 9 (11):114021, 2014. ISSN 1748-9326. doi: 10.1088/1748-9326/9/11/114021. URL http://stacks.iop.org/1748-9326/9/i=11/a=114021.

Hansen, B. B., Aanes, R., Herfindal, I., Kohler, J., and Sæther, B.-E. Climate, icing, and wild arctic reindeer: past relationships and future prospects. *Ecology*, 92(10):1917–1923, October 2011. ISSN 1939-9170. doi: 10.1890/11-0095.1. URL https://esajournals.onlinelibrary.wiley.com/doi/abs/10.1890/11-0095.1.

Homleid, M. and Tveter, F. T. Verification of operational weather prediction models september to november 2015. *METInfo Rep*, 16:2016, 2016. URL https://www.met.no/publikasjoner/met-info/met-info-2016/_/attachment/download/b0463915-cba0-42ac-8539-4233ae2bf01c:3d71565a27f88085373199a33ab8569151c144e9/MET-info-22-2016.pdf.

Hoskins, B. J., McIntyre, M. E., and Robertson, A. W. On the use and significance of isentropic potential vorticity maps. *Q. J. Royal Meteorol. Soc.*, 111(470):877–946, October

1985. ISSN 1477-870X. doi: 10.1002/qj.49711147002. URL http://onlinelibrary.wiley.com/doi/10.1002/qj.49711147002/abstract.

Hudak, D., Barker, H., Rodriguez, P., and Donovan, D. The Canadian CloudSat Validation Project. *4th ERAD*, September 2006. URL http://www.crahi.upc.edu/ERAD2006/proceedingsMask/00165.pdf. Barcelona, Spain.

Joos, H. and Wernli, H. Influence of microphysical processes on the potential vorticity development in a warm conveyor belt: a case-study with the limited-area model COSMO. *Q. J. Royal Meteorol. Soc.*, 138(663):407–418, January 2012. ISSN 00359009. doi: 10.1002/qj.934. URL http://doi.wiley.com/10.1002/qj.934.

Kochendorfer, J., Nitu, R., Wolff, M., Mekis, E., Rasmussen, R., Baker, B., Earle, M. E., Reverdin, A., Wong, K., Smith, C. D., Yang, D., Roulet, Y.-A., Buisan, S., Laine, T., Lee, G., Aceituno, J. L. C., Alastrué, J., Isaksen, K., Meyers, T., Brækkan, R., Landolt, S., Jachcik, A., and Poikonen, A. Analysis of single-Alter-shielded and unshielded measurements of mixed and solid precipitation from WMO-SPICE. *Hydrol. Earth Syst. Sci.*, 21(7): 3525–3542, July 2017. ISSN 1607-7938. doi: 10.5194/hess-21-3525-2017. URL https://www.hydrol-earth-syst-sci.net/21/3525/2017/.

Kulie, M. S. and Bennartz, R. Utilizing Spaceborne Radars to Retrieve Dry Snowfall. *J. Appl. Meteor. Climatol.*, 48(12):2564–2580, January 2009. ISSN 1558-8424. doi: 10.1175/2009JAMC2193.1. URL http://journals.ametsoc.org/doi/abs/10.1175/2009JAMC2193.1.

Køltzow, M. A. MetCoOp EPS - A convection permitting ensemble prediction system, October 2017.

L'Ecuyer, T. S. AOS 441 - Satellite and Radar Meteorology. January 2017. URL https://lecuyer.aos.wisc.edu/aos441.

L'Ecuyer, T. S. and Stephens, G. L. An Estimation-Based Precipitation Retrieval Algorithm for Attenuating Radars. *J. Appl. Meteor.*, 41(3):272–285, January 2002. ISSN 0894-8763. doi: 10.1175/1520-0450(2002)041<0272:AEBPRA>2.0.CO;2. URL http://journals.ametsoc.org/doi/abs/10.1175/1520-0450(2002)041%3C0272:AEBPRA%3E2.0.CO%3B2.

Liu G. Deriving snow cloud characteristics from CloudSat observations. *J. Geophys. Res. Atmos.*, 113(D8), September 2008. ISSN 0148-0227. doi: 10.1029/2007JD009766. URL https://agupubs.onlinelibrary.wiley.com/doi/abs/10.1029/2007JD009766.

Lorenz, E. N. Atmospheric Predictability as Revealed by Naturally Occurring Analogues. *J. Atmos. Sci.*, 26(4):636–646, July 1969. ISSN 0022-4928. doi: 10.1175/1520-0469(1969)26<636:APARBN>2.0.CO;2. URL https://journals.ametsoc.org/doi/abs/10.1175/1520-0469%281969%2926%3C636%3AAPARBN%3E2.0.CO%3B2.

Markowski, P. and Richardson, Y. *Mesoscale Meteorology in Midlatitudes*. John Wiley & Sons, September 2011. ISBN 978-1-119-96667-8. Google-Books-ID: MDeYosfLLEYC.

Martin, J. E. *Mid-Latitude Atmospheric Dynamics: A First Course*. Wiley, May 2006. ISBN 978-0-470-86466-1.

McCumber, M., Tao, W.-K., Simpson, J., Penc, R., and Soong, S.-T. Comparison of Ice-Phase Microphysical Parameterization Schemes Using Numerical Simulations of Tropical Convection. *J. Appl. Meteor.*, 30(7):985–1004, July 1991. ISSN 0894-8763. doi: 10.1175/1520-0450-30.7.985. URL https://journals.ametsoc.org/doi/abs/10.1175/1520-0450-30.7.985.

Meehl, G. A., Karl, T., Easterling, D. R., Changnon, S., Pielke, R., Changnon, D., Evans, J., Groisman, P. Y., Knutson, T. R., Kunkel, K. E., Mearns, L. O., Parmesan, C., Pulwarty, R., Root, T., Sylves, R. T., Whetton, P., and Zwiers, F. An Introduction to Trends in Extreme Weather and Climate Events: Observations, Socioeconomic Impacts, Terrestrial Ecological Impacts, and Model Projections. *Bull. Amer. Meteor. Soc.*, 81(3):413–416, March 2000. ISSN 0003-0007. doi: 10.1175/1520-0477(2000)081<0413:AITTIE>2.3.CO;2. URL https://journals.ametsoc.org/doi/abs/10.1175/1520-0477(2000)081%3C0413:AITTIE%3E2.3.CO;2.

MetCoOp Wiki. Description of MEPS, December 2017. URL https://metcoop.smhi.se/dokuwiki/nwp/metcoop/.

METEK, M. M. G. Micro Rain Radar MRR-2, October 2010. URL http://metek.de/wp-content/uploads/2014/05/Metek-Micro-Rain-Radar-MRR-2-Datasheet.pdf.

Meteo France. The Meso-NH Atmospheric Simulation System: Scientific Documentation, Part III: Physics, January 2009.

Meteorologene. "Her kommer #Urd! Selve Lavtrykksenteret treffer Møre og Romsdal, men den sterkeste vinden kommer sør for Stad. #SørNorge" 26 December 2016, 9:34am, 2016. URL https://twitter.com/Meteorologene.

Müller, M., Homleid, M., Ivarsson, K.-I., Køltzow, M. A. Ø., Lindskog, M., Midtbø, K. H., Andrae, U., Aspelien, T., Berggren, L., Bjørge, D., Dahlgren, P., Kristiansen, J., Randriamampianina, R., Ridal, M., and Vignes, O. AROME-MetCoOp: A Nordic Convective-Scale Operational Weather Prediction Model. *Wea. Forecasting*, 32 (2):609–627, January 2017. ISSN 0882-8156. doi: 10.1175/WAF-D-16-0099.1. URL http://journals.ametsoc.org/doi/abs/10.1175/WAF-D-16-0099.1.

Newman, A. J., Kucera, P. A., and Bliven, L. F. Presenting the Snowflake Video Imager (SVI). *J. Atmos. Oceanic Technol.*, 26(2):167–179, February 2009. ISSN 0739-0572. doi: 10.1175/2008JTECHA1148.1. URL https://journals.ametsoc.org/doi/abs/10.1175/2008JTECHA1148.1.

Norin, L., Devasthale, A., L'Ecuyer, T. S., Wood, N. B., and Smalley, M. Intercomparison of snowfall estimates derived from the CloudSat Cloud Profiling Radar and the ground-based weather radar network over Sweden. *Atmos. Meas. Tech.*, 8(12): 5009–5021, December 2015. ISSN 1867-8548. doi: 10.5194/amt-8-5009-2015. URL https://www.atmos-meas-tech.net/8/5009/2015/.

Norwegian Meteorological Institute. MET Norway Thredds Service, 2016. URL http://thredds.met.no/thredds/catalog/meps25epsarchive/catalog.html.

Olsen, A.-M. and Granerød, M. Ekstremværrapport. Hendelse: Urd 26. desember met. info. no. 18/2017 ISSN X METEOROLOGI Bergen, - PDF, September 2017. URL http://docplayer.me/48734203-Ekstremvaerrapport-hendelse-urd-26-desember-met-info-no-18-2017-issn-x-meteorologi-bergen.html.

Pedersen, K. and Rommetveit, A. Hva er et «ekstremvær»?, November 2013. URL http://www.yr.no/artikkel/hva-er-et-_ekstremvaer__-1.7890946.

Peel, M. C., Finlayson, B. L., and Mcmahon, T. A. Updated world map of the Köppen-Geiger climate classification. *Hydrology and Earth System Sciences Discussions*, 4(2):439–473, March 2007. URL https://hal.archives-ouvertes.fr/hal-00298818.

Pinty, J.-P. and Jabouille, P. A mixed-phased cloud parameterization for use in a mesoscale non-hydrostatic model: Simulations of a squall line and of orographic precipitation. pages 217–220. Amer. Meteor. Soc., 1998.

Putkonen, J. and Roe, G. Rain-on-snow events impact soil temperatures and affect ungulate survival: RAIN-ON-SNOW EVENTS IMPACT SOIL TEMPERATURES. *Geophysical Research Letters*, 30(4), February 2003. ISSN 00948276. doi: 10.1029/2002GL016326. URL http://doi.wiley.com/10.1029/2002GL016326.

Rinehart, R. E. *Radar for Meteorologists: Or You, Too, Can be a Radar Meteorologist*. Rinehart Publications, 2010. ISBN 978-0-9658002-3-5. Google-Books-ID: VqatcQAACAAJ.

Rodgers, C. D. *Inverse Methods for Atmospheric Sounding: Theory and Practice*. World Scientific, 2000. ISBN 978-981-02-2740-1. Google-Books-ID: FjxqDQAAQBAJ.

Rutz, J. J., Steenburgh, W. J., and Ralph, F. M. Climatological Characteristics of Atmospheric Rivers and Their Inland Penetration over the Western United States. *Mon. Wea. Rev.*, 142(2):905–921, January 2014. ISSN 0027-0644. doi: 10.1175/MWR-D-13-00168.1. URL http://journals.ametsoc.org/doi/abs/10.1175/MWR-D-13-00168.1.

Ruud, S., Carr Ekroll, H., Bakke Foss, A., Torgersen, H. O., and Annar Holm, P. To tonn tungt skilt blåste ned da ekstremværet traff Oslo og Østlandet i natt, December 2016. URL https://www.aftenposten.no/article/ap-2z6wy.html.

Schwartz, C. S. Reproducing the September 2013 Record-Breaking Rainfall over the Colorado Front Range with High-Resolution WRF Forecasts. *Wea. Forecasting*, 29(2): 393–402, January 2014. ISSN 0882-8156. doi: 10.1175/WAF-D-13-00136.1. URL https://journals.ametsoc.org/doi/abs/10.1175/WAF-D-13-00136.1.

Seneviratne, S. I., Nicholls, N., Easterling, D., Goodess, C. M., Kanae, S., Kossin, J., Luo, Y., Marengo, J., McInnes, K., Rahimi, M., Reichstein, M., Sorteberg, A., Vera, C., Zhang, X., Rusticucci, M., Semenov, V., Alexander, L. V., Allen, S., Benito, G., Cavazos, T., Clague, J., Conway, D., Della-Marta, P. M., Gerber, M., Gong, S., Goswami, B. N., Hemer, M., Huggel, C., van den Hurk, B., Kharin, V. V., Kitoh, A., Tank, A. M. K., Li, G., Mason, S., McGuire, W., van Oldenborgh, G. J., Orlowsky, B., Smith, S., Thiaw, W., Velegrakis, A., Yiou, P., Zhang, T., Zhou, T., and Zwiers, F. W. Changes in Climate Extremes and their Impacts on the Natural Physical Environment. In Field, C. B., Barros, V., Stocker, T. F., and Dahe, Q., editors, *Managing the Risks of Extreme Events and Disasters to Advance Climate Change Adaptation*, pages 109–230. Cambridge University Press, Cambridge, 2012. ISBN 978-1-139-17724-5. doi: 10.1017/CBO9781139177245.006. URL https://www.cambridge.org/core/product/identifier/CBO9781139177245A030/type/book_part.

Stephens, G. L. *Remote Sensing of the Lower Atmosphere: An Introduction.* Oxford University Press, 1994. ISBN 978-0-19-508188-6. Google-Books-ID: 2FcRAQAAIAAJ.

Stephens, G. L. and Wood, N. B. Properties of Tropical Convection Observed by Millimeter-Wave Radar Systems. *Monthly Weather Review*, 135(3):821–842, March 2007. ISSN 0027-0644, 1520-0493. doi: 10.1175/MWR3321.1. URL http://journals.ametsoc.org/doi/abs/10.1175/MWR3321.1.

Stimberis, J. and Rubin, C. M. Glide avalanche response to an extreme rain-on-snow event, Snoqualmie Pass, Washington, USA. *Journal of Glaciology*, 57(203): 468–474, 2011. ISSN 0022-1430, 1727-5652. doi: 10.3189/002214311796905686. URL https://www.cambridge.org/core/journals/journal-of-glaciology/article/glide-avalanche-response-to-an-extreme-rainonsnow-event-snoqualmie-pass-washington-usa/2B6E48BD92F0700B7BEA02EF156E203F.

Stocker, T. F., Qin, D., Plattner, G.-K., Tignor, M. M. B., Allen, S. K., Boschung, J., Nauels, A., Xia, Y., Bex, V., and Midgley, P. M. Working Group I Contribution to the Fifth Assessment Report of the Intergovernmental Panel on Climate Change. *Cambridge: Cambridge University Press*, page 14, 2013.

Sun, J. Convective-scale assimilation of radar data: progress and challenges. *Quarterly Journal of the Royal Meteorological Society*, 131(613):3439–3463, 2005. ISSN 1477-870X. doi: 10.1256/qj.05.149. URL https://rmets.onlinelibrary.wiley.com/doi/abs/10.1256/qj.05.149.

University Wyoming. Atmospheric Soundings, January 2018. URL http://weather.uwyo.edu/upperair/sounding.html.

Wolff, M. A. WMO Solid Precipitation Intercomparison Experiment (WMO-SPICE), Ch. 4.2.4 Precipitation measurements in areas with high winds and/or complex terrain. unpublished, 2018.

Wolff, M. A., Brækkan, R., Isaksen, K., and Ruud, E. A new testsite for wind correction of precipitation measurements at a mountain plateau in southern Norway. In *Proceedings of WMO Technical Conference on Meteorological and Environmental Instruments and Methods of Observation (TECO–2010). Instruments and Observing Methods Report*, 2010.

Wolff, M. A., Isaksen, K., Brækkan, R., Alfnes, E., Petersen-Øverleir, A., and Ruud, E. Measurements of wind-induced loss of solid precipitation: description of a Norwegian field study. *Hydrol. Res.*, 44(1):35–43, February 2013. ISSN 0029-1277, 2224-7955. doi: 10.2166/nh.2012.166. URL http://hr.iwaponline.com/content/44/1/35.

Wolff, M. A., Isaksen, K., Petersen-Øverleir, A., Ødemark, K., Reitan, T., and Brækkan, R. Derivation of a new continuous adjustment function for correcting wind-induced loss of solid precipitation: results of a Norwegian field study. *Hydrol. Earth Syst. Sci.*, 19 (2):951–967, February 2015. ISSN 1607-7938. doi: 10.5194/hess-19-951-2015. URL https://www.hydrol-earth-syst-sci.net/19/951/2015/.

Wood, N. B. *Estimation of snow microphysical properties with application to millimeter-wavelength radar retrievals for snowfall rate.* Ph.D., Colorado State University, 2011. URL https://dspace.library.colostate.edu/bitstream/handle/10217/48170/Wood_colostate_0053A_10476.pdf?sequence=1&isAllowed=y.

Wood, N. B., L'Ecuyer, T. S., Vane, D. G., Stephens, G. L., and Partain, P. Level 2c snow profile process description and interface control document. Technical Report, 2013. URL http://www.cloudsat.cira.colostate.edu/sites/default/files/products/files/2C-SNOW-PROFILE_PDICD.P_R04.20130210.pdf.

Wood, N. B., L'Ecuyer, T. S., Heymsfield, A. J., Stephens, G. L., Hudak, D. R., and Rodriguez, P. Estimating snow microphysical properties using collocated multisensor observations. *J. Geophys. Res. Atmos.*, 119(14):8941–8961, July 2014. ISSN 2169-8996.

doi: 10.1002/2013JD021303. URL http://onlinelibrary.wiley.com/doi/10.1002/2013JD021303/abstract.

Wood, N. B., L'Ecuyer, T. S., Heymsfield, A. J., and Stephens, G. L. Microphysical Constraints on Millimeter-Wavelength Scattering Properties of Snow Particles. *J. Appl. Meteor. Climatol.*, 54(4):909–931, January 2015. ISSN 1558-8424. doi: 10.1175/JAMC-D-14-0137.1. URL http://journals.ametsoc.org/doi/10.1175/JAMC-D-14-0137.1.

Appendix A: Synoptic Weather Situation

A.1 Skew-T log-P diagram from Stavanger

The Skew-T log-P diagram shows the observed vertical temperature and dew-point temperature at Stavanger. The data are taken from University Wyoming [2018] and processed in Python.

Isobars are grey lines, every 50 hPa, dry adiabats are blue (labelled in °C), isotherms are red [°C], water vapour mixing ratios are green, dashed in [$\mathrm{g\,kg^{-1}}$], and moist adiabats are dashed, purple lines (labelled in [°C]).

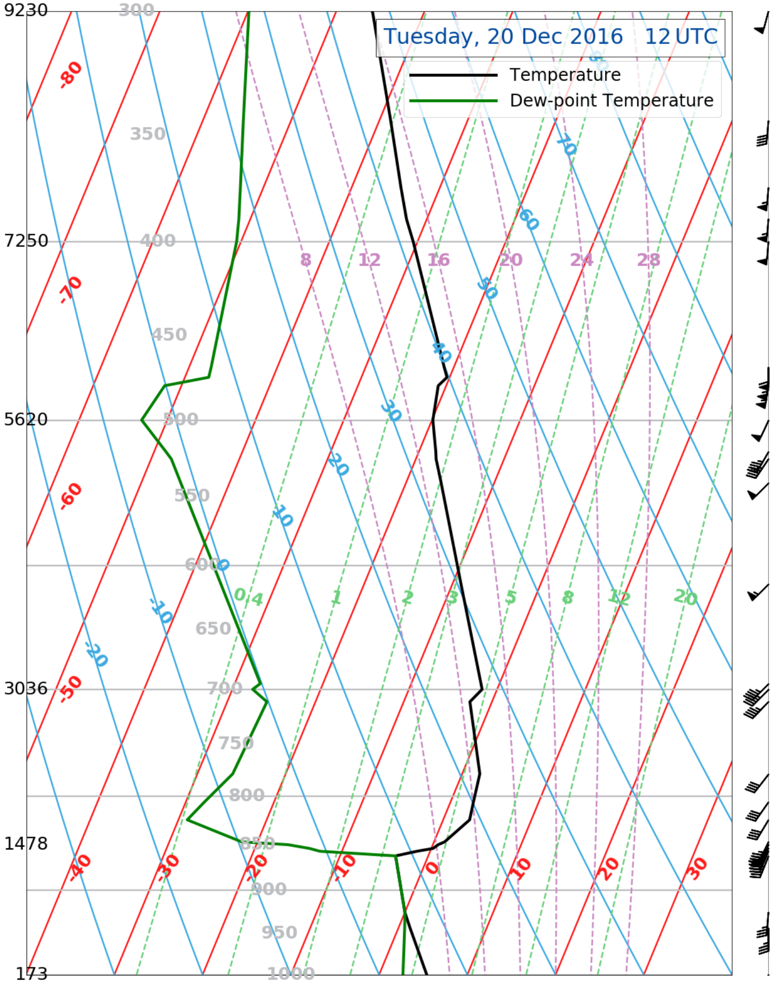
Tuesday, 20 Dec 2016 12 UTC
Temperature
Dew-point Temperature
9230
7250
5620
3036
1478
173
300
350
400
450
500
550
600
650
700
750
800
850
900
950
1000

(a)

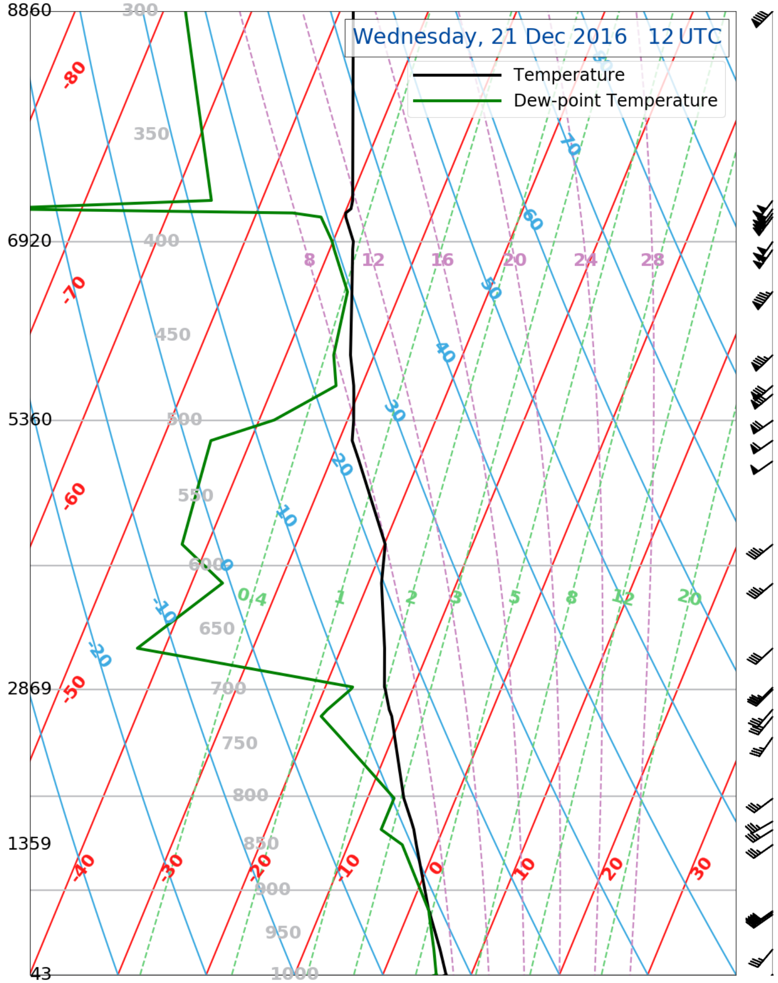
Wednesday, 21 Dec 2016 12 UTC
Temperature
Dew-point Temperature
8860
6920
5360
2869
1359
43
300
350
400
450
500
550
600
650
700
750
800
850
900
950
1000

(b)

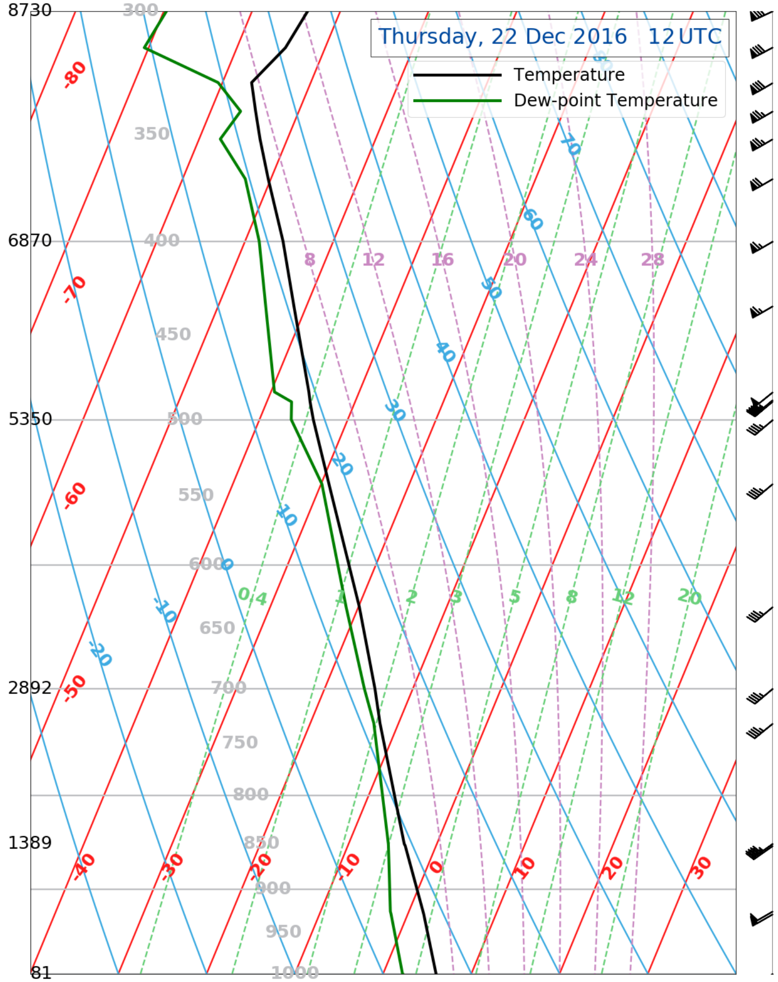
Thursday, 22 Dec 2016 12UTC
Temperature
Dew-point Temperature
8730
6870
5350
2892
1389
81
300
350
400
450
500
550
600
650
700
750
800
850
900
950
1000

(c)

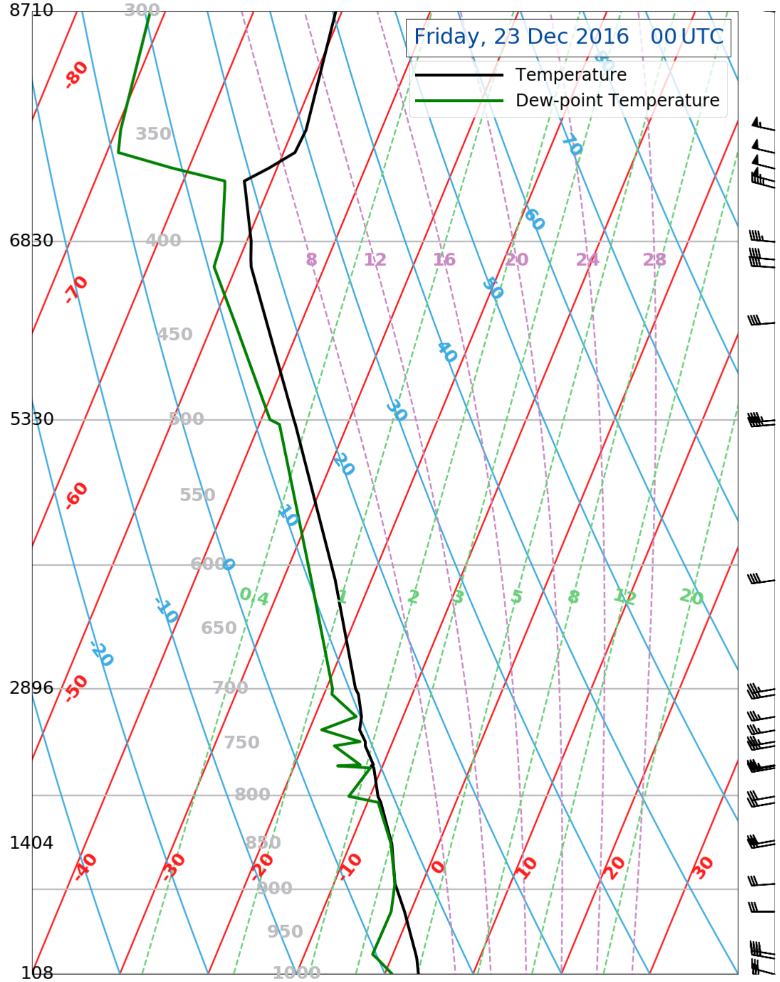
Friday, 23 Dec 2016 00UTC
Temperature
Dew-point Temperature
8710
6830
5330
2896
1404
108
300
350
400
450
500
550
600
650
700
750
800
850
900
950
1000

(d)

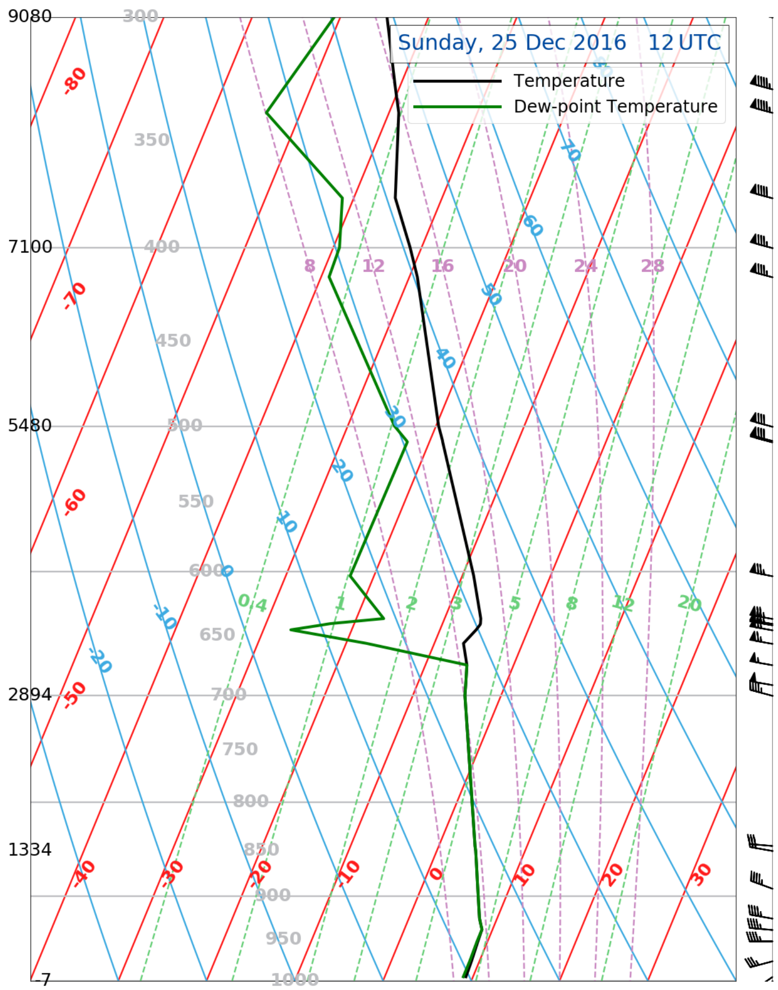

(e)

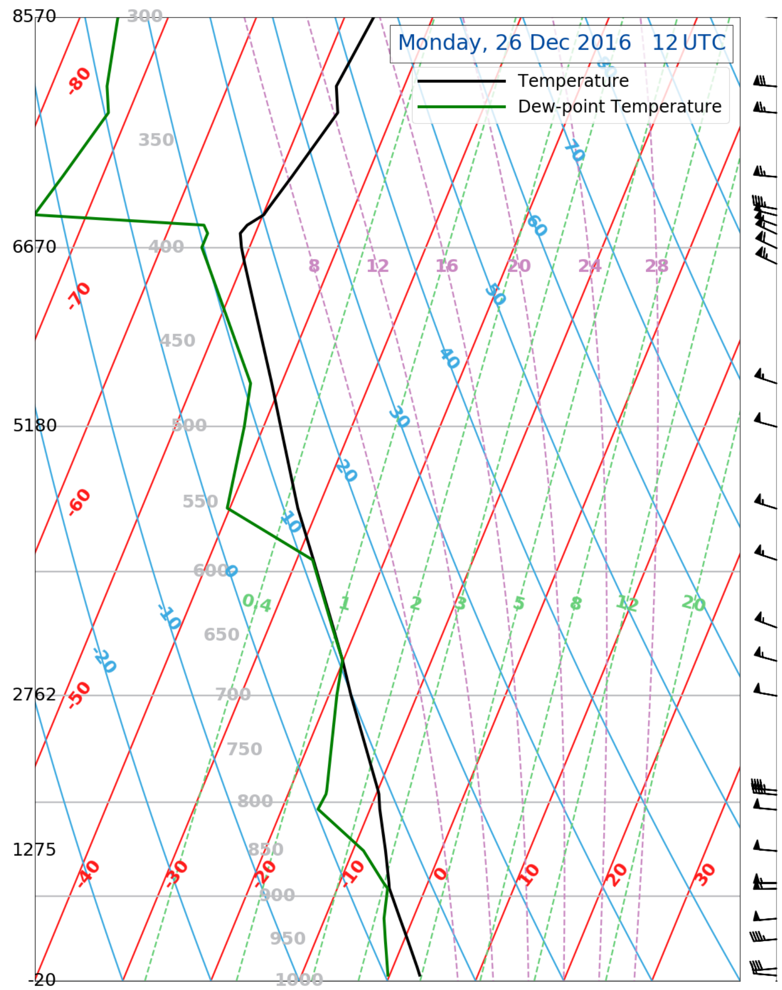

(f)

Figure A.1.1: Vertical profiles of atmospheric temperature (black) and dew-point temperature (green) during 20 December 2016 to 26 December 2016. Vertical Profiles from 24 December 2016 are missing at the webpage http://weather.uwyo.edu/upperair/sounding.html

Appendix B: Forward Model

B.1 Scattering Model

Table B.1.1: Branched 6-arm spatial particle with porosities, 2D, mass oriented scattering scheme at 24.0GHz. $\mathbf{r}$, particle size of the snow particle; $\mathbf{m}(\mathbf{r})$, particle mass; $\sigma_{\mathbf{bk}}(\mathbf{r})$ and $\sigma_{\mathbf{ext}}(\mathbf{r})$, backscattering and extinction cross-section, respectively.

$\mathbf{r}$ [μm]	$\mathbf{m}(\mathbf{r})$ [kg]	$\sigma_{\mathbf{bk}}(\mathbf{r})$ [m^{-2}]	$\sigma_{\mathbf{ext}}(\mathbf{r})$ [m^{-2}]
35.27	1.68529×10^{-10}	8.85111×10^{-17}	4.85381×10^{-17}
41.73	2.79128×10^{-10}	2.00612×10^{-16}	1.28776×10^{-16}
47.87	4.21355×10^{-10}	4.792×10^{-16}	2.9959×10^{-16}
53.76	5.96809×10^{-10}	1.02733×10^{-15}	6.08871×10^{-16}
59.45	8.07074×10^{-10}	1.68272×10^{-15}	1.09633×10^{-15}
70.34	1.3368×10^{-9}	5.7444×10^{-15}	3.61096×10^{-15}
80.69	2.01798×10^{-9}	1.0899×10^{-14}	6.93961×10^{-15}
90.63	2.85939×10^{-9}	2.244×10^{-14}	1.42249×10^{-14}
100.20	3.86421×10^{-9}	3.7814×10^{-14}	2.73019×10^{-14}
109.50	5.04313×10^{-9}	7.05869×10^{-14}	5.36211×10^{-14}
118.60	6.40785×10^{-9}	1.16874×10^{-13}	9.74644×10^{-14}
127.40	7.94266×10^{-9}	1.67227×10^{-13}	1.56602×10^{-13}
144.50	1.15894×10^{-8}	3.41952×10^{-13}	4.19048×10^{-13}
160.90	1.60002×10^{-8}	7.30397×10^{-13}	1.05187×10^{-12}

Continued on next page

Table B.1.1 Continued from previous page

$\mathbf{r}$ [μm]	$\mathbf{m(r)}$ [kg]	$\sigma_{\mathbf{bk}}(\mathbf{r})$ [m^{-2}]	$\sigma_{\mathbf{ext}}(\mathbf{r})$ [m^{-2}]
176.80	2.12278×10^{-8}	1.13638×10^{-12}	2.00359×10^{-12}
192.30	2.73147×10^{-8}	2.05333×10^{-12}	3.63531×10^{-12}
236.50	5.08103×10^{-8}	5.94138×10^{-12}	1.5256×10^{-11}
278.10	8.26154×10^{-8}	1.57715×10^{-11}	4.31927×10^{-11}
317.70	1.23171×10^{-7}	3.68719×10^{-11}	9.71916×10^{-11}
355.80	1.73012×10^{-7}	6.46005×10^{-11}	1.89057×10^{-10}
392.60	2.32439×10^{-7}	1.29191×10^{-10}	3.5246×10^{-10}
428.20	3.01577×10^{-7}	1.7526×10^{-10}	5.67393×10^{-10}
463.00	3.81242×10^{-7}	3.58177×10^{-10}	8.76374×10^{-10}
496.90	4.71265×10^{-7}	5.86279×10^{-10}	1.30417×10^{-9}
530.10	5.72178×10^{-7}	8.50141×10^{-10}	1.8862×10^{-9}
562.60	6.84002×10^{-7}	1.04566×10^{-9}	2.60854×10^{-9}
594.50	8.07074×10^{-7}	1.54514×10^{-9}	3.68176×10^{-9}
625.80	9.41379×10^{-7}	1.61704×10^{-9}	4.48578×10^{-9}
656.60	1.08733×10^{-6}	2.10709×10^{-9}	5.71184×10^{-9}
687.00	1.24546×10^{-6}	3.31567×10^{-9}	7.85938×10^{-9}
717.00	1.41584×10^{-6}	3.73598×10^{-9}	9.50817×10^{-9}
746.50	1.59789×10^{-6}	4.40591×10^{-9}	1.14824×10^{-8}
775.60	1.79214×10^{-6}	5.1432×10^{-9}	1.37371×10^{-8}
804.40	1.99928×10^{-6}	4.21261×10^{-9}	1.59603×10^{-8}
832.90	2.2194×10^{-6}	7.0875×10^{-9}	1.90438×10^{-8}
861.10	2.45255×10^{-6}	7.606×10^{-9}	2.17023×10^{-8}
888.90	2.69784×10^{-6}	9.61605×10^{-9}	2.52476×10^{-8}
916.50	2.95703×10^{-6}	1.20108×10^{-8}	2.91329×10^{-8}
943.80	3.22922×10^{-6}	1.29326×10^{-8}	3.30911×10^{-8}
970.80	3.51437×10^{-6}	1.53246×10^{-8}	3.82595×10^{-8}
997.60	3.81353×10^{-6}	1.32687×10^{-8}	4.344×10^{-8}

Appendix C: Results

C.1 48 h surface observations and MEPS forecasts

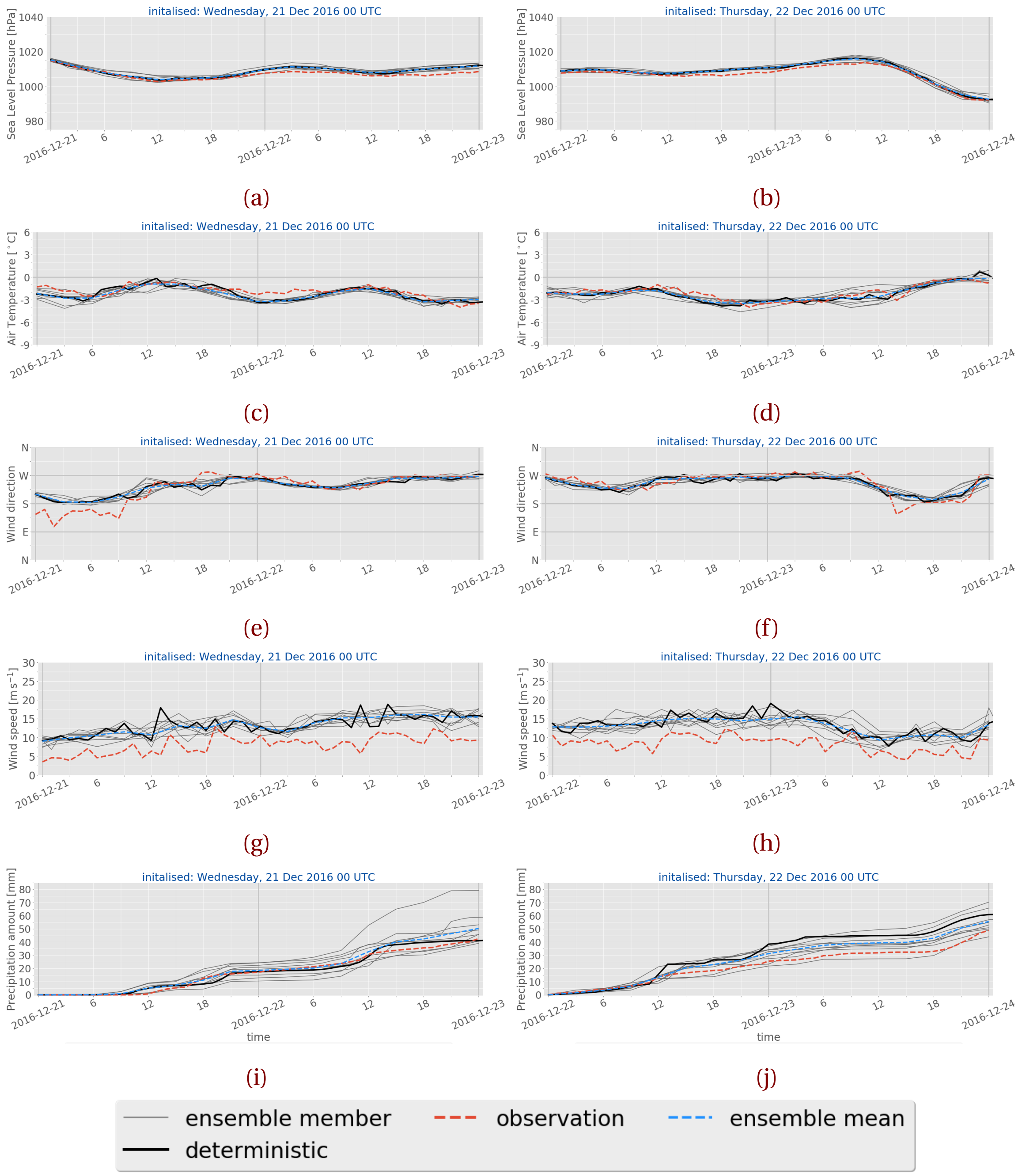

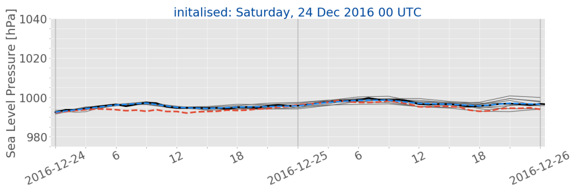

(k)

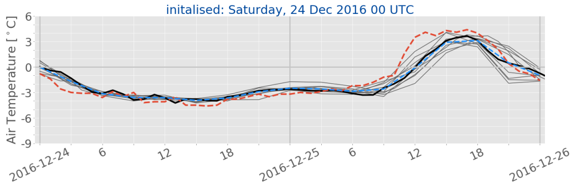

(l)

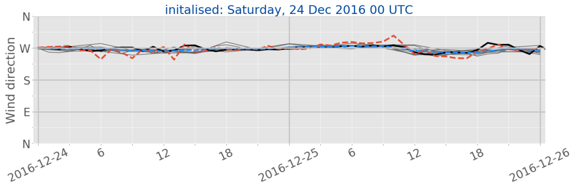

(m)

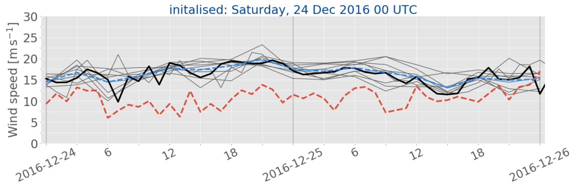

(n)

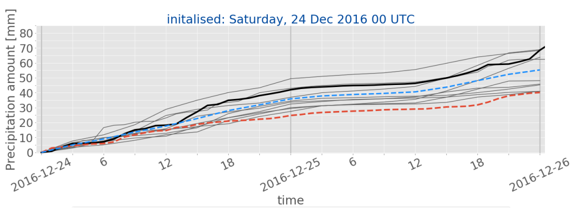

(o)

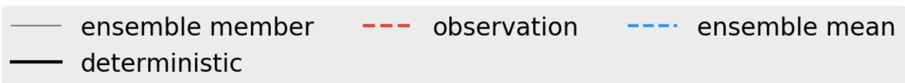

Figure C.1.1: *(Continued from previous page.)* Initialisations for 22 December 2016 (k, l, m, n, o)

C.2 MEAN ERROR AND MEAN ABSOLUTE ERROR

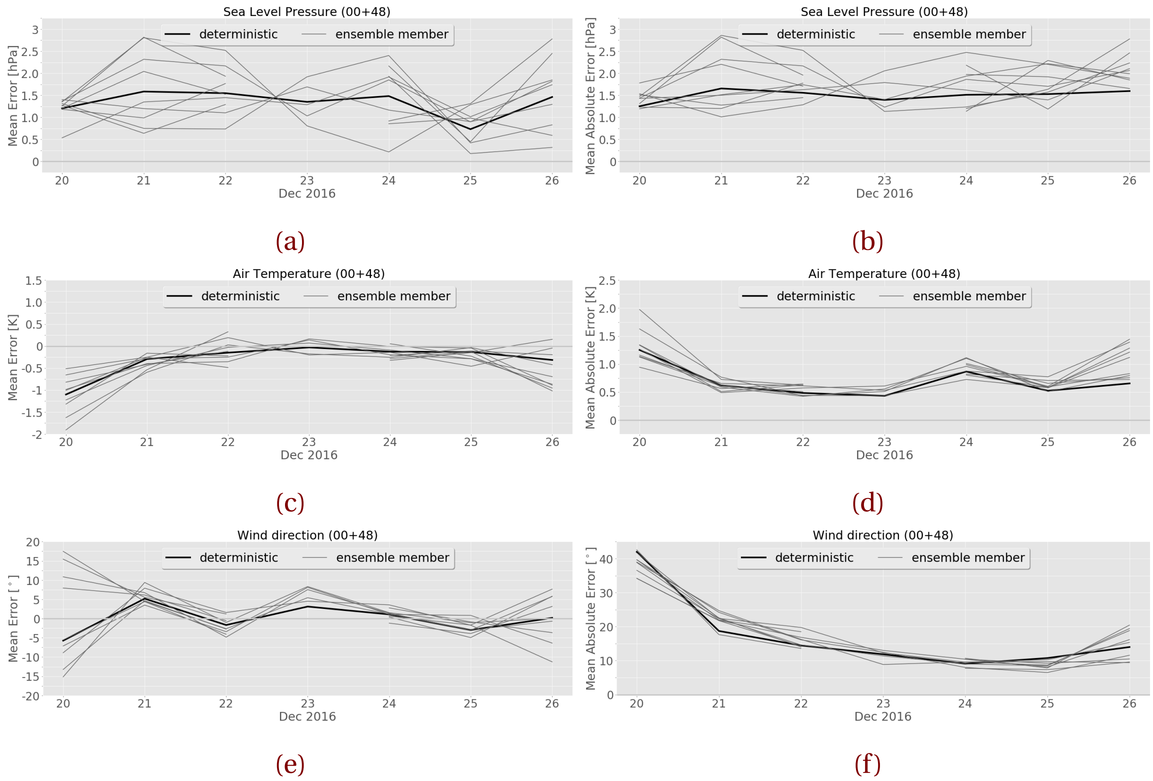

Figure C.2.1: Mean error (a, c, e, g, i) and mean absolute error (b, d, f, h, j) of surface variables for all ten ensemble members at Haukeliseter, initialisations at 0 UTC, valid for 48 h. From top to bottom, sea level pressure (a, b), 2 m air temperature (c, d), 10 m wind direction (e, f).

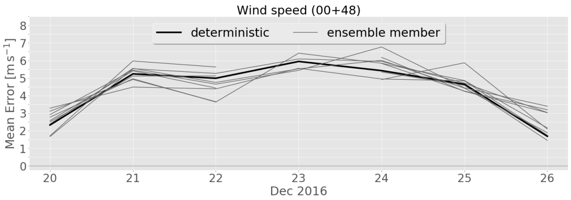

(g)

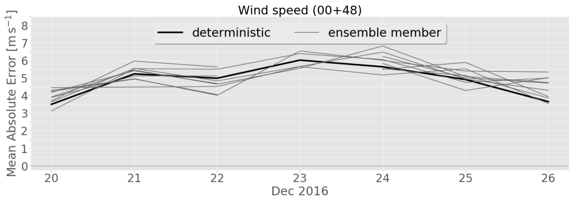

(h)

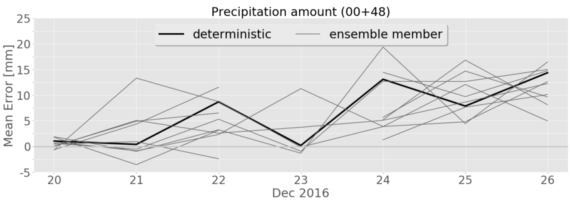

(i)

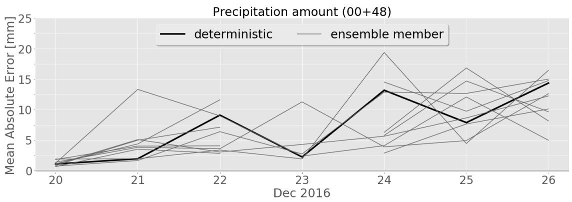

(j)

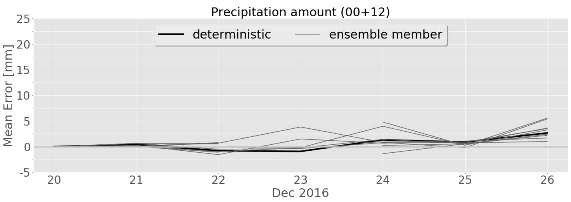

(k)

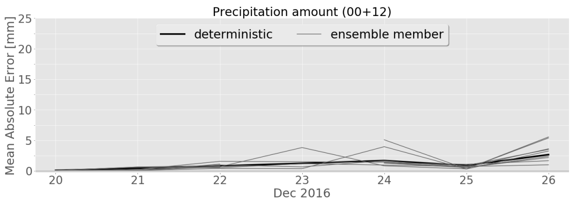

(l)

Figure C.2.1: *(Continued from previous page.)* , 10 m wind speed (g, h), precipitation accumulation for 48 h (i, j) and 12 h surface accumulation (k, l).

C.3 Hourly averages ensemble member zero and one

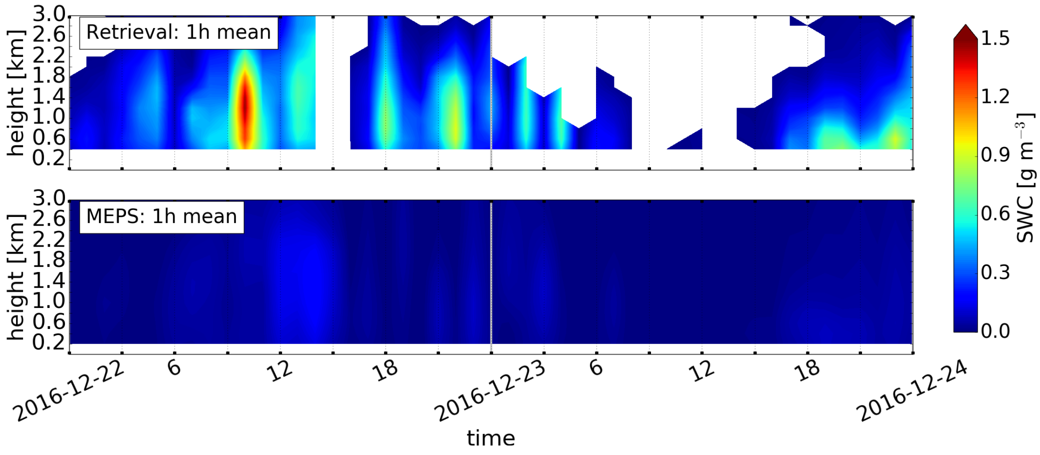

(a)

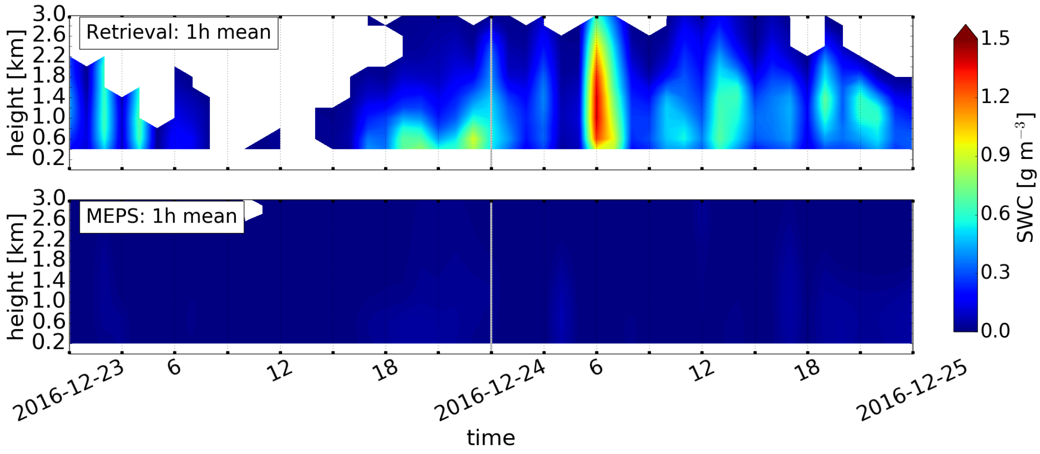

(b)

Figure C.3.1: Upper panel: hourly averaged retrieved SWC, lower panel instantaneous hourly averaged SWC forecast of deterministic and first ensemble member. Initialised 22 December 2016 and 23 December 2016 at 0 UTC.

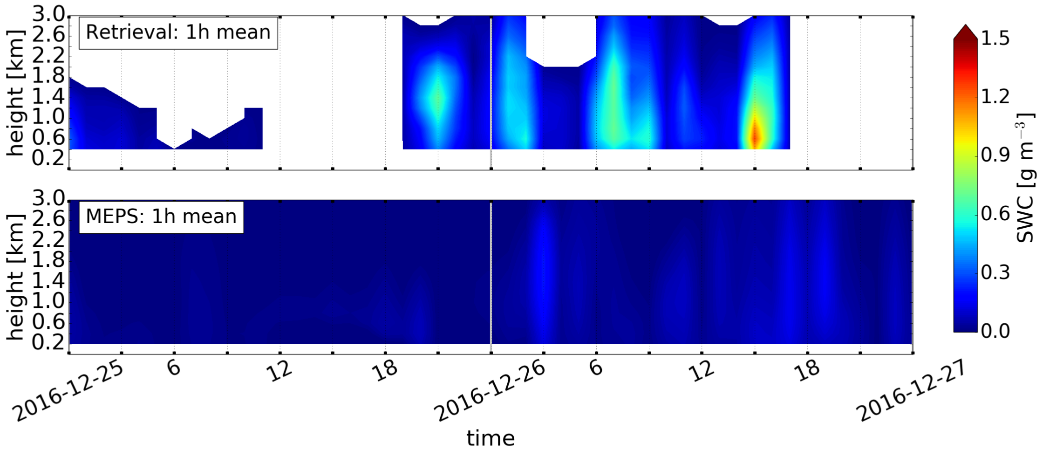

(c)

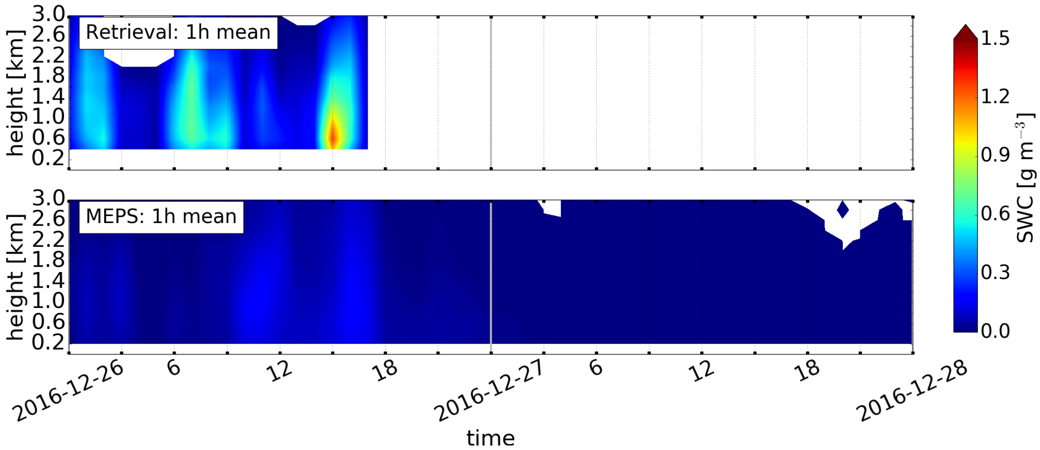

(d)

Figure C.3.1: *(Continued from previous page.)* Initialised 25 December 2016 and 26 December 2016 at 0 UTC.

C.4 Vertical SWC - all ensemble member

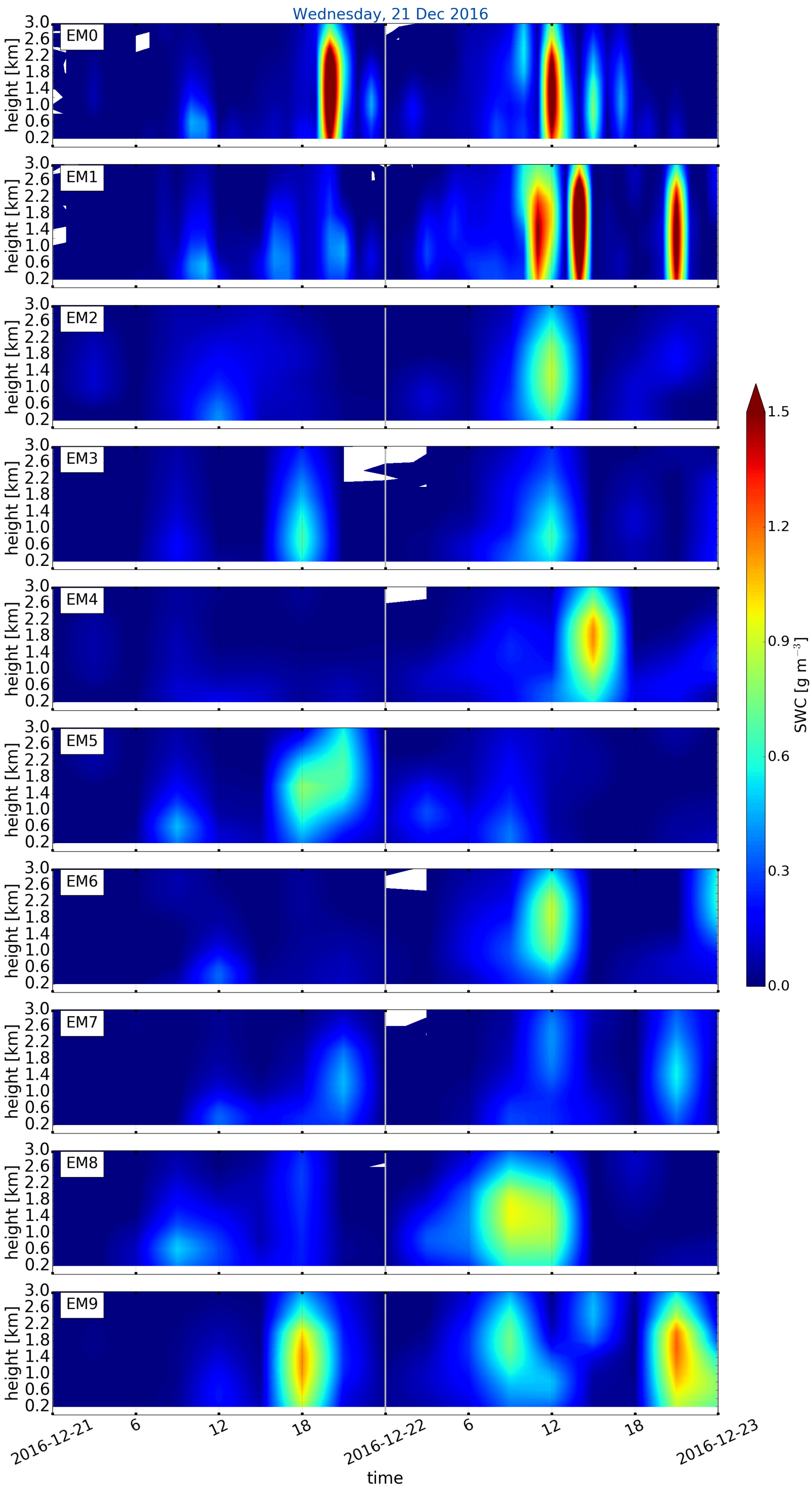

(a)

Figure C.4.1: Vertical SWC of each individual ensemble member from 0 to 9 forecast for 48 h. Initialised 21 December 2016 at 0 UTC.

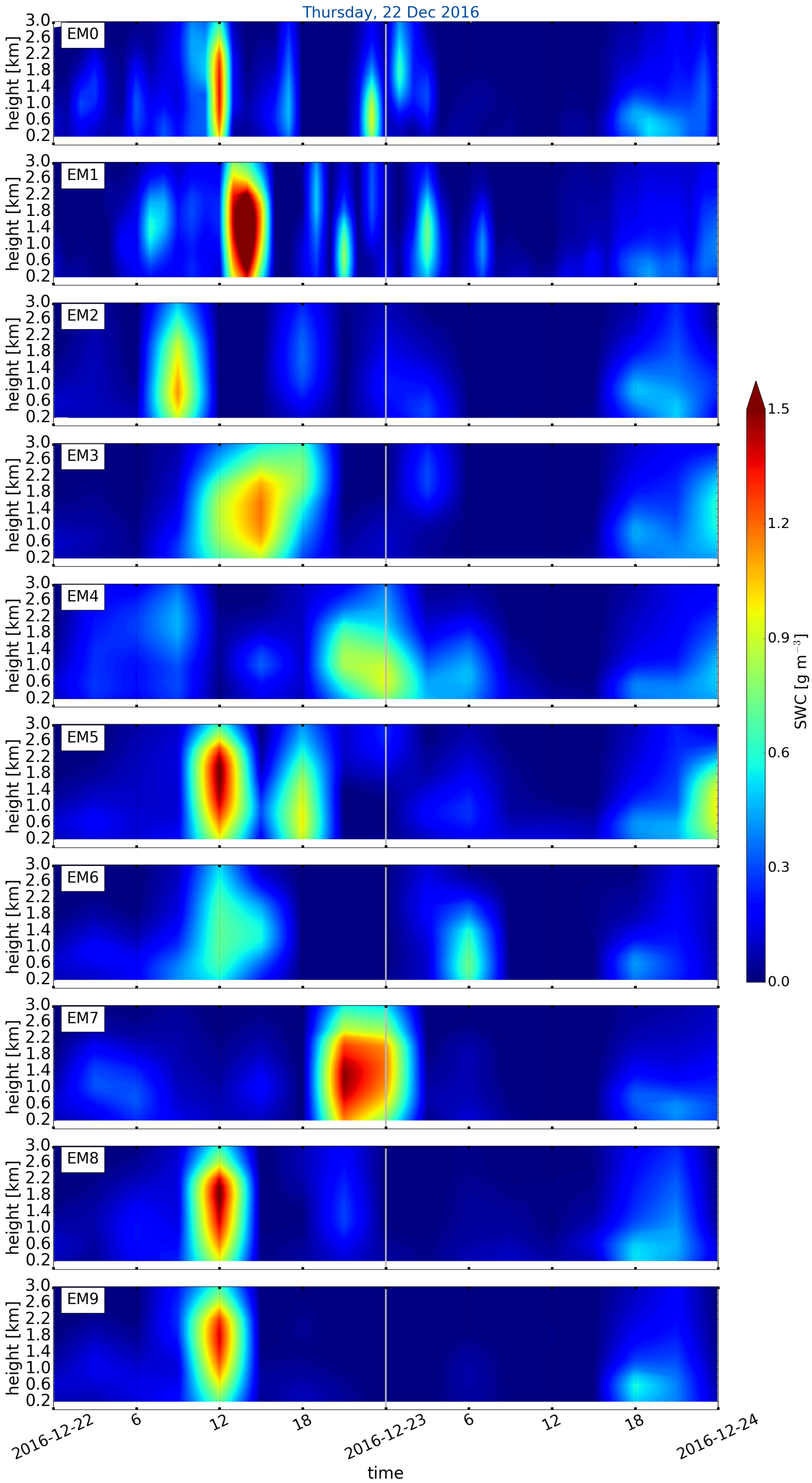

(a)

Figure C.4.2: *(Continued from previous page.)* Initialised 22 December 2016 at 0 UTC.

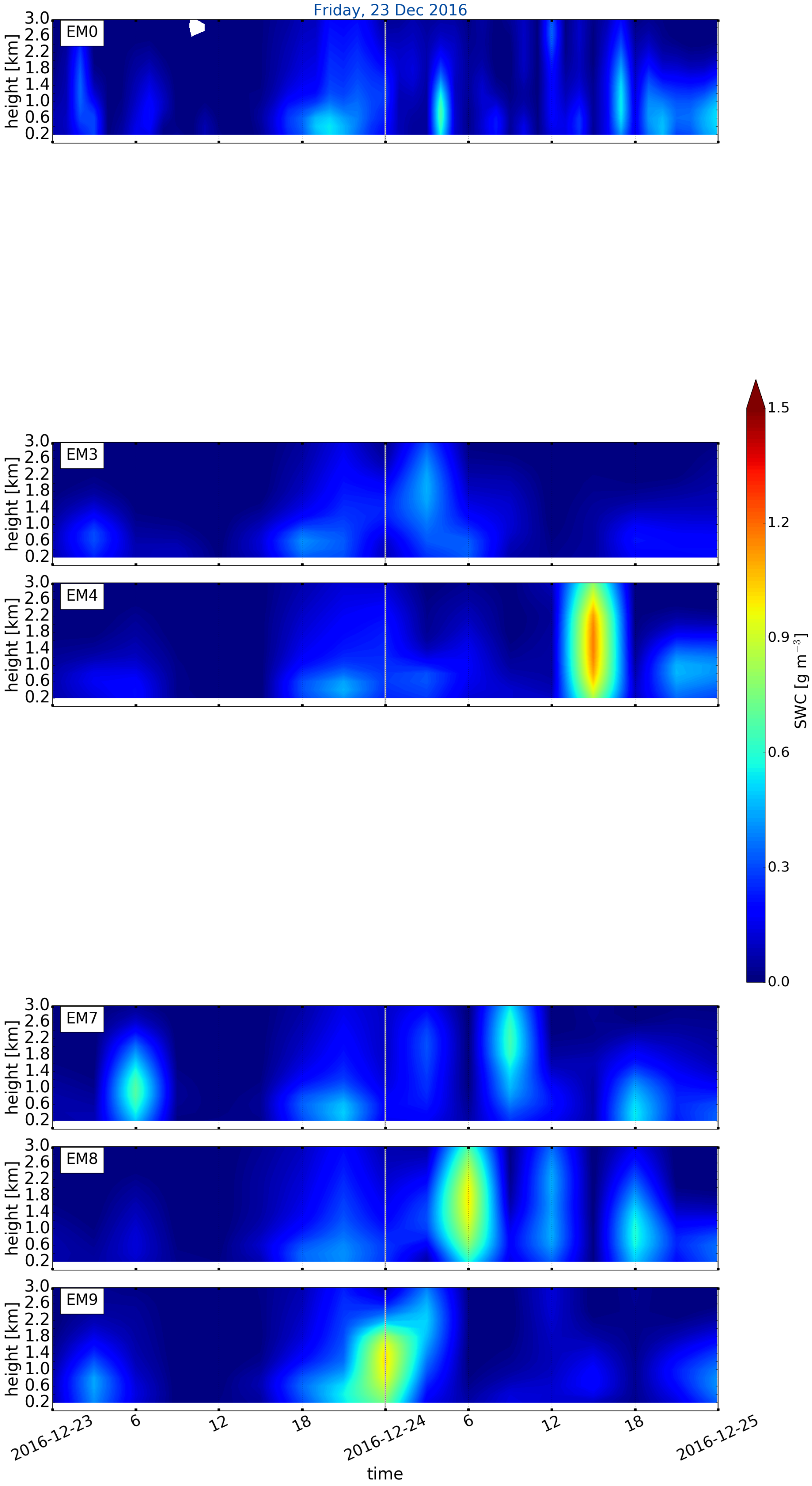

(b)

Figure C.4.2: *(Continued from previous page.)* Initialised 23 December 2016 at 0 UTC.

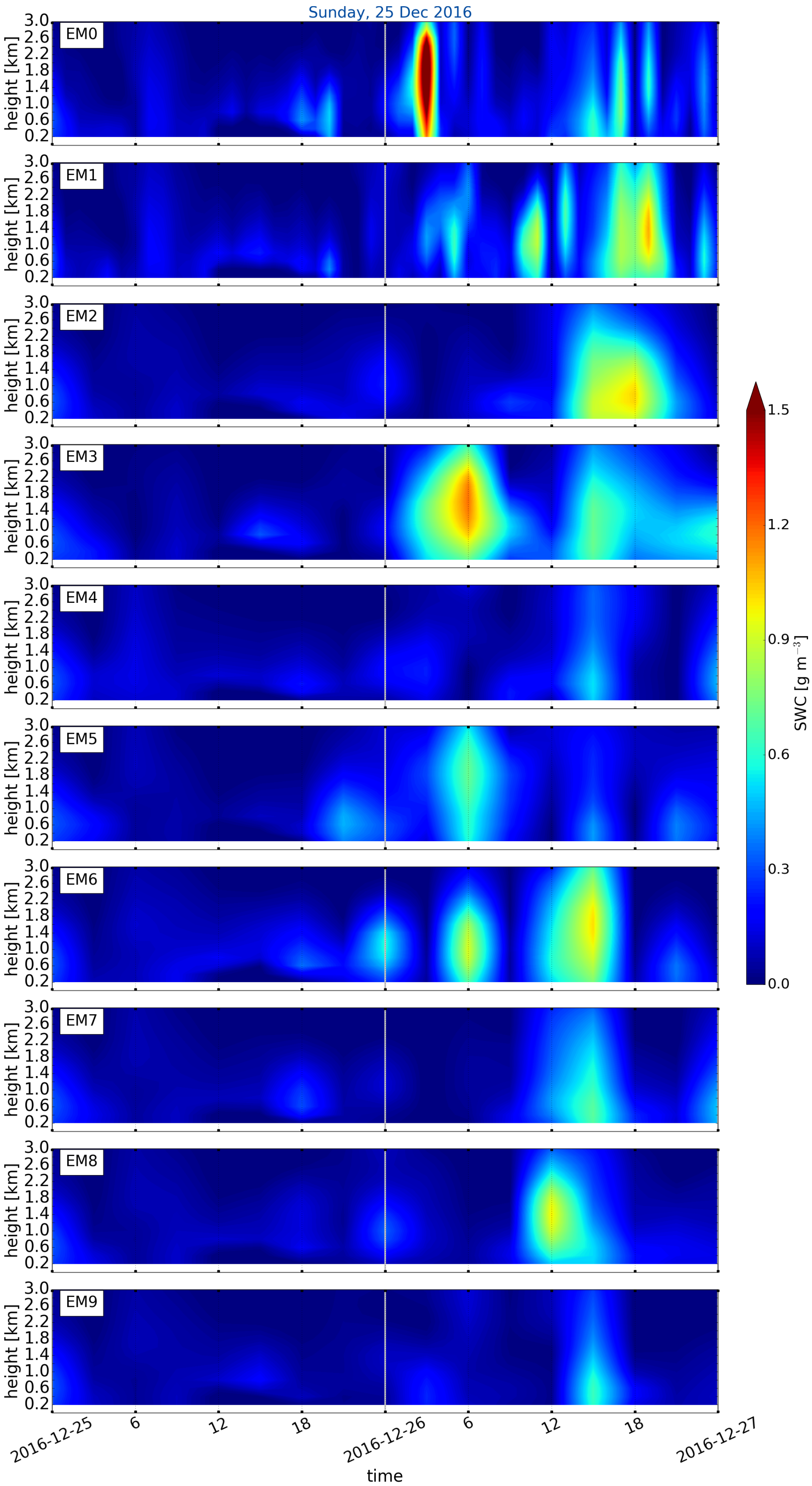

(c)

Figure C.4.2: *(Continued from previous page.)* Initialised 25 December 2016 at 0 UTC.

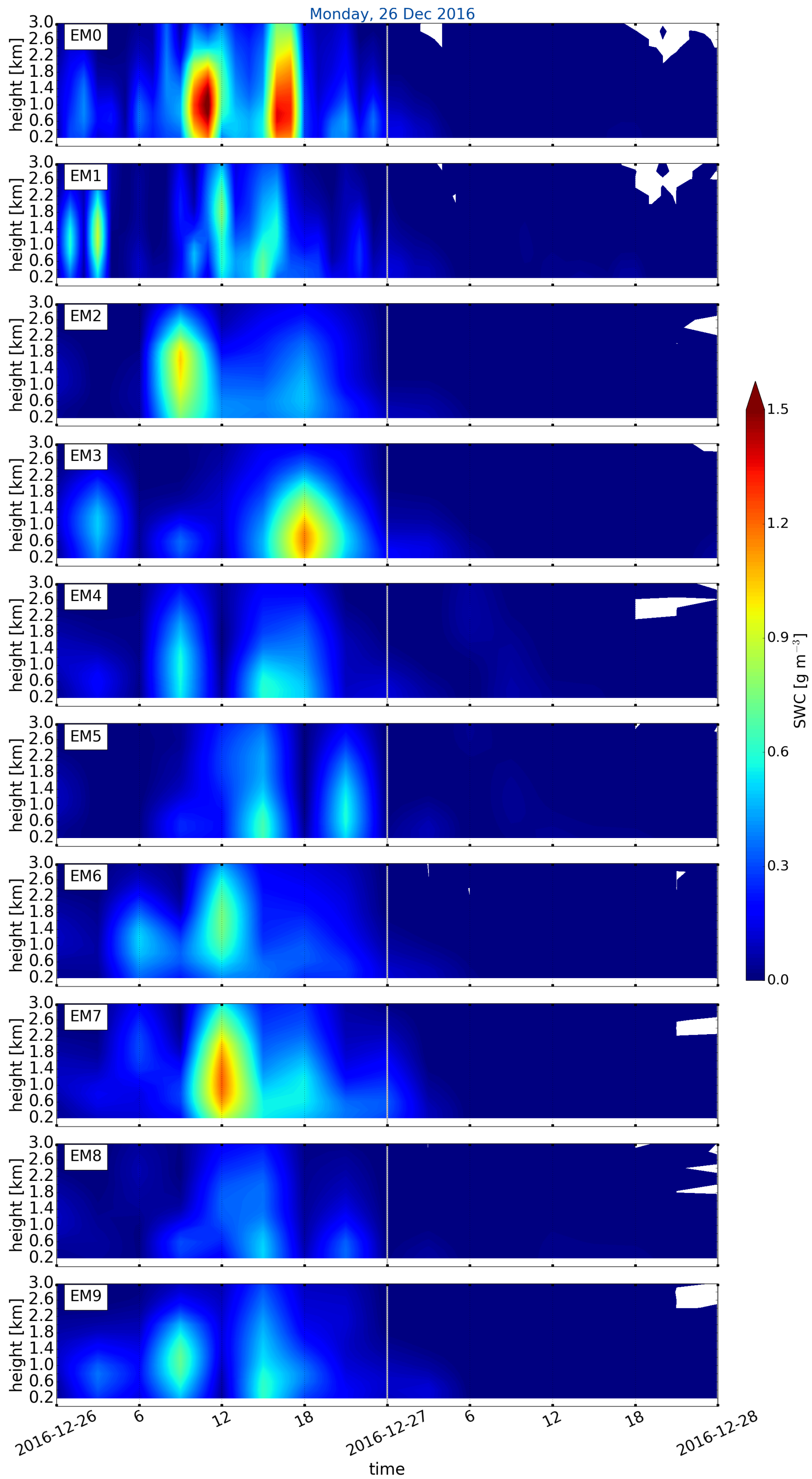

(d)

Figure C.4.2: *(Continued from previous page.)* Initialised 26 December 2016 at 0 UTC.

DECLARATION

I hereby declare that except where specific reference is made to the work of others, the contents of this thesis is made independently. I have explicitly marked all material which has been quoted either literally or by content from the used sources.
Furthermore, I certify that this research thesis or any part of it has not been previously submitted for a degree or any other qualification at the University of Oslo or any other institution in Norway or abroad.

Franziska Hellmuth
Oslo, June 2018